

LEVEL

2

NAVAL POSTGRADUATE SCHOOL

Monterey, California

AD A105758



DTIC
ELECTE
OCT 20 1981
S A D

THESIS

THE EFFECT OF SCATTERING AND ABSORPTION
ON NOISE FROM A CAVITATING NOISE SOURCE
IN THE SUBSURFACE OCEAN LAYER

by

Yngvar Dag Tronstad

June 1981

Thesis Advisor:

K. E. Woehler

Approved for public release; distribution unlimited

FILE COPY

10 31

UNCLASSIFIED

SECURITY CLASSIFICATION OF THIS PAGE (When Data Entered)

REPORT DOCUMENTATION PAGE		READ INSTRUCTIONS BEFORE COMPLETING FORM
1. REPORT NUMBER	2. GOVT ACCESSION NO. AD-A105 758	3. RECIPIENT'S CATALOG NUMBER
4. TITLE (and Subtitle) The Effect of Scattering and Absorption on Noise from a Cavitating Noise Source in the Subsurface Ocean Layer.		5. TYPE OF REPORT & PERIOD COVERED Master's thesis June 1981
7. AUTHOR(s) Yngvar Dag/Tronstad		6. PERFORMING ORG. REPORT NUMBER
9. PERFORMING ORGANIZATION NAME AND ADDRESS Naval Postgraduate School Monterey, California 93940		8. CONTRACT OR GRANT NUMBER(s)
11. CONTROLLING OFFICE NAME AND ADDRESS Naval Postgraduate School Monterey, California 93940		10. PROGRAM ELEMENT, PROJECT, TASK AREA & WORK UNIT NUMBERS D111
14. MONITORING AGENCY NAME & ADDRESS (if different from Controlling Office)		12. REPORT DATE June 1981
		13. NUMBER OF PAGES 176 pages
		15. SECURITY CLASS. (of this report) Unclassified
		15a. DECLASSIFICATION/DOWNGRADING SCHEDULE
16. DISTRIBUTION STATEMENT (of this Report) Approved for public release; distribution unlimited		
17. DISTRIBUTION STATEMENT (of the abstract entered in Block 20, if different from Report) Approved		
18. SUPPLEMENTARY NOTES		
19. KEY WORDS (Continue on reverse side if necessary and identify by block number) Scattering, absorption, rough sea surface, inhomogeneous bubble-dominated subsurface layer, torpedo, turn rate limitation, cavitating propeller, square law detector.		
20. ABSTRACT (Continue on reverse side if necessary and identify by block number) When investigating the detection performance of a passive homing torpedo used against shallow draft surface ships, certain environmental factors such as the rough sea surface and the bubble dominated inhomogeneous layer near the sea surface have to be considered. This thesis attempts to gain some insight into the behavior of a homing torpedo system during its critical attack phase, as well as getting some indications of the relative importance of the scattering mechanisms and the induced tactical		

DD FORM 1473
1 JAN 73

EDITION OF 1 NOV 68 IS OBSOLETE
S/N 0102-014-6001

UNCLASSIFIED 25143
SECURITY CLASSIFICATION OF THIS PAGE (When Data Entered)

UNCLASSIFIED

SECURITY CLASSIFICATION OF THIS PAGE/When Data Entered

limitations. An idealized propagation model was used as reference of comparison. For a given sea state and target speed, the results stress the importance of low operating frequency as well as a high maximum turn rate. They also point to the importance of having a search depth below the bubble-dominated subsurface layer, and a variable speed capability during the torpedo's attack phase.

7

Availability Codes	
Dist	Avail and/or Special
A	

Approved for public release; distribution unlimited

The Effect of Scattering and Absorption
on Noise from a Cavitating Noise Source
in the Subsurface Ocean Layer

by

Yngvar Dag Tronstad
Commander, Norwegian Navy
Marine Engineer, Norwegian Naval Academy, 1969

Submitted in partial fulfillment of the
requirements for the degree of

MASTER OF SCIENCE IN ENGINEERING ACOUSTICS

from the

NAVAL POSTGRADUATE SCHOOL
June 1981

Author

Yngvar D. Tronstad.

Approved by:

H. W. W. W.

Thesis Advisor

James V. Sanders

Second Reader

J. P. Durr

Chairman, Department of Physics and Chemistry

William M. Jolley

Dean of Science and Engineering

ABSTRACT

When investigating the detection performance of a passive homing torpedo used against shallow draft surface ships, certain environmental factors such as the rough sea surface and the bubble-dominated inhomogeneous layer near the sea surface have to be considered. This thesis attempts to gain some insight into the behavior of a homing torpedo system during its critical attack phase, as well as getting some indications of the relative importance of the scattering mechanisms and the induced tactical limitations. An idealized propagation model was used as reference of comparison. For a given sea state and target speed the results stress the importance of low operating frequency as well as a high maximum turn rate. They also point to the importance of having a search depth below the bubble-dominated subsurface layer, and a variable speed capability during the torpedo's attack phase.

TABLE OF CONTENTS

I. INTRODUCTION-----12

II. SCENARIO AND TORPEDO RUN GEOMETRY-----15

III. OCEANOGRAPHIC BACKGROUND MATERIAL-----17

IV. THE PASSIVE SONAR EQUATION-----21

V. REFERENCE MODEL-----22

 A. INTRODUCTION-----22

 B. IDEALIZED TRANSMISSION LOSS MODEL-----22

 C. NOISE SOURCE MODEL-----23

 1. General Characteristics of Noise Sources--23

 2. The Noise Source Model-----26

 D. PASSIVE MODE RECEIVER CHARACTERISTICS-----31

 1. Assumptions-----31

 2. Derivations-----32

 E. REFERENCE DETECTION PERFORMANCE-----38

 1. Introduction-----38

 2. 60 kHz Case-----38

 3. 30 kHz Case-----40

VI. THE EFFECT OF SURFACE SCATTERING-----42

 A. OCEANOGRAPHIC DESCRIPTION OF THE SEA SURFACE--42

 B. SCATTERING THEORY-----45

 C. GEOMETRICAL SHADOWING-----57

 D. ESTIMATING THE SURFACE SCATTERING EFFECT-----61

 E. CONCLUSION AND DISCUSSION-----67

VII. THE EFFECT OF SCATTERING AND ABSORPTION FROM THE SUBSURFACE OCEAN LAYER-----	69
A. GENERAL SCATTERING THEORY-----	69
B. ABSORPTION MODEL-----	70
C. THE COHERENT INTENSITY CASE-----	75
D. THE INCOHERENT INTENSITY CASE-----	82
E. SUMMARY AND DISCUSSION OF THE BUBBLE ATTENUATION-----	83
F. THE REFRACTION BY BUBBLES-----	85
VIII. THE TURN RATE LIMITATION-----	89
IX. CONCLUSIONS AND RECOMMENDATIONS-----	99
APPENDIX A: Detailed Oceanographic Background Material-----	102
APPENDIX B: Surface Scattering TI 59 Program-----	110
APPENDIX C: Bubble Dynamics TI 59 Program-----	116
APPENDIX D: Numerical Integration TI 59 Program-----	121
APPENDIX E: Turn Rate Limitation TI 59 Programs-----	124
APPENDIX F: Figures-----	132
LIST OF REFERENCES-----	174
INITIAL DISTRIBUTION LIST-----	176

LIST OF TABLES

I.	Relationship between Sea State (SS), Wind Speed, and Expected Significant Wave Heights (H_s)-----	18
II.	Source Level Data and Calculation for a Blade Surface Cavitating Propeller-----	29
III.	Detection Parameters and Ranges for $f=60$ kHz-----	86
IV.	Detection Parameters and Ranges for $f=30$ kHz-----	87
V.	Frequency Distribution of Wind Speed in Percent per Year at Weather Stations Along the Norwegian Coast ---	104
VI.	Frequency Distribution of Significant Wave Height in Percent at the Weather Station "Andenes"-----	106

LIST OF FIGURES

1.	Torpedo Search and Attack Geometry-----	132
2.	Location of Weather Stations along the Norwegian Coast-----	133
3.	Average Monthly Wind Speed in Beaufort from the Weather Station "Andenes"-----	134
4.	Histogram of Significant Wave in Percent per Year from the Weather Station "Andenes"-----	135
5.	Resonant Bubble Density at 12 kHz as a Function of Depth-----	136
6.	Resonant Bubble Density at 38 kHz as a Function of Depth-----	137
7.	Resonant Bubble Density at 120 kHz as a Function of Depth-----	138
8.	Ambient Noise Level Curves-----	139
9.	Typical Sound Speed Profiles in Norwegian Coastal Waters-----	140
10.	Worst Case Ray Path During Winter-----	141
11.	Worst Case Ray Path During Summer-----	142
12.	Frequencies of Wind Directions in Percent for Stations along the Coast from "Hillesøy" to "Ona"-----	143
13.	Frequencies of Wind Directions in Percent for Stations along the Coast from "Myken" to "Furuholmen"-----	144
14.	Absorption Coefficient in dB/m as a Function of Frequency-----	145
15.	Average Radiated Spectrum Level for Surface Ship as a Function of Speed in kts-----	146
16.	General Noise Spectrum for a Cavitating Propeller-----	147
17.	Spectrum Level as a Function of Total Gas Content-----	148
18.	Measured Model and Full Scale Noise Spectra-----	149

19.	Square Law Detector Scheme-----	150
20.	Required Input S/N Ratio and BT Product for Various Operating Probabilities-----	151
21.	Probability of Detection Versus Input S/N Ratio for Various Thresholds-----	152
22.	$-20\log R - \alpha R$ Versus R for a Frequency of 60 kHz-----	153
23.	$-20\log R - \alpha R$ Versus R for a Frequency of 30 kHz-----	154
24a.	Geometry of the Sea Surface Scattering-----	155
24b.	Specular Scattering Geometry-----	156
25.	Rough Surface Shadowing Geometry-----	157
26.	Calculation Scheme of the Surface Scattering Effect-----	158
27.	ΔIL Versus R-----	159
28.	Geometry of the Subsurface Propagation Model-----	160
29a.	Chains of Successive Scattering-----	161
29b.	Scattering Path Going Through the Same Scatterer More Than Once-----	161
30.	Scattering Pattern-----	162
31.	σ_e and σ_a for 60 kHz-----	163
32.	σ_e and σ_a for 30 kHz-----	164
33.	Interpolated Bubble Data-----	165
34.	$\sigma_e(a)n(a)da$ for 60 kHz-----	166
35.	$\sigma_e(a)n(a)da$ for 30 kHz-----	167
36.	$\sigma_a(a)n(a)da$ for 60 kHz-----	168
37.	$\sigma_a(a)n(a)da$ for 30 kHz-----	169
38.	Pursuit Homing Geometry-----	170
39.	$ \dot{\phi}K/V_s $ as a Function of ϕ with Parameter p-----	171
40.	Hit Criterion Geometry-----	172

41. AOB-Limitation Versus Ship Speed with Parameter Maximum
Turn Rate-----173

ACKNOWLEDGMENT

The author wishes to gratefully express his appreciation to his advisor, Professor Karlheinz E. Woehler, for his advice, encouragement and guidance in the preparation of this thesis.

I. INTRODUCTION

The following analysis examines several factors that limit the detection performance of a passive homing torpedo with the mission objective of countering shallow-draft targets in Norwegian coastal waters. Generally, these factors can be divided into three main groups:

- Environmental factors in the ocean
- Electrical mechanical and hydrodynamical factors in the torpedo system
- The users tactical situation

The factors that are generated in the ocean itself are the principal subject of this analysis. As our interest is confined to the layer immediately below the surface of the ocean, later called the subsurface ocean layer, the main factors affecting the sound propagation are:

- Scattering and absorption due to the bubble-dominated inhomogeneous subsurface ocean layer.
- Scattering from the rough sea surface

The concentration of air bubbles and the roughness of the sea surface are determined by the windspeed. The effectiveness of both these scattering mechanisms depends on the frequency of the incident wave and the geometry of the source and receiver. The following analysis is limited to

high frequencies in the region of 30-60 kHz which are characteristic of existing torpedo systems. At high frequency and low grazing angles for the incident and received signals, the phenomena of "shadowing" of the surface by other parts of the boundary occurs. Under these conditions, the effect from the inhomogeneous subsurface ocean layer becomes increasingly important. Obviously both the above mentioned scattering mechanisms are present simultaneously. Often these two effects cannot be resolved either theoretically or experimentally, as any signal with a finite duration will be scattered from the space near the surface simultaneously with that from the sea surface itself.

In order to adequately describe the scattering mechanisms, this analysis starts with a presentation of the oceanographic background material for:

- Typical windspeed and wave height
- Typical sound speed profiles
- Density and distribution of air bubbles in the subsurface layer
- Statistical description of the sea surface

The analysis proceeds by separately estimating the effect of:

- Scattering from a randomly rough surface
- Scattering and absorption caused by an inhomogeneous subsurface layer,

and comparing their relative importance. The method employed for these estimations is an approximation that is a combination of both ray and wave theories. Ray methods are used to follow the acoustic signal from its source to the vicinity of the scatterer. Wave theory is used to calculate the actual scattering process. Finally, ray theory is again used to follow the scattered signal to the receiver.

An idealized propagation model consisting of an isotropic stratified medium will be used as reference of comparison. This model is founded on:

- A noise source from a cavitating propeller blade.
- The operational characteristics for a square law detector (ROC-curves).
- A transmission loss model based on geometrical spreading and absorption losses in homogeneous sea water.

In this analysis, the passive sonar equation is used to predict the performance of the homing system. The detection range encountering the two scattering effects will be obtained from the sonar equation and compared to the detection range based on the reference model. Thus, the difference in ranges at which the homing device just acquires the target with and without scattering is a measure of efficiency.

II. SCENARIO AND TORPEDO RUN GEOMETRY

In the Norwegian coastal waters, the primary mission of a torpedo system is to counter an amphibious force consisting of escorts, supply ships, and shallow-draft landing crafts. Typical characteristics of these three ship types are as follows:

Supply ships:

- Displacement 5000 tons
- Length 100 m.
- Draft 6 m.
- Speed 15-20 kts.

Escort ships:

- Displacement 2000-3000 tons
- Length 85 m.
- Draft 3 m.
- Speed 35 kts.

Landing craft:

- Displacement 1000 tons
- Length 80 m.
- Draft 2 m.
- Speed 18 kts.

In order to simplify this analysis, moderate sea states (SS 3) are assumed. Since "moderate" wave heights of two meters

are appreciable when compared with the two-meters draft of the landing craft, the possibility of an acoustic torpedo impacting the target at a depth of two meters is very remote without the use of an influence exploder.

Two relevant search and attack schemes will be considered. These are illustrated in Fig. 1 together with the operation of the influence exploder. From target validation to completion of terminal attack, the torpedo continuously tracks in the azimuth plane. In Case A, ascent is inhibited after enable. For Case B, ascent is inhibited after the torpedo reaches terminal attack depth.

An assumed attack depth of six meters is consistent with the activation range of influence exploders and is deep enough to preclude wave or "free surface" induced disturbances of the torpedo. Success of the attack depends primarily on the availability of maintaining azimuth-plane steering to within a short horizontal range of the target, and the subsequent operation of the influence exploder.

Case A is of particular interest to this analysis, as both the search and attack-depth are within the subsurface layer.

III. OCEANOGRAPHIC BACKGROUND MATERIAL

The oceanographic background for predicting typical and extreme conditions of

- wind speed
- wave heights
- bubble densities and distributions
- ambient noise versus self noise
- sound speed profiles

are outlined in detail in Appendix A. Even though most data have general validity for Norwegian coastal waters, the region above 68°N are of particular interest. Thus, a typical area combining open as well as confined waters can be represented by "Andfjord" at 70°N , where the oceanographic conditions can be related to the weather station "Andenes," see Fig. 2.

Figures 3 and 4 [Ref. 1] show average windspeed and the occurrence of significant wave heights as a function of time of year at weather station "Andenes," respectively. The bulk of data is centered around a windspeed of Beaufort:4-5 (11-21 kts) and SS:3-4 (significant wave heights: 1-2 m). Table I gives the relationship between SS, windspeed and expected significant wave heights.

TABLE I
 RELATIONSHIP BETWEEN SEA STATE (SS), WIND SPEED,
 AND EXPECTED SIGNIFICANT WAVE HEIGHTS (H_s)

Class Number	Significant Wave Height in m	Beaufort Scale
SS	H_s	
0	0	0
1	0 - 0.1	1
2	0.1 - 0.5	2
3	0.5 - 1.25	3-4
4	1.25 - 2.5	5
5	2.5 - 4.0	6-7
6	4.0 - 6.0	8
7	6.0 - 9.0	9-10
8	9.0 - 14.0	11
9	>14	12

This, together with the low probability of having an amphibious operation occurring in high sea states ($SS > 5$) justifies the assumption of moderate sea state with wind-speed in the region of 12 kts and wave heights of 2 m.

The bubble data distribution taken from Ref. 2 was obtained in the area "Tromsö" - "Björnöya" during the period June-November 1978. These data correlate very well with a larger body of data obtained by H. Medwin [Ref. 3].

Figures 5, 6 and 7 [Ref. 2] show the density of resonant bubbles as a function of depth with windspeed as parameter for the 12, 38 and 120 kHz. As seen from these figures, the number of resonant bubbles are an increasing function of frequency and windspeed, and a decreasing function of depth. Below a depth of approximately 15 m, the number of bubbles is negligible for the windspeed of interest.

The effect of SS (windforce) on the ambient noise level is given in Fig. 8 [Ref. 4]. Shallow coastal Norwegian waters are typically 5-10 dB noisier than the corresponding deep water. However, great variability caused by local ship traffic, fishing fleet activity, marine life and local wind conditions makes ambient noise prediction difficult in these areas. This means that for accurate modeling, ambient noise prediction have to be done at each location as its level is both site and time dependent. However, Fig. 8 shows that for frequencies higher than 50 kHz, the

effect of windforce on the ambient noise level decreases to a lower bound determined by the thermal agitation. Based on the above discussion and experience related to noise levels for torpedo systems, the self noise will be assumed to be dominant through this analysis.

Figure 9, obtained from Ref. 5, shows that the sound speed profiles usually encountered in the area of interest results in extremely difficult sonar conditions. This is illustrated in Figs. 10 and 11, which show worst-case ray path derived from Fig. 9. In addition, the presence of bubbles in the subsurface layer causes the sound speed to be a function of frequency. The above two factors may frequently be the ones limiting the detection range of the torpedo. These effects can be minimized by selecting an appropriate search depth for a particular sound speed profile. In addition, for Case B the corresponding curved homing trajectories in the pitch plane give an error in apparent range to target. This effect will normally be taken into account by devising appropriate attack logic which is outside the scope of the present analysis.

IV. THE PASSIVE SONAR EQUATION

A measure of efficiency for a passive homing torpedo is the detection range obtained by solving the passive sonar equation for broadband noise:

$$SL+10\log B-TL(\text{geom})-\alpha R+DI-NL-DT=0 \quad (1)$$

where

SL = spectral level of the broadband noise radiated by the target (in dB re $1\mu\text{Pa}/\text{LHz}$ at 1m).

R = detection range (in m).

α = attenuation coefficient at the center frequency (in dB/m).

DI = receiving sensitivity (directivity index) (in dB re $1\mu\text{Pa}$).

NL = noise level at the receiver in the bandwidth B (in dB re $1\mu\text{Pa}$).

DT = detection threshold; the signal to noise ratio at the transducer output required for a detection probability of p_D and associated false alarm probability p_{FA} (in dB).

V. REFERENCE MODEL

A. INTRODUCTION

In order to produce the reference for the analysis the sonar equation is solved assuming ideal free-field conditions, a simple noise source model, and a generalized square-law detector.

B. IDEALIZER TRANSMISSION LOSS MODEL

Because the presence of refraction, scattering, and of ocean boundaries, free-field conditions associated with homogeneous (isovelocity) and unbounded medium seldom exist in the sea. However, as a basis for comparison, the ubiquitous spherical spreading law plus an added loss term due to "normal absorption" can be used as a reference model for measuring the effects of the previous mentioned scattering and absorption mechanisms. Thus, the reference transmission loss model can be expressed as:

$$TL=20\log R + \alpha R \quad (2)$$

where the absorption coefficient, expressed in dB/m, can be obtained from Fig. 14 taken from Ref. 8.

C. NOISE SOURCE MODEL

1. General Characteristics of Noise Sources

Sound is generated in a fluid medium by any process that causes an unsteady pressure field. Physically processes that can cause an unsteady pressure field include:

- Pulsation of a boundary surface of the medium
- The action of a nonsteady source on the fluid
- Turbulent motion in the fluid
- Oscillatory temperatures

It can be shown, e.g., Ref. 10, that each source mechanism mathematically corresponds to a dominant order of multipole. If all sources are of such a nature that their time variation can be described by a Fourier Integral, it can be shown [Ref. 10] that the Helmholtz Equation is

$$\nabla^2 p_\omega(x) + \frac{\omega^2}{C^2} p_\omega(x) = -4\pi f_\omega(x) \quad (3)$$

$$= \frac{\partial Q_\omega(x)}{\partial t} + \nabla \cdot F_\omega(x) - \frac{\partial^2 T_{\omega ij}}{\partial x_i \partial x_j}$$

Term 1 Term 2 Term 3

where the right hand side describes distributed source terms.

The terms on the right hand side of Eq. (3) have the following interpretations:

- Term 1: mass injection
- Term 2: external force
- Term 3: turbulent shear stress

In the long distance and long wavelength approximation, it can be shown that the mass injection term gives rise to a simple source; a zero order pole called a monopole. The monopole radiates omnidirectional with no angular dependence. At large distances the pressure field from the monopole radiation is that of a point source. Examples of this are:

-Pulsating bubbles

-Cavitation

The external force, in the long distance and long wavelength approximation, is associated with a dominant dipole which has a cosine directional pattern. Examples of this type of radiation is that caused by the vibratory motion of an un baffled rigid body.

Radiation from turbulent shear stresses is characterized by a lowest order term of quadrupole nature.

The efficiency of the source terms decreases with increasing dependence on the spatial derivatives. This can be understood when recognizing that wave functions of the general form $f(x-ct)$ have a time derivative

$$\left| \frac{\partial}{\partial t} f(x-ct) \right| = c f_t(x-ct) \quad (4)$$

which is magnitude c (sound speed) greater than the spatial derivative

$$\left| \frac{\partial}{\partial x} f(x-ct) \right| = f_x(x-ct) \quad (5)$$

Other factors being equal, the radiation from an external force is small compared to that from mass injection, and that from turbulent shear stress is the smallest; therefore, monopole radiation is the dominant term.

Propeller cavitation, when it occurs, is usually the dominant noise source for any marine vessel. Submarine and torpedoes often operate at a depth great enough to avoid cavitation. Surface ships, on the other hand, generally have well developed propeller cavitation with the result that their radiated spectrum from 5 Hz to 100 kHz is controlled by this source.

The basic phenomena of cavitation combined with propeller hydrodynamics give the fundamental characteristics of propeller cavitation noise. An excellent qualitatively discussion of this can be found in Ref. 9:Chs. 7 and 8, from which the following is extracted:

Propeller blades are rotating twisted wings that produce hydrodynamic forces. Depending on operating conditions, they experience cavitation on a number of different places. Of these there are three prominent types:

- Tip vortex cavitation
- Hub vortex cavitation
- Surface blade cavitation

In addition to the two types of vortex cavitation, there normally are two types of blade surface cavitation:

-Back: driving face

-Front: suction surface

Of all kinds of propeller cavitation, surface blade cavitation on the suction surface is normally the most noisy, while hub vortex cavitation is the least noisy.

2. The Noise Source Model

Due to lack of recorded and available noise data from the target in question, the noise source has been generalized on the basis of the following discussion and assumptions:

The noise source will be build up around a surface blade cavitating propeller operating in a good to poor wake; surface cavitation will be assumed to be dominant.

D. Ross [Ref. 9] has developed an approximate theory for cavitation noise, where dimensional analysis is combined with the basic results of cavitation theory that the acoustic pressure is proportional to the product of the collapse pressure of the cavities and the volume of cavitation produced per unit time. From this synthesis it is found that the total acoustic intensity varies as:

$$I \approx K_{ti} \frac{p_o b s D (U_{ti})^3}{r^2} \left[\left(\frac{U_t}{U_{ti}} \right) \left(\frac{U_t}{U_{ti}} - 1 \right)^2 \right] \quad (6)$$

where

r = distance of the hydrophone from the source

K_{ti} = the cavitation inception parameter

U_t = blade tip speed

U_{ti} = blade tip speed for inception of cavitation

This expression shows that propeller cavitation noise power is proportional to the total number of blades, b , the blade chord, s , and to the propeller diameter, D , and is a function of the tip speed with the dependence on the tip speed being the strongest. The different blade surface sections where cavitation exist are uncorrelated and the radiated noise is treated as a single monopole radiation so that at a distance $r \gg a$ (where a is the characteristic dimension on the source region) the radiation is similar to that of a point source with no angular dependence.

Submarines and torpedoes with centerline propellers have a relatively symmetric inflow condition. Surface ship propellers, in contrast, operate under nonuniform inflow conditions. Circumferential wake variation causes the radiated sound to be amplitude modulated at the blade rate frequency. Furthermore, slight physical difference between the blades produces modulation at the shaft rate frequency. These amplitude variations gives a very distinct characteristic to the radiated noise that can be used for classification purposes to reduce the probability of false alarm.

The most complete source of data on surface ship radiated noise are measurements made during WWII, reported

in a compendium issued by the U.S. Office of Scientific Research and Development (OSRD) in 1945 and declassified in 1960. When these data are examined the radiated noise is found to depend on tip speed and the number of propeller blades with little dependence on the other variables. For surface ships near cruise speed, the source level for frequency over 100 Hz can be written as:

$$SL = SL' + 20 - 20 \log f; \quad f > 100 \text{ Hz} \quad (7)$$

where

f = frequency in Hz

SL' = overall source level in dB re $1 \mu\text{Pa}$.

The overall level can be expressed as:

$$SL' = 175 + 60 \log U / 25 + 10 \log b / 4 \quad (8)$$

where

$$U = \pi n D \quad (9)$$

n = rotational speed (rpm)

D = diameter of the propeller (m).

The above expressions are used as the basis for the noise model with the following input data:

n = 300 rpm for maximum cruise speed of 15 kts.

n = 180 rpm for a cruise speed of 10 kts.

D = 2 m.

b = 5.

The resulting noise spectrum, in dB re $1 \mu\text{Pa}$ at 1 m, as a function of speed in kts. are tabulated in Table II.

TABLE II

SOURCE LEVEL DATA AND CALCULATION
FOR A BLADE SURFACE CAVITATING PROPELLER

Rotational Frequency	Diameter of Propeller	Tip Speed	Advance Speed	Overall Level	Average Source Level
n rpm	D m	U_t m/s	U m/s	SL' dB re 1 μ Pa	SL dB re 1 μ Pa
300	2	31.4	15	182	106.0
180	2	18.9	10	168.6	93.0

and plotted in Fig. 15. A one sigma region (5 dB of uncertainty) is incorporated in Fig. 15.

The above noise spectrum estimation agrees very well in the high frequency limit, with more recent studies by A. Lövik [Refs. 11 and 12]. Here it is found that the cavitation spectra, both theoretically and experimentally, can be divided into four frequency regions, as illustrated in Fig. 16.

Region I is dominated by noise at the blade frequency and its harmonics. The emitted sound is caused by the volume variation of the main cavity.

Region II starts at the bubble frequency, which is the reciprocal of the lifetime of the main cavity. The mean power level is found to decrease with increasing frequency as $f^{-2.5}$.

Region III is an intermediate region.

Region IV associated with the shock waves starts at the mean collapse frequency f_c , given by the mean collapse time. The power level is found to decrease as f^{-2} , as in Eq. 5.

The number of gas bubbles in the water have a pronounced effect on the high frequency cavitation noise from the propeller. This is illustrated in Fig. 17, obtained from Ref. 12, where the power is found to decrease as much as 40 dB with increasing gas content.

Scaling laws are developed [Ref. 12] for each region based on a series of models and full scale measurements. These laws depend on the dynamic pressure induced by the propeller, the model ratio, and the gas content of the water. The full scale measurements were performed in cooperation with the Royal Norwegian Navy and the Marine Institute of Norway. The model experiments were performed in the largest cavitation tunnel at the Ship Research Institute of Norway.

In summary, the scaling of cavitation noise was demonstrated to be a useful tool in predicting a full scale cavitation noise as shown in Fig. 18 [Ref. 12] which compares measured noise spectra for the model and full scale measurements.

For the high frequency region, the source levels are of the same magnitude as predicted by the WWII empirical formula.

D. PASSIVE MODE RECEIVER CHARACTERISTICS

1. Assumptions

For receiver characteristics assume a square law detector with a center frequency f_c of 60 or 30 kHz and a bandwidth B . The detection scheme is shown in Fig. 16. The principal assumptions employed in the derivation are as follows:

- Gaussian signals in Gaussian noise
- Frequency independent signal and noise spectra

-Integration time T is sufficiently long to permit application of the central limit theorem.

2. Derivations

The detector input $r(t)$ is assumed to be a zero-mean Gaussian process composed of noise alone or signal plus noise expressed by the two well known hypotheses

$$H_0 r(t) = n(t) \quad (10)$$

$$H_1 r(t) = s(t) + n(t)$$

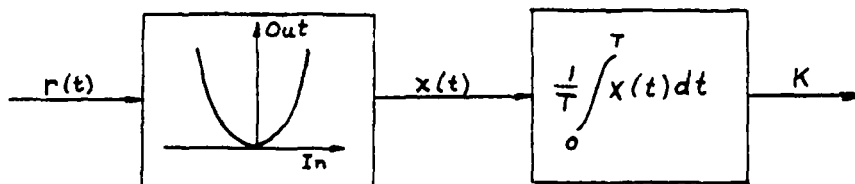
where:

$n(t)$: noise signal

$s(t)$: signal.

The two signals $s(t)$ and $n(t)$ are assumed to be independent.

Assume that the spectral shape of $s(t)$ and $n(t)$ are the same, such that H_0 and H_1 only differ in the total power level. Then the detector-smoother have the form:



Schematic of detector-smoother

and

$$x(t) = r^2(t) \quad (11)$$

Furthermore, let the noise variance be normalized to unity (for convenience) and the signal variance be denoted by σ^2

$$\text{Var}[n(t)] = 1 \quad (12)$$

$$\text{Var}[s(t)] = \sigma^2$$

Because of the assumed similarity in the spectral shapes, the autocorrelation functions are

$$R_n(\tau) = F^{-1}[N(f)] = \rho(\tau); \quad N(f) \text{ is the noise power spectral density} \quad (13)$$

$$R_s(\tau) = \rho(\tau) \sigma^2$$

$$R_n(\tau) = H_0 \rho(\tau) + H_1 (1 + \sigma^2) \rho(\tau)$$

Furthermore, assume that the integration time T is long enough so the central limit theorem holds, implying that K also is a Gaussian random variable.

This yields that the probability density function of the output variable and hence the detection and false alarm probabilities are completely determined once the mean and the variance of K are derived.

If a process $V(t)$ is wide-sense stationary, then

$$E[V(t)] = E\left[\frac{1}{T} \int_0^T V(t) dt\right] = \frac{1}{T} \int_0^T E[V(t)] dt = v \text{ (constant)} \quad (14)$$

Thus, assuming that $r(t)$ is a wide-sense stationary process.

$$E[K] = E[x(t)] = E[r(t)] = 1 + \sigma^2 \quad (15)$$

and similarly

$$\text{Var}[V] = E[V^2] - \{E[V]\}^2 = \frac{1}{T^2} \iint_{00}^{TT} E[V(t)V(s)] dt ds - v^2 \quad (16)$$

$$\text{Var}[V] = \frac{1}{T^2} \iint_{00}^{TT} [R_V(t-s) - v^2] dt ds = \frac{1}{T^2} \iint_{00}^{TT} \text{Cov}_V(t-s) dt ds$$

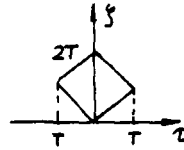
where $\text{Cov}_V(t-s)$ is a covariance function.

Then letting

$$\tau = t-s$$

$\zeta = t+s$, and substituting into Eq. (7) yields

$$\text{Var}[V] = \frac{1}{T^2} \iint_0^T \text{Cov}_V(\tau) \frac{d\zeta d\tau}{2}$$



$$\text{Var}[V] = \frac{1}{T} \int_{-T}^T \left[1 - \frac{|\tau|}{T}\right] \text{Cov}_V(\tau) d\tau \quad (17)$$

Consequently

$$\text{Var}[K] = \frac{1}{T} \int_{-T}^T \left[1 - \frac{|\tau|}{T}\right] \text{Cov}_V(\tau) d\tau \quad (18)$$

Then, evaluating the covariance function from the auto-correlation function

$$R_X(\tau) = E[x(t)x(t-\tau)] = E[r^2(t)r^2(t-\tau)] \quad (19)$$

Since $r(t)$ is Gaussian, the above fourth moment can be expressed as product and sums of second moments:

$$R_X(\tau) = \overline{r^2(t) \cdot r^2(t+\tau)} + 2\overline{r(t)r(t-\tau) \cdot r(t)r(t-\tau)}$$

$$= R_r^2(0) + 2R_r^2(\tau)$$

$$R_X(\tau) = (1+\sigma^2)^2 + 2(1+\sigma^2)^2 \rho^2(\tau) \quad (20)$$

Thus, the covariance function is

$$\begin{aligned} \text{Cov}_X(\tau) &= R_X(\tau) - \{E[x(t)]\}^2 \\ &= (1+\sigma^2)^2 + 2(1+\sigma^2)^2 \rho^2(\tau) - (1+\sigma^2)^2 \end{aligned}$$

$$\text{Cov}_x(\tau) = 2(1+\sigma^2)^2 \rho^2(\tau) \quad (21)$$

Inserting Eq. (12) into Eq. (9) yields

$$\begin{aligned} \text{Var}[K] &= \frac{1}{T} \int_{-T}^T \left\{ \left[1 - \frac{|\tau|}{T} \right] 2(1+\sigma^2)^2 \rho^2(\tau) \right\} d\tau \\ \text{Var}[K] &= \frac{2(1+\sigma^2)^2}{T} \int_{-T}^T \left[1 - \frac{|\tau|}{T} \right] \rho^2(\tau) d\tau \end{aligned} \quad (22)$$

If T is large compared to the correlation time

$$TB \gg 1$$

then we can substitute the limit for Eq. (22) by

$$\begin{aligned} \text{Var}[K] &= \frac{2(1+\sigma^2)^2}{T} \int_{-\infty}^{\infty} \rho^2(\tau) d\tau \\ &= \frac{2(1+\sigma^2)^2}{T} \int_{-\infty}^{\infty} N^2(f) df \end{aligned} \quad (23)$$

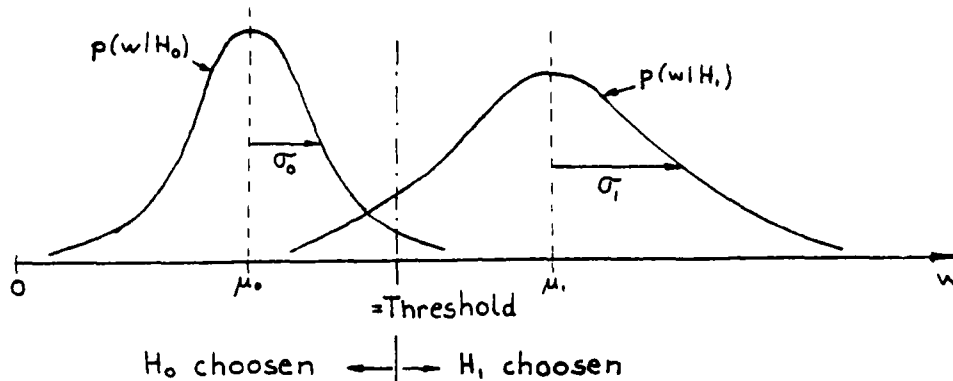
If we further make the assumption that the signal and noise have ideal flat bandpass spectra:

$$N(f) = \begin{cases} 1/2B, & f-B/2 < f < f+B/2 \\ 0, & \text{otherwise,} \end{cases} \quad (24)$$

Inserting Eq. (24) in Eq. (23) yields

$$\text{Var}[K] = \frac{(1+\sigma^2)^2}{BT} \quad (25)$$

The probability density function for the output of the detector have the following form



Here w is the outcome of all possible signals. The false alarm probability is obtained by integrating the conditional probability $p(w|H_0)$ over the outcome space for which to choose H_1 .

$$P_{FA} = \int_j^{\infty} p(w|H_0) dw = Q\left(\frac{j - \mu_0}{\sigma_0}\right) \quad (26)$$

Similarly, the miss probability = 1 - detection probability is obtained by integrating the conditional probability $p(w|H_1)$ over the outcome space for which to choose H_0 .

$$P_M = 1 - P_D = \int_{-\infty}^j p(w|H_1) dw = Q\left(\frac{\mu_1 - j}{\sigma_1}\right) \quad (27)$$

Further defining the input and output signal-to-noise ratios as

$$S/N(\text{input}) = \frac{\sigma^2}{1} = \sigma^2 \quad (28)$$

$$S/N(\text{output}) = \frac{(\mu_1 - \mu_0)^2}{\sigma_1^2} \quad (29)$$

For the square law detector where

$$\mu_0 = E[n^2(t)] = 1, \quad \mu_1 = E[r^2(t)] = E[K] = 1 + \sigma^2 \quad (30)$$

$$\begin{aligned} \sigma_0^2 = \text{Var}[n^2(t)] &= \frac{1}{BT}, \quad \sigma_1^2 = \text{Var}[r^2(t)] \\ &= \text{Var}[K] = \frac{(1 + \sigma^2)^2}{BT} \end{aligned}$$

The output signal-to-noise ratio:

$$S/N(\text{output}) = \frac{(1 + \sigma^2 - 1)^2}{\left[\frac{(1 + \sigma^2)^2}{BT}\right]} = \frac{BT \sigma^4}{(1 + \sigma^2)^2} \quad (31)$$

The input signal-to-noise ratio:

$$S/N(\text{input}) = \sigma^2 \quad (32)$$

The probability of false alarm:

$$P_{FA} = Q[\sqrt{BT}(j-1)] \quad (33)$$

The probability of detection:

$$P_D = 1 - Q\left[\sqrt{BT} \left(\frac{1 + \sigma^2 - j}{1 + \sigma^2}\right)\right] \quad (34)$$

The Equations (32), (33), and (34) are plotted for a variety of realistically encountered conditions. Figure 17 gives BT versus $S/N(\text{in})$ (identical to the detection threshold DT) for various combinations of p_D and P_{FA} .

Figure 18 gives p_D versus $S/N(\text{in})$ for various combinations of the threshold j and P_{FA} . This constitutes the ROC-curves for the generalized square law detector.

E. REFERENCE DETECTION PERFORMANCE

1. Introduction

As both the scattering and absorption are frequency dependent, it is necessary to have reference models for both 60 and 30 kHz.

2. 60 kHz Case

The range dependent portion of the sonar Equation (1):
$$-20 \log r - \alpha R$$

is plotted in Fig. 19 for $\alpha = 0.021$ dB/m taken from Fig. 14.

Figures 15, 17 and 19 are then used to estimate the detection range:

- (a) Select p_D , p_{FA} , B , and the integration time T .
The detection threshold $DT = S/N(\text{input})$ is then found from Fig. 17.
- (b) Select the speed of the target and find the SL from the noise source model (Fig. 15). Then, reasonable values for the receiver sensitivity DI and the self noise level NL yields the left hand side of the sonar equation (1) except for range dependent term.
- (c) Use Fig. 19 to solve the passive equation for R .

A realistic example may illustrate the above procedure.

(a) Entering Fig. 17 with

$$P_D = 0.5$$

$$P_{FA} = 10^{-6}$$

$$B = 4500 \text{ Hz}$$

$$T = 100 \text{ msec}$$

yields.

$$DT = -6.5 \text{ dB.}$$

(b) Selecting a target speed of 12 kts. gives

(from Fig. 15) $SL=100 \text{ dB}$. Selecting a

typical transducer sensitivity $DI = -180 \text{ dB}$.

Assuming the NL to be dominated by self noise of typical value $NL=-124 \text{ dB}$. This yields

$$SL+10\log B+DI-NL-DT=87 \text{ dB.}$$

(c) Figure 19 with

$$-20\log R-0.02R=-87$$

yields

$$R=1200 \text{ m. for } a=0.02 \text{ dB/m and } f=50 \text{ kHz.}$$

The influence of different design parameters like self noise and detection threshold on the passive detection performance is now easily investigated by the above procedure.

Although outside the main scope of this analysis, the above statement can be confirmed with an example. As seen from Fig. 18, a probability of false alarm $P_{FA} = 10^{-6}$ implies a threshold setting = 0.9 dB above the noise level.

Due to the variability of the noise level together with the practical difficulty in accurately setting the threshold, a more realistic goal for the threshold would typically be 3 dB. Going into Fig. 17 shows that the corresponding value for DT for $p_D = 0.5$ is $DT = 0$ dB, with a corresponding low value for the p_{FA} .

Letting $DT=0$ dB and keeping the previous assumed values of SL, DI, and NL yields:

$$SL+10\log B+DI-NL-DT=80.5 \text{ dB.}$$

The corresponding detection range is:

$$R = 1000 \text{ m, for } \alpha = 0.02 \text{ dB/m and } f = 60 \text{ kHz.}$$

Thus, this change in threshold setting caused a decrease in detection range from 1200 m to 1000 m in return of a significant decrease in the false alarm probability.

3. 30 kHz Case

In order to estimate the reference detection range for an operating frequency of 30 kHz, we utilize the sonar equation (1).

Assume that the receiver has the same generalized passive detector characteristics as in the 60 kHz case:

$$DI = -180 \text{ dB}$$

$$NL = -124 \text{ dB.}$$

$$DT = -6.5 \text{ dB, based on } p_D = 0.5 \text{ and } p_{FA} = 10^{-6}.$$

However, the empirical equation (7) for the source level:

$$SL=SL'+20-20\log f$$

shows that the source level falls off as f^{-2} . If the dynamical and dimensional parameters of the propeller are the same, SL will increase by +6 dB when the frequency is reduced from 60 to 30 kHz.

A source level of

$$SL=100+5=106 \text{ dB}$$

gives a range dependent solution of the sonar equation

$$-20\log R - \alpha R = -87 - 6 = -93 \text{ dB.}$$

A plot of

$$-20\log R - \alpha R$$

is given in Fig. 20 for an absorption coefficient $\alpha=0.01$ dB/m taken from Fig. 14.

Figure 20 then gives a detection range of

$$R = 2400 \text{ m.}$$

Thus, as seen from these ideal reference calculations, halving the frequency gives a higher source level and a lower absorption loss, resulting in a doubling of the detection range.

VI. THE EFFECT OF SURFACE SCATTERING

A. OCEANOGRAPHIC DESCRIPTION OF THE SEA SURFACE

The roughness of the sea surface is the essence of the scattering mechanism. Thus, to adequately describe the scattering of sound from a randomly rough sea surface, it is necessary to formulate a suitable description of the sea surface from an acoustical propagation point of view.

Generally the shape of the rough sea surface is most appropriately described in terms of time and spatial dependent random variables. However, observation of the ocean under the same environmental (meteorological) conditions indicates that the roughness is the same over large areas and for periods of at least several hours. The random processes responsible for the structure of the sea surface, therefore, can be considered stationary at least over periods of hours. With this assumption, the sea surface can be described in terms of the statistical description of the surface displacement function, and the distribution of signals reflected from the sea surface can then be related to this probability distribution function.

The most significant statistical parameters describing the scattering mechanism from the randomly rough surface are:

- the mean square slope
- the mean square surface height
- the correlation length.

Optical measurements made at sea by C. Cox and W. Munk [Ref. 13] showed that the sea surface with an arbitrary wide continuous spectrum of waves is characterized by a Gaussian distributed surface slope. The mean square slope, determined from these optical measurements is

$$\langle \zeta'^2 \rangle = \Sigma^2 = (3+5.12w) \times 10^{-3} \quad (35)$$

where

W=wind speed in m/s measured 41 ft (12.5 m) above
the sea surface.

The Gaussian distribution of surface slopes implies that the surface displacement function can be described by a Gaussian probability density function with zero mean

$$\langle \zeta \rangle = 0$$

and variance

$$\langle \zeta^2 \rangle = \sigma^2$$

and Gaussian correlation function

$$\langle \zeta(t)\zeta(t+\tau) \rangle$$

The mean square height σ^2 , is obtained by integrating the frequency spectrum of the fully developed sea. The frequency spectrum G is given by the commonly accepted semi-empirical expression of Pierson-Moskowitz [Ref. 14] as

$$G(\Omega) = \frac{\alpha g^2}{\Omega^5} \exp\left[-\beta \frac{\Omega}{\Omega_0}\right]^4 \quad (36)$$

where

Ω = frequency (in s^{-1})

$\alpha = 8.1$

$\beta = .74$

$\Omega_0 = g/W$ (in s^{-1}).

W = wind speed in m/s at 19.5m above the sea surface

g = gravitational acceleration (in m/s^2).

This gives

$$\sigma^2 = \int_0^{\infty} G(\Omega) d\Omega = \frac{\alpha W^4}{4\beta g^2} \quad (37)$$

For a Gaussian autocorrelation function expressed as

$$\psi(\tau) = \frac{1}{\sigma^2} \langle \zeta(t)\zeta(t+\tau) \rangle = e^{-\tau^2/T^2} \quad (38)$$

where

T = correlation length.

The following relationship for the mean square height holds for sea of small roughness

$$\Sigma^2 = \frac{2\sigma^2}{T^2}, \text{ see later Eq. (60)} \quad (39)$$

and the correlation length is thus:

$$T = \sqrt{2} \frac{\sigma}{\Sigma} \quad (40)$$

B. SCATTERING THEORY

All real boundaries are rough for radiation with short enough wavelength, and the apparent roughness depends on the "viewing" conditions. The wave reflected by a plane surface has the same properties as the incident wave since the radiation is scattered coherently and there is a definite relation between the incident and scattered waves.

A randomly rough surface, however, such as the wind generated ocean surface, scatters radiation in all directions, i.e., an illuminated area is visible from any direction.

Heuristically there are two distinct approaches to this phenomena.

1. If the boundary is rough most of the radiation is scattered and there is little transmission in the specular direction. Thus, the attenuation caused by the irregularities can be included in the transmission equation.
2. If the surface is truly smooth, it can be assumed that the effect of the boundary is to supplement the original pressure field by an out-of-phase image contribution. For a randomly rough surface the reflected sound neither completely cancels the direct sound nor adds to give +6 dB pressure peaks of the interference pattern. For a rough surface, this supplement is a small fraction of the direct path.

The second approach will be used with the simplified assumption that the sea below the surface has an isotropic statistical description; i.e., the mean acoustic velocity and the mean density are assumed to be constant and have negligibly small mean square fluctuations.

The estimation of the scattering is based on an approximation method employing both ray and wave theory. Ray methods are used to follow the acoustic signal from the noise source to the vicinity of the sea surface. Then, wave theory is used to calculate the scattering process. Finally, ray theory is used to follow the scattered signal to the receiver.

The geometry is given in Fig. 24a. The origin of the coordinate system is at the center of the illuminated area. The x-y plane coincides with the mean of the rough surface as averaged over the illuminated area.

The source and receiver are at distances R_1 and R_2 , respectively, from the origin. R_1 is the xz-plane and makes the angle θ_1 with the z-axis. R_2 makes the angle θ_2 with the z-axis and the projection of R_2 on the xy-plane has an angle θ_3 relative to the x-axis.

For high frequencies R_1 and R_2 are much larger than the acoustic wavelength. Then both the incident wave and scattered waves can be treated as nearly plane waves.

The formulation of the scattering problem will be based on the Helmholtz integral which requires known values of the normal derivatives of the incident and reflected waves on the boundary. These are estimated by using the heuristic Kirchhoff's approximation, which assumes that the wave is locally reflected by a plane surface; i.e., an approximation restricted to a surface not too rough and not shadowed.

Further, the receiver directivity, as indicated by Fig. 24b, will be used to limit the surface area that is illuminated.

Since this procedure is based on a detailed development by I. Tolstoy and C. S. Clay [Ref. 15], only the main points will be outlined here to bring out the assumptions made and the inherent limitations of this approach.

The development starts by considering the inhomogeneous wave equation of the general form:

$$\nabla^2 p(\vec{x}_1, t) - \frac{1}{c^2} \frac{\partial^2 p(\vec{x}_1, t)}{\partial t^2} = -4\pi f(\vec{x}_1, t) \quad (41)$$

where

$f(\vec{x}_1, t)$ = is a known source distribution.

The development is based on the following initial assumptions:

- The medium is homogeneous.
- The medium is bounded by some surface S , onto which an incident wave impinges.

-The boundary is characterized by the specific acoustic admittance and the shape of the boundary.

-The incident wave is harmonic.

The assumed harmonic source implies that $f(\vec{x}, t)$ can be decomposed into a Fourier integral. Furthermore, assuming that the solution of Eq. (41) can be decomposed in time, we arrive at the Helmholtz equation

$$\nabla^2 p_\omega(\mathbf{x}) + \frac{\omega^2}{c^2} p_\omega(\mathbf{x}) = -4\pi f_\omega(\mathbf{x}) \quad (42)$$

It should be noted here that L. Fortuin, in [Ref. 16] showed that the Helmholtz equation is not exactly correct for a medium with a time dependent boundary. The equation can, however, be used with a good approximation when the time derivative of the surface elevation is much smaller than the speed of the waves through the medium. For underwater sound waves scattered by the rough sea surface, this means that the wind speed has to be much less than the sound speed; a requirement easily fulfilled for our investigation.

Green's method allows the solution of this linear inhomogeneous wave equation to be expressed in the heuristic Helmholtz integral form:

$$p_\omega(\mathbf{x}) = \int_V f_\omega(\mathbf{x}^1) G_\omega(\mathbf{x}\mathbf{x}^1) d^3x^1 + \frac{1}{4\pi} \int_S \left\{ G_\omega(\mathbf{x}\mathbf{x}^1) \frac{\partial p_\omega(\mathbf{x}^1)}{\partial n^1} - p_\omega(\mathbf{x}^1) \frac{\partial G_\omega(\mathbf{x}\mathbf{x}^1)}{\partial n^1} \right\} da^1 \quad (43)$$

The first integral on the RHS of Eq. (43) contains the sound sources and the bulk (volume) scattering. The second integral represents the surface scattering and is taken over all finite surfaces.

Now, disregarding the direct path, the signal at the receiver is given by the surface integral alone:

$$p_{\omega}^{(s)}(x_2) = \frac{1}{4\pi} \int_S \left\{ G(x_2, x^1) \frac{\partial p_{\omega}}{\partial n^1} - p_{\omega}(x^1) \frac{\partial G}{\partial n^1} \right\} da^1 \quad (44)$$

where the subscript s denotes the scattered field. In order to solve Eq. (44) the following must be done:

- Give an approximate expression for the incident wave.
- Find an appropriate Greens function.
- Make an approximation for $p_{\omega}(x^1)$ and $\partial p_{\omega}/\partial n$ at the surface.

As we already have assumed a simple harmonic source, the incident wave can be expressed as:

$$p_{\omega}^{(i)}(x^1) = \left(\frac{\Pi pc}{2\pi} \right)^{1/2} \frac{D}{R} e^{ikR} \approx \frac{BD}{R} e^{ikR} \quad (45)$$

where

Π : power output.

D: illumination function.

Assuming $kr \gg 1$, i.e., that the distance of the source is large compared to the wavelength, the wave in the bounded ensonified area can be considered as a plane wave

characterized by its propagation vector

$$k_i = -k \frac{\vec{x}_i}{|\vec{x}_i|}$$

thus obtaining the expression for the incident wave:

$$p_w^{(i)}(\vec{x}_1) = \frac{BD}{R} e^{ikR_1} e^{i\vec{k}_i \cdot \vec{x}_1} \quad (46)$$

Further assuming that the receiver is sufficiently far removed from the scattering area with the rest of the sea surface not contributing, then the scattering area acts as a small induced source in a free space and we can approximate the propagation of the scattered waves from the ensonified region in terms of the free field Greens function:

$$G(x_2 x_1) \approx \frac{e^{ikR_2}}{R_2} e^{-i\vec{k}_s \cdot \vec{x}_1} \quad (47)$$

where

$$k_s = k \frac{\vec{x}_2}{|\vec{x}_2|}$$

We further assume that each surface element da^1 acts as a small reflector, and that the response of da^1 to the incident wave is that of a "local reaction," i.e., independent of any other part of the ensonified area A.

Then, the Kirchhoff's approximation where it is assumed that p and $\partial p / \partial n$ vanish everywhere on the surface except at the ensonified area and that the values of p and $\partial p / \partial n$ are proportional to the incident wave, allow the scattered

"target" strength for the ensonified area to be approximated as:

$$p_{\omega}(x^1) \Big|_A = R p_{\omega}^{(i)}(x^1) \quad (48)$$

$$\frac{\partial p}{\partial n^1} \Big|_A = R \frac{\partial p^{(i)}}{\partial n^1}$$

where

p is the locally reflected wave.

R = reflection coefficient.

$$= \frac{p^1 c^1 \cos \theta - p c \cos \theta^1}{p^1 c^1 \cos \theta + p c \cos \theta^1}; \quad \frac{c}{\sin \theta} = \frac{c^1}{\sin \theta^1}$$

Finally, assuming a Gaussian illumination function:

$$D = e^{-\frac{x^2}{X^2} - \frac{y^2}{Y^2}} \quad (49)$$

where

X and Y are the effective dimensions of the illuminated area.

The scattering integral based on the Kirchhoff's approximation can be expressed as:

$$p_{\omega}^{(s)}(x_2) = \frac{ikBe^{ik(R_1+R_2)}}{2\pi R_1 R_2} Rf(\theta_1 \theta_2 \theta_3) \iint_{-\infty}^{\infty} D e^{2i(\alpha x^1 + \beta y^1)} e^{2i\zeta(x^1 y^1)} dx^1 dy^1 \quad (50)$$

where

$$\alpha = \frac{k}{2} (\sin \theta_1 - \sin \theta_2 \cos \theta_3)$$

$$\beta = -\frac{k}{2} \sin \theta_2 \sin \theta_3$$

$$\gamma = \frac{k}{2}(\cos \theta_1 + \cos \theta_2)$$

$\zeta(x^1 y^1)$ = surface displacement function.

The above scattering integral is then applied to a randomly rough surface where the surface displacement function ζ is a random variable assumed to be represented by a Gaussian PDF expressed as

$$W(\zeta) = \frac{1}{\sigma\sqrt{2\pi}} e^{-\zeta^2/2\sigma^2} \quad (51)$$

with zero mean and variance σ^2 .

Also, assume that the surface is slowly varying so that the signal reflects from an essentially stationary surface and that the succession of received scattered signals p_n are assumed to form a statistically independent set of sample functions from which sequence N the first and second moment of the field can be investigated. Doing so Clay and Tolstoy [Ref. 15] found that the mean reflected signal can be expressed as

$$\langle p_\omega^{(s)}(x_2) \rangle_\zeta = p_0 e^{-2\gamma^2 \sigma^2} \quad (52)$$

where

$$p_0 = p_\omega^{(s)}(x_2) \Big|_{\zeta=0}$$

is the signal reflected by a mirror-like surface, other factors being the same.

It is seen from the above that

1. For $\sigma \rightarrow 0$, all displacements ζ have zero probability and the mean signal tends to p_0 . Furthermore, all elements contribute to the scattering coherently.
2. For $\sigma \gg k$, all displacements ζ are equally probable. **There** are large phase shifts between contributions from different surface elements and they tend to cancel each other and the scattering radiation is incoherent.

The second moment is defined as:

$$\langle s^2(t) \rangle \triangleq \frac{1}{T} \int_0^T s^2(t) dt = \langle pp^* \rangle_T - \langle \bar{p} \bar{p}^* \rangle_T \quad (53)$$

where

$$s^2(t) = \frac{1}{N} \left[\sum_{n=1}^N p_n^2(t) - N \langle p(t) \rangle_N^2 \right] \quad (54)$$

In this expression the operation of squaring the signal has to be considered. However, each surface element has a different ζ for a random surface. Thus, the probability of finding element $dx' dy'$ with ζ_1 , and element $dx'' dy''$ with ζ_2 is expressed in the bivariate distribution function assumed to be Gaussian and of the form:

$$W(\zeta_1 \zeta_2) = \frac{1}{2\pi\sigma^2(1-\psi^2)^{1/2}} e \left[-\frac{1}{2(1-\psi^2)\sigma^2} (\zeta_1^2 + \zeta_2^2 - 2\zeta_1\zeta_2\psi) \right] \quad (55)$$

where

$$\psi(\xi, \eta) = \frac{1}{\sigma^2} \langle \zeta_1(x' y' t) \zeta_2(x'' y'' t) \rangle \quad (56)$$

is the cross-correlation function characterizing the surface shape.

Changing to polar coordinate leads to Eq. 6.51 of Ref. 15 where:

$$\langle s^2 \rangle_\alpha \int_0^\infty D J_0(2\kappa r) [e^{-4\gamma^2\sigma^2(1-\psi)} - e^{-4\gamma^2\sigma^2}] r dr \quad (57)$$

Here J_0 is the Bessel function of zero order and x is the transformation parameter given as

$$\kappa = \frac{\alpha}{\cos \theta}$$

As seen from Eq. (57)

1. For rough surface, $\gamma^2\sigma^2$ is large and the second term in the bracket, the coherent part, is negligible.
2. For smooth surface, $\gamma^2\sigma^2$ is zero and the whole bracket is zero.

Since Eq. (57) cannot be integrated directly, Clay and Tolstoy [Ref. 15] consider it for small and large $\gamma\sigma$ separately.

Thus, concentrating on the high frequency limit, Clay and Tolstoy assumed $\gamma^2\sigma^2 \gg 1$ and showed that:

-The coherent component is negligible.

- $\langle s^2 \rangle \cong \langle pp^* \rangle$, as the means tends to zero,

$$\langle s^2 \rangle \cong \langle pp^* \rangle_\alpha \int_0^\infty J_0(2\kappa r) e^{-4\gamma^2\sigma^2(1-\psi)} r dr; \quad \gamma^2\sigma^2 \gg 1 \quad (58)$$

Equation (58) consists of the product of an oscillatory function and an exponential function. Because of the Bessel function, the main contribution to the integral is near $r=0$. Near $r=0$ the phase changes slowly and the expression can be evaluated by the method of stationary phase. Thus, the expression of ψ about $r=0$ is given as:

$$\psi \approx 1 + \psi''(0) \frac{r^2}{2} \quad (59)$$

Furthermore, Clay and Tolstoy show that $\psi''(0)$ can be related to the characteristics of the surface as:

$$|\psi''(0)| = \frac{1}{\sigma^2} \langle \zeta^{12} \rangle \quad (60)$$

Finally, Clay and Tolstoy show that the scattering signal can be expressed as:

$$\langle s^2 \rangle = \langle pp^* \rangle = \langle P_1 P_1^* \rangle \frac{A}{R_2^2} S_{hf}; \quad \begin{matrix} 4\gamma^2 \sigma^2 \gg 1 \\ (2\gamma^2 \langle \zeta^{12} \rangle) \gg \frac{1}{R^2} \end{matrix} \quad (61)$$

where

A = ensonified area

$\langle p_1 p_1^* \rangle$: the expected average value of p_1^2 , where p_1 is the incoming pressure to the illuminated area.

S_{hf} = scattering function

$$= \frac{f^2(\theta) R^2}{2\pi (\cos \theta_1 + \cos \theta_2)^2 \langle \zeta^{12} \rangle} e^{-\frac{x^2}{(2\gamma^2 \langle \zeta^{12} \rangle)}}$$

$$f(\theta) = f(\theta_1, \theta_2, \theta_3) = \frac{1 + \cos\theta_1 \cos\theta_2 - \sin\theta_1 \sin\theta_2 \cos\theta_3}{\cos\theta_1 + \cos\theta_2}$$

$$R = \frac{\rho^1 c^1 \cos\theta - \rho c \cos\theta^1}{\rho^1 c^1 \cos\theta + \rho c \cos\theta^1}; \quad \frac{c}{\sin\theta} = \frac{c^1}{\sin\theta^1}$$

$$\gamma = -\frac{k}{2} (\cos\theta_1 + \cos\theta_2)$$

$$\kappa = \frac{\alpha}{\cos\theta}$$

$$\alpha = \frac{k}{2} (\sin\theta_1 - \sin\theta_2 \cos\theta_3)$$

$$k = \frac{2\pi}{\lambda}$$

$$\langle \zeta^{12} \rangle = (3 + 5.12W) \times 10^{-3}; \quad W = \text{wind speed in m/s.}$$

Equation (61) is valid for:

$$4\gamma^2 \sigma^2 \gg 1$$

$$(2\gamma^2 \langle \zeta^{12} \rangle) \gg \frac{1}{R^2}$$

In summary, the reflection of high frequency signals yields scattered radiation which is incoherent. Furthermore, as pointed out by Clay and Tolstoy in [Ref. 15] although the radiation is primarily scattered in the specular direction, parts are scattered in all directions. As seen from Eq. (61) the scattering function S_{hf} is primarily dependent on the mean square slope of the surface $\langle \zeta^{12} \rangle$ and neither the mean square wave height σ^2 nor the correlation distance are important. Furthermore, it is noticeable that in the

high frequency limit the scattering function is independent of the frequency since

$$e - \frac{k^2}{(2\gamma^2 \langle \zeta^2 \rangle)} \rightarrow 1 \text{ when } r^2 \rightarrow \infty$$

C. GEOMETRICAL SHADOWING

The phenomena of shadowing of some surface areas by others has to be considered either when the surface irregularities are large with respect to the incident wavelength or when the grazing angle is small.

The few papers devoted to this subject are aimed mainly towards calculation of a "Shadowing function" based on the statistics of the surface.

An explicit method, geometrical shadowing, has been introduced by P. Bechmann [Ref. 17] where the shadowing function $S(\theta)$ is the probability that the point ζ (Fig. 25) is illuminated.

$$S(\theta) = \exp \left[- \int_0^{\infty} q(x) dx \right] \quad (62)$$

where:

$q(x)$ is the probability that ζ is shaded by ζ in the interval $(x, x+dx)$ given that it is not shaded in $(0, x)$.

This calculation of $S(\theta)$ only considers the elevation of the surface observation point. However, the slope also plays a role in that if its value exceeds $\cot\theta$ the point

will certainly be shaded. Thus, R. Wagner, in Ref. 18, incorporated both ζ and ζ^1 using P. Bechmann's method and found that the conditional probability that a point on the surface is illuminated, given that it has height ζ and slope ζ^1 , can be expressed as:

$$S(\theta_1 | \zeta_1, \zeta_1^1) = \exp\left[-\int_0^{\infty} q(x) dx\right] u(\cot\theta - \zeta^1) \quad (63)$$

where

u : is the unit step function.

$q(x)$: is the conditional probability that ζ is shadowed in the interval $(x, x+dx)$ given that it is not shadowed in $(0, x)$.

The function $q(x)$ cannot be calculated exactly. Thus, R. Wagner made the approximation that, for all x , the probability that ζ crosses the ray in dx is independent of the values of ζ and ζ^1 at $x=0$. In the above, no mention has been made of the direction of observation. However, in this respect, R. Wagner [Ref. 18] points out that in the high frequency limit only those portions of the surface which are illuminated simultaneously by rays in the direction of incidence and observation can contribute to the observed scattered power. For this condition, R. Wagner introduced both directions as independent variables in the so-called bistatic shadowing probabilities where he defines:

1. $S(\theta_1, \theta_2 | \zeta_1, \zeta_1')$ to be the conditional probability that the surface will not cross the incoming ray (Ray 1) or the outgoing ray (Ray 2) anywhere, given that both rays pass through an arbitrary point on the surface with displacement ζ and slope ζ' .
2. $S(\theta_1 | \theta_2, \zeta_1, \zeta_1')$ to be the conditional probability that the surface does not cross Ray 1, given that it does not cross Ray 2 and that both rays pass through the point ζ having slope ζ' .

Thus, the conditional shadowing function can be expressed as:

$$S(\theta_1, \theta_2 | \zeta_1, \zeta_1') = S(\theta_1 | \theta_2, \zeta_1, \zeta_1') S(\theta_2 | \zeta_1, \zeta_1') \quad (64)$$

The shadowing function is then obtained by averaging over all possible heights and slopes

$$S(\theta_1, \theta_2) = \iint_0^\infty S(\theta_1, \theta_2 | \zeta, \zeta') W(\zeta, \zeta') d\zeta d\zeta' \quad (65)$$

Here $w(\zeta, \zeta')$ is the bivariate PDF of the surface height and slope, assumed to be Gaussian

$$w(\zeta, \zeta') = \frac{1}{2\pi} (\psi_0 | \psi_0'')^{-\frac{1}{2}} \exp\left\{-\frac{\zeta^2}{2\psi_0} - \frac{\zeta \zeta'}{2|\psi_0''|}\right\} \quad (66)$$

where $\psi_0 = \sigma^2$ and ψ'' are the values at $\tau=0$ of the correlation function and its second derivatives, respectively.

For the region $0 < \theta < \frac{\pi}{2}$ where the probability of crossing one ray is assumed independent of that of crossing the other, R. Wagner found that the bistatic shadowing function

could be expressed as:

$$S(\theta_1, \theta_2) = \frac{\{1 - \exp[-2(B_1 + B_2)]\} x \{\operatorname{erf} v_1 + \operatorname{erf} v_2\}}{4(B_1 + B_2)} \quad (67)$$

where

$$B_i = \frac{\exp(-v_i^2) - \sqrt{\pi} v_i \operatorname{erfc} v_i}{4\pi v_i}; \quad i = 1, 2$$

$$v_i = \frac{\eta_i}{2\sigma^2 |\psi_0''|} = \frac{|\eta_i|}{2\Sigma^2}; \quad i = 1, 2$$

$$\begin{aligned} \text{as we from Eq. (60) have that } \sigma^2 |\psi''(0)| \\ = \langle \zeta'^2 \rangle = \Sigma^2 \end{aligned}$$

$$\eta_i = \cot \theta; \quad i = 1, 2$$

and noting that

$$\text{Error function } \operatorname{erf}(x) = \frac{2}{\sqrt{\pi}} \int_0^x e^{-t^2} dt$$

$$\text{Complementary error function } \operatorname{erfc}(x) = \frac{2}{\pi} \int_x^\infty e^{-t^2} dt$$

The shadowing function $S(\theta_1, \theta_2)$ is, in short, the fraction of the surface still illuminated. As seen from Eq. (60), the scattered field, in the high frequency case, is proportional to the illuminated area. Hence, the shadowing effect of a rough surface can be introduced by multiplying the ensonified area A by the shadowing function $S(\theta_1, \theta_2)$.

D. ESTIMATING THE SURFACE SCATTERING EFFECT

The following estimations are based on calculations in the specular direction, which is, as pointed out earlier, expected to give the maximum supplementary scattering effect. Hence, in the specular direction where $\theta_1 = \theta_2 = \theta$ and $\theta_3 = 0^\circ$, the scattering function S_{hf} reduces to the following expression:

$$S_{hf} = \frac{f^2(\theta) R^2}{2 (\cos\theta_1 + \cos\theta_2)^2 \langle \zeta^2 \rangle} e^{-\frac{k^2}{(2\gamma^2 \langle \zeta^2 \rangle)}} \quad (68)$$

$$S_{hf} = \frac{R^2}{8\pi \langle \zeta^2 \rangle}$$

as

$$f(\theta) = \cos\theta$$

$$\gamma = k \cos\theta$$

$$\alpha = 0$$

$$x = \frac{\alpha}{\cos\theta} = 0$$

As pointed out in the previous paragraph, the reflection of very high frequency signals by the sea surface yields scattered radiation that is incoherent under the assumption that

$$4\gamma^2 \sigma^2 \gg 1$$

$$(2\gamma^2 \langle \zeta^2 \rangle) \gg \frac{1}{R^2}$$

Before we launch into the calculations, we will verify these criteria for the frequency range of interest: 60 and 30 kHz.

Utilizing

$$\gamma^2 = k^2 \cos^2 \theta$$

$$\alpha = 8.1 \times 10^{-3}$$

$$\sigma^2 = \frac{\alpha W^4}{4\beta g^2}$$

$$\beta = 0.74$$

$$\langle \zeta^{12} \rangle = (3 + 5.12W) \times 10^{-3} \quad g = 9.81 \text{ m/s}^2$$

and assuming a windspeed of 10 m/s (SS3) yields

$$\alpha^2 = 0.30 \text{ m}^2 ; \sigma = 0.55 \text{ m}$$

$$\langle \zeta^{12} \rangle = 5.42 \times 10^{-2}$$

For 60 kHz ($\lambda = .025 \text{ m}$) and low grazing angles, e.g., $\theta = 85^\circ$

$$4\gamma^2\sigma^2 = 5.75 \times 10^2 \gg 1$$

$$(2\gamma^2\langle \zeta^{12} \rangle) = 5.2 \times 10^1 \gg \frac{1}{R^2}$$

and the first order $5.2 \gg \frac{1}{R^2}$, $R \geq 0.5 \text{ m}$.

Thus, for the 60 kHz case, the criteria are fulfilled.

For 30 kHz ($\lambda = .05 \text{ m}$) and $\theta = 85^\circ$.

$$4\sigma^2\gamma^2 = 1.44 \times 10^2 \gg 1$$

$$(2\gamma^2\langle \zeta^{12} \rangle) = 13 \gg \frac{1}{R}$$

again the first order $R > 1.0 \text{ m}$.

Thus, also for the 30 kHz case the criteria are fulfilled.

Similarly, for the shadowing function in the specular direction

$$0 < \theta_1 = \theta_2 = \theta < \pi/2 \quad \text{and} \quad \theta_3 = 0$$

we obtain the following simplified expression

$$S(\theta) = S(\theta_1, \theta_2) = \frac{[1 - \exp(-4B)] \operatorname{erfv}}{4B} \quad (69)$$

as

$$v_1 = v_2 = v = \frac{|\eta|}{(2\sigma^2 |\psi_0''|)^{\frac{1}{2}}} = \frac{|\eta|}{(2\Sigma^2)^{\frac{1}{2}}}$$

$$\eta_1 = \eta_2 = \eta = \cot\theta$$

$$B_1 = B_2 = B = \frac{[\exp(-v^2) - \sqrt{\pi} v \operatorname{erfc} v]}{4\sqrt{\pi} v}$$

In summary, for specular scattering at the high frequency limit, the expected average value of p^2 , where p is the pressure field at the receiver, is then obtained from the following simplified expressions:

$$\langle s^2 \rangle = \langle pp^* \rangle \frac{AS(\theta)}{R_2^2} S_{hf} \quad (70)$$

$$\langle s^2 \rangle = \langle pp^* \rangle \frac{AS(\theta)R^2}{8\pi R_2^2 \langle \zeta^{12} \rangle}$$

where

$$S(\theta) = \frac{1 - \exp(-4B) \operatorname{erfv}}{4B}$$

$$v = \frac{|\eta|}{(2\Sigma^2)^{\frac{1}{2}}}$$

$$|\eta| = \cot\theta$$

$$B = \frac{[\exp(-v^2) - \sqrt{\pi} v \operatorname{erfc} v]}{4(\pi)^{\frac{1}{2}} v}$$

$$\langle \zeta^{12} \rangle = \Sigma^2 = (3 + 5.12W) \times 10^{-3} ; W = \text{windspeed in m/s.}$$

$$R = \frac{\rho^1 c^1 \cos\theta - \rho c \cos\theta^1}{\rho^1 c^1 \cos\theta + \rho c \cos\theta^1} ; \frac{c}{\sin\theta} = \frac{c^1}{\sin\theta^1}$$

From Ref. 19 we use the following air/sea water interface data:

1. For air $c^1 = 343$ m/s and $\rho^1 c^1 = 415$ Rayls.
2. For sea water $c = 1500$ m/s and $\rho c = 1.54 \times 10^6$ Rayls.

The estimation of the illuminated area A for specular scattering where $\theta_1 = \theta_2 = 0$ and $\theta_3 = 0$, is based on the geometry illustrated in Fig. 24b. The illuminated area is given by

$$A = \pi ab \tag{71}$$

Assuming the following data to be known

h_s = depth of the source

h_r = depth of the receiver

$\Delta\phi$ = the half beam width of the directional receiver.

Both a and b of Eq. (71) can be calculated in terms of the detection range R_D as follows:

$$x_2 = \frac{R_D h_r}{h_s + h_r} \tag{72}$$

$$x_1 = R_D - x_2 = R_D \left(1 - \frac{h_r}{h_s + h_r}\right) ; \theta = \tan^{-1} \left(\frac{R_D}{h_s + h_r}\right)$$

$$R_1 = \frac{x_1}{\sin\theta}$$

$$R_2 = \frac{x_2}{\sin\theta}$$

To a good approximation when $\theta = \pi/2$, we have

$$a = x_1 = R_D \left(1 - \frac{h_r}{h_s + h_r}\right) \quad (73)$$

$$b = R \sin(\Delta\phi) = \frac{R_D h_r}{(h_s + h_r) \sin\theta} \sin(\Delta\phi)$$

The expression for $\langle s^2 \rangle$ is then introduced as a supplement to the direct path to the receiver in the following way:

By utilizing the relationship

$$I = \frac{\overline{p^2}}{\rho c} \quad (74)$$

for the intensity, the scattering intensity at the receiver and the intensity at the ensonified area are, respectively,

$$I_s = \frac{\overline{p^2}}{\rho c} = \frac{\langle s^2 \rangle}{c}$$

$$I_1 = \frac{\overline{p_1^2}}{\rho c} = \frac{\langle p_1 p_1^* \rangle}{\rho c}$$

Equation (70) can thus be written as

$$I_s = I_1 \frac{AS(\theta) R^2}{8\pi R_2^2 \langle \zeta^{12} \rangle}$$

$$I_s/I_1 = \frac{AS(\theta) R^2}{8\pi R_2^2 \langle \zeta^{12} \rangle}$$

$$10 \log I_s / I_1 = 10 \log \frac{I_s / I_{ref}}{I_1 / I_{ref}} = K_0$$

$$IL_s = IL(R_1) = K_0 \quad (75)$$

We then have to determine $IL(R_1)$

$$TL = SPL(1) - SPL(R_1) = 20 \log R_1 \quad (76)$$

$$SPL(R_1) = IL(R_1) = 10 \log I_1$$

$$SPL(1) = SL$$

yielding

$$IL(R_1) = SL - 20 \log R_1 = K_1 \quad (77)$$

Then

$$IL_{suppl} = K_0 + K_1 \quad (78)$$

is the supplement to the direct path, and

$$IL_{direct} = SL - 20 \log R_D = K_3$$

$$I_{direct} / I_{ref} = \text{anti log} \frac{IL_{direct}}{10} = K_4$$

$$I_{suppl} / I_{ref} = \text{anti log} \frac{IL_s}{10} = K_5$$

The total intensity of the receiver is thus

$$I_{Tot} / I_{ref} = \frac{I_{direct} + I_{suppl}}{I_{ref}} = K_4 + K_5 = K_6$$

$$IL_{Tot} = 10 \log K_6 = K_7 \quad (79)$$

Thus, the effect of the randomly rough surface compared to the idealized free-field condition can be expressed as

$$\Delta IL = IL_{\text{Tot}} - IL_{\text{direct}} = K_s \quad (80)$$

A calculator program on a Texas Instrument 59 (later called TI 59) was developed to perform these calculations. A block diagram of the program is outlined in Fig. (26) and the programs steps together with a detailed description is given in Appendix B. The calculations are based on the following fixed data

$$h_s = 2 \text{ m}$$

$$h_r = 6 \text{ m}$$

$$\Delta\phi = 10^\circ$$

$$W = 10 \text{ m/s (SS3)}$$

Then, varying the detection range from $R = 2000 \text{ m}$ to 100 m gives the difference between IL_{Tot} and IL_{direct} plotted in Fig. (27).

E. CONCLUSION AND DISCUSSION

As seen from Fig. (27) the supplementary effect of the scattering from a rough surface in the high frequency case is negligible compared to the direct path.

In saying so, it also should be pointed out that the Helmholtz-Kirchhoff's approach may be limited as it does not take into account the diffraction effects from crests

and troughs of the ensonified area, an effect which becomes increasingly important at low grazing angles, high frequency and when the rough surface is a superposition of swell and capillary waves.

VII. THE EFFECT OF SCATTERING AND ABSORPTION FROM THE SUB-SURFACE OCEAN LAYER

A. GENERAL SCATTERING THEORY

Generally when a region (volume) scatters sound, some of the energy carried by the incident wave is dispersed.

The energy lost by the incident wave may be absorbed by the scatterers or it may be simply deflected from its original course. The amount of energy lost per second by the incident wave divided by the incident wave's intensity is called the total cross section σ_e of the region and is the sum of the absorption and scattering cross sections

$$\sigma_e = \frac{\Pi_s + \Pi_a}{I_p}$$

where

Π_s = scattered power

Π_a = absorbed power

The existence of gas bubbles in the subsurface ocean layer modifies the forward scattering in the following two major ways:

1. The bubbles can resonate. When the bubbles are excited at a frequency near its natural frequency, it very efficiently absorbs and scatters the incident wave. At resonance, the scattering and

absorption cross section of a typical bubble at sea is of the order 10^3 times its geometrical cross section.

2. The bubbles change the effective compressibility of the water and cause the speed of sound to be a function of frequency, i.e., the medium is dispersive.

We will investigate and discuss these effects by separately estimating:

1. The attenuation due to the bubbles and
2. the refraction by bubbles.

B. ABSORPTION MODEL

The choice of model for the subsurface ocean layer depends on whether the medium has a tenuous or a dense distribution of scatterers. When the bubble density is tenuous, both "single scattering" and "first order multiple scattering" approximation solutions are applicable.

On the other extreme, when the bubble density is high, the so-called "diffusion" approximation can be used. Between these two extremes, multiple scattering effects are important.

The multiple scattering theory, which in the limit also contains the first order approximation, will be used to estimate effects of attenuation due to bubbles, on the propagation of propeller noise from the target to the torpedo.

The geometry of the propagation model is illustrated in Fig. (28) where it is assumed that a plane wave is incident on a semi-infinite (disregarding the sea surface) slab of thickness x containing a number of randomly distributed bubbles. The plane wave approximation is valid if the incident sound has a wavelength λ much greater than the bubble-radius a

$$ka \ll 1$$

where

$$k = \omega/c = 2\pi/\lambda$$

The receiver is located outside the slab and the beam pattern of the receiver is represented by the solid angle Ω_r .

We are interested in the estimating of the total power received, taking into account the multiple scattering process in the inhomogeneous slab as well as the beam pattern of the receiver.

The mathematical formulation of this problem is based on Twersky's theory of multiple scattering. Since the theory is presented in Ref. 20 only, the basic formulation, major assumptions, and the end results will be presented here.

The total intensity is the average of the square of the magnitude of the total field:

$$\langle |\psi^a|^2 \rangle = \langle |\langle \psi^a \rangle + \psi_f^a|^2 \rangle = |\langle \psi^a \rangle|^2 + \langle |\psi_f^a|^2 \rangle \quad (81)$$

where

$$\psi^a = \psi_i^a + \sum_{s=1}^N u_s^a$$

the scalar field at the receiver location \vec{r}_a , see Fig. (29), is the sum of the incident wave ϕ_i and the contribution from all N scatterers.

$|\langle \psi^a \rangle|^2$ is the coherent intensity based on the average field $\langle \psi^a \rangle$. $\langle |\psi_f^a|^2 \rangle$ is the incoherent intensity based on the fluctuating field ψ_f^a .

In Twersky's theory, the multiple scattering process is described by the following set of integral equations which Eq. (81) must satisfy:

$$\langle |\psi^a|^2 \rangle = |\langle \psi^a \rangle|^2 + |v_s^a|^2 \langle |\psi^s|^2 \rangle \rho(\vec{r}_s) d\vec{r}_s \quad (82)$$

where

$$v_s^a = U_s^a + U_t^a v_s^t \rho(\vec{r}_t) dt$$

is an operator representing all the scattering processes from s to a. (See Fig. (28).) It should be noted that Twersky's theory includes all the multiply scattered waves that involve chains of successive scattering going through different scatterers. (See Fig. (29a).) However, the theory neglects the terms which include an individual scatterer more than once, as illustrated by Fig. (29b).

Thus Twersky's theory is expected to give good results when back scattering is insignificant compared to the scattering in other directions.

As typical for most integral equations, Twersky being no exception, detailed complete solutions are difficult to obtain. However, Twersky gave an approximate solution to Eq. (81) and Eq. (82), which according to Ref. 20 have been found to agree reasonably well with experimental data. This solution is based on the following main assumptions:

- Backscattering is assumed to be small compared to scattering in other directions.
- Scattering is mostly concentrated in the forward direction. This is reasonable based on the assumed random distribution of the bubbles; i.e., no reinforcement of the radiation pattern occurs except in the direction of the incident wave.
- The angle θ_{as} is small, i.e., $\theta_{as} = 0^\circ$.

This leads to the following expression for the total intensity at the receiver:

$$\begin{aligned} \langle |\psi^a|^2 \rangle = T = & \exp(-\rho\sigma_a x) \exp(-\rho\sigma_s x) \\ & + q[1 - \exp(-\rho\sigma_s x)] \end{aligned} \quad (83)$$

where

σ_a = absorption cross section

σ_s = scattering cross section

$$q = \frac{\int_{\Omega_r} |f|^2 d\Omega_s}{4\pi \int |f|^2 d\Omega_s}$$

where

f = the amplitude function

q = the fraction of total scattered power collected by the receiver as illustrated in Fig. 30 and

ρ = is the bubble density, i.e., the number of scatterers per unit volume.

For small values of ρx we see from Eq. (82) that the coherent part dominates:

$$\ln T \approx -(\sigma_a + \sigma_s) \rho x \quad (84)$$

In this limit the multiple scattering result is equivalent to that obtained from single scattering considerations.

For large values of ρx which corresponds to very dense or very wide slab of scatterers, the incoherent intensity dominates

$$\ln T \approx \ln q - \sigma_a \rho x \quad (85)$$

In this latter case, it is notable that when $\Omega_r \geq 2\pi$, the receiver collects almost all the scattered power

$$\ln T \approx -\sigma_a \rho x \quad (86)$$

The first case, representing the situation for tenuous density of scatterers and/or narrow beam pattern of the receiver, gives a good approximation to the situation of interest in the thesis. It also represents the case for

which no scattered power is received. This will be approximately true for a narrow-beam width receiver. We will, therefore, investigate the coherent intensity first.

Also, the incoherent case, as represented by Eq. (86) will be investigated, where only losses due to absorption are incorporated.

C. THE COHERENT INTENSITY CASE

For the coherent case the intensity level after the incident wave has traversed a distance x is

$$I_x = I_p \exp[-(\sigma_a + \sigma_s) \rho x] \quad (87)$$

where

$$I_p = \text{incident plane wave intensity.}$$

The change in intensity over the distance x is

$$\begin{aligned} \Delta IL &= 10 \log \frac{I_x}{I_p} = \frac{I_p \exp [-(\sigma_a + \sigma_s) \rho x]}{I_p} \quad (88) \\ &= 10 \log \exp [-(\sigma_a + \sigma_s) \rho x] \end{aligned}$$

The excess attenuation per unit distance due to bubbles is thus

$$\begin{aligned} \alpha &= - \frac{\Delta IL}{x} = - \left[\frac{-(\sigma_a + \sigma_s) \rho x \log e}{x} \right] \\ &= (\sigma_a + \sigma_s) \rho \log e \\ \alpha &= 4.34 \sigma_e \rho, \text{ in dB/m.} \quad (89) \end{aligned}$$

However, this only takes into account bubbles of one size. In a bubbly medium there is a spectrum of radii.

The probability density function for finding a bubble size between radii a and $a+da$ is

$$W(a) = \frac{n(a)}{\rho} \quad (90)$$

where

$$\int_0^{\infty} W(a) da = 1$$

$n(a)da$ is the number of bubbles per unit volume having radii between a and $a+da$. It is common to use $da=1 \mu\text{m}$.

$\rho = \int_0^{\infty} n(a)da$ is the total number of bubbles per unit volume.

As the extinction cross section also is a function of the radius (See Eq. (93).), the absorption due to bubbles is obtained by integrating Eq. (89) over all possible radii

$$\alpha = 4.34 \int_0^{\infty} \sigma_e(a)n(a)da \quad (91)$$

To calculate the absorption coefficient, the extinction cross section σ_e must be derived from the general bubble dynamic relationship. This is done in detail by C. Clay and H. Medwin [Ref. 21] from which the following results are taken.

The scattering cross section

$$\sigma_s = \frac{\Pi_s}{I_p} \quad (92)$$

$$= \frac{4\pi a^2}{[(f_r/f)^2 - 1]^2 + \delta^2}$$

where

$$f_r = \text{resonance frequency} = \frac{1}{2\pi a} \left(\frac{2\gamma b \beta P_A}{\rho_A} \right)^{1/2}$$

$$f = f_o = \text{operating frequency}$$

$$\delta = \text{damping constant} = \delta_r + \delta_t + \delta_v$$

$$= ka + \left(\frac{d}{b} \right) \left(\frac{f_r}{f} \right)^2 + \frac{4\mu}{\rho_A \omega a^2}$$

$$a = \text{bubble radii}$$

$$\frac{d}{b} = 3(\gamma-1) \left[\frac{\bar{X}(\sin h \bar{X} + \sin \bar{X}) - 2(\cos h \bar{X} - \cos \bar{X})}{\bar{X}^2(\cos h \bar{X} - \cos \bar{X}) + 3(\gamma-1)(\sin h \bar{X} - \sin \bar{X})} \right]$$

$$\bar{X} = a \left(\frac{3\omega \rho_g C_{pg}}{k_g} \right)^{1/2}$$

$$k_g = \text{thermal conductivity of gas}$$

$$\rho_g = \text{density of gas} = \rho_{gA} \left[1 + \frac{2\tau}{(\rho_A a)} \right] (1+0.1z)$$

$$\rho_{gA} = \text{density of gas at sea level}$$

$$\tau = \text{surface tension}$$

$$P_A = 1.013 \times 10^6 (1+0.1z)$$

$$z = \text{bubble depth in m.}$$

$$C_{pg} = \text{specific heat of constant pressure of gas}$$

μ = shear viscosity of water

$\gamma = 7/5$, for diatomic gas

ρ_A = density for sea water

$$b = [1 + (\frac{d}{b})^2]^{-1} [1 + \frac{3\gamma-1}{\bar{X}} \frac{\sin h \bar{X} - \sin \bar{X}}{\cos h \bar{X} - \cos \bar{X}}]^{-1}$$

$$B = 1 + \frac{2\tau}{P_A a} (1 - \frac{1}{3\gamma b})$$

Furthermore:

$$\sigma_e = \sigma_a + \sigma_s = \frac{4\pi a^2 (\delta/ka)}{[(f_r/f)^2 - 1]^2 + \delta^2} \quad (93)$$

and

$$\sigma_a = \sigma_e - \sigma_s \quad (94)$$

A detailed computer program, as outlined in Appendix B, was developed for the TI 59 to handle the derivation of σ_s , σ_e , and σ_a based on an assumed receiver depth of $z = 6$ m.

For the 60 kHz case, both the extinction cross section σ_e and the absorption cross section σ_a are given in Fig. 31 as a function of bubble radius a .

Similarly, Fig. 32 gives σ_e and σ_a for the 30 kHz case. Superimposed on these figures are the curves for $n(a)da$ as calculated from the following: Figures 5 - 7 of Ref. 2 give the resonant bubble densities in a 1 μ m band as a function of depth and with the wind speed as parameter for the three discrete frequencies 12 kHz, 38 kHz and 120 kHz.

Based on these data, Fig. 33 shows the interpolated bubble density as a function of resonance frequency for sea state 2, 3, and 6.

Furthermore, both A. Lövik [Ref. 2] and H. Medwin [Ref. 3] found that the bubble density function $n(a)$ decreases with increasing bubble radii as

$$n(a) \propto a^{-x}$$

where H. Medwin [Ref. 3] found the power law of:

$$x = 4 \text{ for } a < 50\text{-}80 \text{ } \mu\text{m.}$$

$$x = 2 \text{ for } a > 50\text{-}80 \text{ } \mu\text{m.}$$

and A. Lövik [Ref. 2] found the power law of:

$$x = 4.2 \text{ between } 38 \text{ kHz and } 120 \text{ kHz}$$

$$x = 2.6 \text{ between } 12 \text{ kHz and } 38 \text{ kHz}$$

which, averaged over the depth interval, corresponds to the bubble radii of 380 μm (12 kHz), 120 μm (38 kHz) and 49 μm (120 kHz).

As suggested by A. Lövik [Ref. 2], the discrepancy between the two observations is not great and may be due to the few measuring frequencies used in the work of A. Lövik.

In summary, Fig. 33, from which we obtain the appropriate resonant bubble density in a 1 μm band $n(a_R)$ together with the power law $n(a) \propto a^{-x}$, comprise the full knowledge of $n(a)da$.

Performing a multiplication of σ_e and $n(a)da$, we obtain Fig. 34 and Fig. 35 for the 60 kHz and the 30 kHz case, respectively.

Finally, the integral

$$\int_0^{\infty} \sigma_e(a)n(a)da$$

was evaluated using a numerical integration based on Simpson's discrete approximation programmed for the TI 59 and documented in Appendix C.

Based on the above, the following absorption coefficient for the coherent case is obtained for $f = 60$ kHz

$$\begin{aligned} \alpha &= 4.34 \int_0^{\infty} \sigma_e(a)n(a)da = 4.34 (2.016 \times 10^{-1}) \\ &= 8.75 \times 10^{-1} \text{ dB/m.} \end{aligned}$$

$$\alpha \approx 0.88 \text{ dB/m} \quad (95)$$

with

$$n(a_R) = 1000$$

$$n(a) \propto a^{-4}$$

$$z = 6 \text{ m.}$$

Thus, it is seen that the attenuation due to bubbles is considerably greater than the "normal attenuation" due to chemical and viscous relaxation processes in sea water, which for the 60 kHz case is

$$\alpha = 0.02 \text{ dB/m.}$$

Thus, the total absorption coefficient for the 60 kHz case is

$$\alpha \approx 0.90 \text{ dB/m.} \quad (96)$$

For $f = 30 \text{ kHz}$, the absorption coefficient due to bubbles in the coherent case is

$$\begin{aligned} \alpha &= 4.34 \int_0^{\infty} \sigma_e(a) n(a) da = 4.34 (3.8375 \times 10^{-2}) \\ &= 1.665 \times 10^{-1} \text{ dB/m.} \\ \alpha &\approx 0.17 \text{ dB/m} \end{aligned} \quad (97)$$

with

$$\begin{aligned} n(a_R) &= 20 \\ n(a) &\propto a^{-2.6} \\ z &= 6 \text{ m.} \end{aligned}$$

For this case, the power law dependence of $n(a) \propto a^{-2}$ gives

$$\alpha \approx 1.655 \times 10^{-1}$$

Thus, the difference in power law dependence makes no significant difference in the absorption coefficient.

The absorption coefficient due to chemical and viscous relaxation processes is at 30 kHz

$$\alpha = 0.012 \text{ dB/m.}$$

The total absorption coefficient in the coherent case is

$$\alpha \approx 0.18 \text{ dB/m.} \quad (98)$$

D. THE INCOHERENT INTENSITY CASE

For the incoherent case, where only losses due to absorption are included, the product σ_a and $n(a)da$ for the 60 kHz and 30 kHz cases are given in Fig. 36 and Fig. 37, respectively. Performing a numerical integration based on the Simpson's discrete approximation leads to the following results:

For $f = 60$ kHz, the absorption coefficient due to bubbles is

$$\alpha = 4.34 \int_0^{\infty} \sigma_a(a)n(a)da = 4.34 (1.66 \times 10^{-1})$$
$$\alpha \approx 0.72 \text{ dB/m.} \quad (99)$$

with

$$n(a_R) = 1000$$
$$n(a) \propto a^{-4}$$
$$z = 6 \text{ m.}$$

Adding the "normal attenuation" in sea water for $f = \text{kHz}$, yields a total absorption coefficient of

$$\alpha \approx 0.74 \text{ dB/m} \quad (100)$$

For $f = 30$ kHz, the absorption coefficient due to bubbles is

$$\alpha = 4.34 \int_0^{\infty} \sigma_a(a)n(a)da = 4.34 (2.975 \times 10^{-2}) \quad (101)$$
$$\alpha \approx 0.13 \text{ dB/m}$$

with

$$n(a_R) = 20$$

$$n(a) \propto a^{-2}$$

$$z = 6 \text{ m.}$$

Adding the "normal attenuation" in sea water for $f = 30 \text{ kHz}$ yields a total absorption coefficient in the incoherent case of

$$\alpha \approx 0.14 \text{ dB/m} \quad (102)$$

E. SUMMARY AND DISCUSSION OF THE BUBBLE ATTENUATION

As seen from the above, the attenuation due to bubbles in the subsurface ocean layer is important for high frequency and high Sea State.

Accounting for the effect of bubbles at Sea State 3 in summary we found the following absorption coefficients in dB/m:

f = 60 kHz		f = 30 kHz	
coherent	incoherent	coherent	incoherent
$\alpha = 0.88$	$\alpha = 0.72$	$\alpha = 0.17$	$\alpha = 0.13$

The main assumptions were:

- the back scattering is small compared to that in other directions.
- the scattering is mostly concentrated in the forward direction.

- the angle θ_{as} between the scatterer and the receiver is small, i.e., $\theta_{as} \approx 0^\circ$.
- the depth of the receiver is $z = 6$ m.
- the sea state is 3.

The range dependent portion of the passive sonar Eq. (1) $TL = -20 \log R - \alpha R$ for both the 60 kHz and 30 kHz scattering results can now be compared with the reference data obtained in Section V.

For $f = 60$ kHz, Fig. 22 gives $TL = -20 \log R - \alpha R$ as a function of R with

1. $\alpha = 0.021$ dB/m, the "normal attenuation" due to chemical and viscous relaxation processes.
2. $\alpha = 0.9$ dB/m, the total attenuation including the effect of bubbles in the coherent case.
3. $\alpha = 0.74$ dB/m, the total attenuation including the effect of bubbles in the incoherent case.

For the same example as in the reference model, Fig. 22 yields the detection ranges for 60 kHz.

$$R = 1200 \text{ m for } \alpha = 0.021 \text{ dB/m} \quad (103)$$

$$R = 60 \text{ m for } \alpha = 0.90 \text{ dB/m}$$

$$R = 70 \text{ m for } \alpha = 0.74 \text{ dB/m}$$

Not surprisingly, this result seems to exclude the possibility of having both a searching and attack depth near the surface, i.e., $z = 6$ m, for a torpedo system operating in a high frequency region, $f = 60$ kHz.

Similarly, for $f = 30$ kHz, Fig. 23 gives $TL = -20 \log R - \alpha R$ as a function of R with

1. $\alpha = 0.012$ dB/m, the "normal attenuation" in sea water.
2. $\alpha = 0.18$ dB/m, the total attenuation including the effect of bubbles in the coherent case.
3. $\alpha = 0.14$ dB/m, the total attenuation including the effect of bubbles in the incoherent case.

For the same detection example as in the reference model, Fig. 23 yields the detection ranges for 30 kHz:

$$R = 2400 \text{ m for } \alpha = 0.012 \text{ dB/m} \quad (104)$$

$$R = 250 \text{ m for } \alpha = 0.18 \text{ dB/m}$$

$$R = 310 \text{ m for } \alpha = 0.14 \text{ dB/m.}$$

Again, the bubbles give a major decrease in the detection range. A detection range of $R = 250$ m seems marginally acceptable as the turn rate requirement for a pursuit homing trajectory may become excessive.

The above results are summarized in Tables III and IV for the 60 kHz and 30 kHz, respectively.

F. THE REFRACTION BY BUBBLES

The presence of bubbles in the sea water affects the speed of sound (phase speed) primarily because of the change in compressibility. The derivation of this dispersive relationship on the sound speed has been done by H. Medwin

TABLE III

DETECTION PARAMETERS AND RANGES FOR $f=60$ kHz

SL	DI	NL	P_D	P_{FA}	DT	Detection Range (m)		SS	f
dB	dB	dB			dB	$\alpha=.021$	$\alpha=.9$	$\alpha=.74$	kHz
100	-180	-124	.5	10^{-6}	-6.5	1200	60	70	3 60
100	-180	-124	.5	10^{-99}	0	1000	--	--	3 60

TABLE IV

DETECTION PARAMETERS AND RANGES FOR $f=30$ kHz

SL	DI	NL	P_D	P_{FA}	DT	Detection Range (m)	SS	f
dB	dB	dB			dB	$\alpha=.012$ $\alpha=.18$ $\alpha=.14$		kHz
106	-180	-124	.5	10^{-6}	-6.5	2400 250 310	3	30
106	-180	-124	.5	10^{-99}	0	2200 220 290	3	30

[Ref. 22]. H. Medwin showed that the bubbles with resonant frequencies greater than the incident frequency decrease the sound speed, while bubbles with resonant frequency lower than the incident wave increase the sound speed.

Furthermore, H. Medwin [Ref. 22] predicts the sound speed gradient due to bubbles as a function of depth for a frequency range and wind speed compatible with our domain of interest.

He found the gradients

$$g = \partial c / \partial z = 0.26 \text{ s}^{-1} \text{ at } z = 0 \text{ m.}$$

$$g = \partial c / \partial z = 0.016 \text{ s}^{-1} \text{ at } z = 10 \text{ m.}$$

$$g = \partial c / \partial z = 0.005 \text{ s}^{-1} \text{ at } z = 20 \text{ m.}$$

For comparison, the sound speed gradient due to pressure in an isothermal water is

$$g = 0.017 \text{ s}^{-1}$$

This shows that the rays in the top 10 m are strongly influenced by bubbles. However, with respect to our surface scattering model (Section VI) where both the source and the receiver are situated very close to the surface and where relatively short propagation distances are encountered, this refraction phenomenon is assumed to have negligible effect.

VIII. THE TURN RATE LIMITATION

As pointed out in the previous section, the presence of bubbles near the surface may significantly reduce the range at which the target can be detected.

In this section, the turn rate necessary during pursuit homing at the previous estimated detection ranges will be studied. A computational procedure will be used to determine the range of angles on the bow (AOB) of the target at the beginning of homing which lead to miss on the initial attack. A trajectory where the torpedo velocity vector always is directed towards the instantaneous target position is called a pursuit homing trajectory. The derivation of the pursuit homing trajectory follows P. van Nostrand [Ref. 23] and is based on the geometry of Fig. 38, where

r = approach angle, i.e., angle between ship velocity vector and the line of sight.

$$\text{AOB} = 180 - \phi$$

The equation of motion is obtained by taking the component along r and the normal to r , yielding

$$\dot{r} = V_S \cos \phi - V_T \quad (105)$$

$$r\dot{\phi} = -V_S \sin \phi \quad (106)$$

where

\dot{r} = range rate

$\dot{\phi}$ = turn rate

V_S = target speed

V_T = torpedo speed.

Dividing Eq. (105) by Eq. (106) yields:

$$\frac{\dot{r}}{r} = \left(\frac{V_T}{V_S} \frac{1}{\sin \phi} - \cot \phi \right) \dot{\phi} ; r \neq 0$$

and defining

$$\frac{V_T}{V_S} \triangleq P$$

yields

$$\frac{\dot{r}}{r} = \left(\frac{P}{\sin \phi} - \cot \phi \right) \dot{\phi} \quad (107)$$

$$r = K \frac{(\sin \phi)^{P-1}}{(1 + \cos \phi)^P} \quad (108)$$

Then, introducing the initial conditions: r_0, ϕ_0 where

r_0 : initial detection range

ϕ_0 : initial approaching angle

yields

$$K = r_0 \frac{(1 + \cos \phi_0)^P}{(\sin \phi_0)^{P-1}} \quad (109)$$

For the geometry of Fig. 38, the turning rate is given by Eq. (105).

$$\dot{\phi} = -\frac{V_S}{r} \sin \phi \quad (110)$$

Substituting Eq. (108) into Eq. (110) yields:

$$\dot{\phi} = -\frac{V_S (1+\cos \phi)^P}{K(\sin \phi)^{P-2}} \quad (111)$$

From Eq. (108) we see that $r \rightarrow 0$ as $\phi \rightarrow 0$, i.e., ϕ tends to zero as the torpedo approaches the target ship. It is further of interest to determine the limiting value of the turning rate as the torpedo approaches the target for various values of the parameter p . This is done by taking the derivative of $\dot{\phi}$ with respect to ϕ . Thus, from Eq. (109) we get

$$\frac{d\dot{\phi}}{d\phi} = -\frac{V_S}{K} (\sin \phi)^{1-P} [1+\cos \phi]^P [2 \cos \phi - p] \quad (112)$$

For $1 < p < 2$, we see that Eq. (112) is zero at

$$\cos \phi = p/2 \quad (113)$$

$$\phi = \cos^{-1}(p/2)$$

with an associated maxima

$$|\dot{\phi}_{\max}| = \frac{V_S (1+p/2)^P [1-(p/2)^2]^{1-P/2}}{K} \quad (114)$$

Furthermore, the turn rate for $p < 2$ at impact is zero as the limit of Eq. (109) yields:

$$\lim_{\phi \rightarrow 0} \dot{\phi} = -\frac{V_S}{K} \lim_{\phi \rightarrow 0} (\sin \phi)^{2-P} [1+\cos \phi]^P \rightarrow 0 \quad (115)$$

For $p=2$ we see from Eq. (111) that

$$\lim_{\phi \rightarrow 0} \dot{\phi} = -\frac{V_S}{K} \lim_{\phi \rightarrow 0} (1 + \cos \phi)^2 = -\frac{4V_S}{K} \quad (116)$$

For $p>2$ we see from Eq. (111) that there is no zero value of $d\dot{\phi}/d\phi$ between $\phi = 0^\circ$ and $\phi = 180^\circ$, since all terms of Eq. (112) are nonzero terms for $0^\circ < \phi < 180^\circ$. Furthermore, the turn rate for $p>2$ at impact is

$$|\lim_{\phi \rightarrow 0} \dot{\phi}| = \left| -\frac{V_T}{K} \lim_{\phi \rightarrow 0} \frac{(1 + \cos \phi)^P}{(\sin \phi)^{P-2}} \right| \rightarrow \infty \quad (117)$$

as $(\sin \phi) \rightarrow 0$ since $(p-2) > 0$.

Furthermore, as $\phi \rightarrow 180^\circ$, we get from Eq. (112)

$$\lim_{\phi \rightarrow 180} \frac{d\dot{\phi}}{d\phi} = \frac{V_O}{K} (2+p) \lim_{\phi \rightarrow 180} (\sin \phi)^{1-P} (1 + \cos \phi)^P$$

Evaluating

$$\lim_{\phi \rightarrow 180} (\sin \phi)^{1-P} (1 + \cos \phi)^P = \lim_{\phi \rightarrow 180} (\sin \phi) \left(\frac{1 + \cos \phi}{\sin \phi} \right)^P$$

by applying l' Hopitale rule to the term

$$\lim_{\phi \rightarrow 180} \frac{1 + \cos \phi}{\sin \phi} = \lim_{\phi \rightarrow 180} \frac{-\sin \phi}{\cos \phi} \rightarrow 0$$

Thus, the product $\sin \phi \left(\frac{1 + \cos \phi}{\sin \phi} \right)^P$ approaches zero for any $p>1$, since both terms in this product approach zero as $\phi \rightarrow 180$.

Figure 39 shows a plot of computed values of $|\dot{\phi}K/V_s|$ for different values of $p > 1$. From this we can draw the following summarizing conclusions.

For $1 < p < 2$ the turn rate has

- a maximum value at $\phi = \cos^{-1}(p/2)$
- the zero value at $\phi = 0^\circ$ and $\phi = 180^\circ$.

For $p = 2$ the turn rate

- is zero at $\phi = 180^\circ$.
- monotonically increasing with decreasing ϕ approaching the value $(4V_s/K)$ when $\phi = 0^\circ$.

For $p > 2$ the turn rate

- is zero at $\phi = 180^\circ$.
- is monotonically increasing with decreasing ϕ approaching ∞ as $\phi = 0^\circ$.

As seen from the above for $p > 2$, the turn rate increases monotonically with decreasing ϕ approaching an infinite turn rate to hit a point target. To avoid this singularly we must make some provision. If the torpedo's maximum turn rate is exceeded only at some very small range, a hit is likely.

Figure 40 illustrates the hit criterion used. Assume a rudder of length L_R is situated directly behind the propeller which is idealized as an acoustic point source.

If the torpedo becomes turn rate limited at some range $r = r'$, it at best can proceed along a circular path which lags the desired pursuit trajectory, or at worst it can

loose acoustic contact and go into "hold-in," maintaining a constant heading at the angle ϕ' . In this last case, it will cross the line of target ship's course in the time:

$$t = r'/V_r \quad (118)$$

If this advance is less than the length of the rudder L_R , the torpedo will impact the rudder. Hence, the limiting condition is

$$\frac{r'}{p} = L_R$$

$$r' = pL_R \quad (119)$$

For this analysis, we have arbitrarily chosen

$$L_R = 3 \text{ m} \quad (120)$$

Thus, the torpedo's turn rate has not been exceeded when the range to the target is

$$r' = pL_R = 3 p \quad (121)$$

and a hit is assumed.

Now we can analyze the cases $p > 2$ and $1 < p < 2$ on the same footing. If we match the torpedo's maximum turn rate to a particular range r' , it is certain that its turn rate has not been exceeded earlier in the run.

This turn rate-range matching is done by substituting the "hit-range" defined as $r' = 3 p$ into Eq. (106) and solving it for $\sin \phi$, yielding

$$\dot{\phi}_{\max} = -\frac{V_s}{3p} \sin \phi$$

$$\sin \phi = -\frac{\dot{\phi}_{\max} (3p)}{V_s}$$

Since $\dot{\phi}$ is always negative, $\sin \phi$ is always positive and equal to

$$\sin \phi = \frac{3p |\dot{\phi}|_{\max}}{V_s} \quad (122)$$

Two values of ϕ satisfies this equation, and they are denoted

$$\phi_A = \sin^{-1} \frac{3p |\dot{\phi}|_{\max}}{V_s}; \text{ for } \phi \leq 90^\circ \quad (123)$$

$$\phi_B = 180^\circ - \phi_A$$

A unique value of K may now be found using Eq. (111) for each of the angles ϕ_A and ϕ_B .

$$K = \frac{V_s (1 + \cos \phi)^P}{|\dot{\phi}|_{\max} (\sin \phi)^{P-2}}$$

These values of K are designated as K_A and K_B , and for each there is a corresponding value of ϕ_0 from Eq. (109) with ϕ_0 given by the initial detection range

$$(\phi_0)_A \text{ and } (\phi_0)_B$$

In the case of $1 < p < 2$, the turn rate does not necessarily increase monotonically during the pursuit homing trajectory, and we must check that either ϕ_A or ϕ_B , respectively, is not beyond the angle corresponding to $\dot{\phi}_{\max}$.

As seen from Eq. (113), the turn rate reaches a maximum at an angle given by

$$\phi^* = \cos^{-1}(P/2)$$

with a corresponding turn rate given by

$$|\dot{\phi}|_{\max} = \frac{V_s (1+P/2)^P [1-(P/2)^2]^{1-P/2}}{K}$$

Thus, the value of $K = K^*$ for which the limiting turn rate is achieved

$$K = \frac{V_s (1+P/2)^P [1-(P/2)^2]^{1-P/2}}{|\dot{\phi}|_{\max}}$$

It is important to note that, if $\phi_A < \phi^* < (\phi_O)_A$, the "A" trajectory is invalid since the maximum turn rate of the torpedo, reached at the range $r = 3p$ at $\phi = \phi_A$ is exceeded earlier in the trajectory. In that case, the limiting trajectory is the "*" trajectory. Along the same lines, we argue that the "B" trajectory always is a limiting trajectory, since the equality $\phi_B < \phi^* < (\phi_O)_B$ cannot be satisfied. This follows from the fact that

$$0^\circ < \phi^* < 90^\circ$$

and $\phi_B = 90^\circ$ as ϕ_B is the supplement of ϕ_A .

Below some critical ship speed, the torpedo will not be turn rate limited. This speed is obtained when the trajectory is normal to the ship's velocity vector, $\phi = 90^\circ$, at a range of $r = 3p$.

Thus, from Eq. (106), we obtain

$$(3p) |\dot{\phi}|_{\max} = (V_s)_{NL} \sin 90^\circ$$

yielding

$$(V_s)_{NL} = (3p) |\dot{\phi}|_{\max} \quad (124)$$

Then introducing $p = V_T / (V_s)_{NL}$, we get

$$(V_s)_{NL} = [3V_T |\dot{\phi}|_{\max}]^{1/2} \quad (125)$$

Furthermore, we see from Eq. (108) that for $\phi = 90^\circ$

$$(K)_{NL} = 3p \quad (126)$$

Again, by probing Eq. (88) we can obtain the corresponding values of ϕ_o , designated $(\phi_o)_{NL}$, where the subscript "NL" is used to indicate the "no-limit" boundary point.

The computational procedure is based on:

1. Assuming a torpedo speed $V = 35$ kts.
2. Using an initial detection range (beginning of homing) $r_o = 250$ m.
3. Assuming the following maximum turn rates:
 - a. 8 o/s b. 12 o/s c. 16 o/s
 - d. 24 o/s e. 36 o/s f. 48 o/s
4. The following range of target speeds
$$0 < V_s < 25 \text{ kts}$$

The aim of the computation is to determine whether the limiting ϕ_o , and hence AOB, is governed by ϕ^* or by the turn rate at the range $r = 3p$.

The calculations are divided into two parts, and are performed on a TI 59 calculator.

For a given ship speed, Part I gives the sequential calculations of ϕ_A , K_A , ϕ_B , K_B , θ^* and K^* for each of the turn rates. The computer program is given in Appendix E.

Then, in Part II, the probe calculation for $(\phi_O)_A$, $(\phi_O)_B$, $(\phi_O)^* = (\phi_O)_{A,B,*}$ are performed. The program is given in Appendix E.

The limiting results are given on a polar plot, Fig. 41 with

$$(\text{AOB})_{A,B,*} = 180^\circ - (\phi_O)_{A,B,*}$$

As seen from Fig. 41, for a target speed of 15 kts, we need $\text{AOB} > 85^\circ$ at ϕ_O for a maximum turn rate 16 o/s in order to have a hit at the first attack.

IX. CONCLUSIONS AND RECOMMENDATIONS

The detection performance of a passive homing torpedo used against shallow-draft surface ships operating in moderate sea states was investigated. Attention was focused on the effects of scattering from the randomly rough sea surface and scattering and absorption from the bubble-dominated inhomogeneous layer just below the sea surface. The effects of these two scattering mechanisms were separately estimated and their relative importance were compared.

The passive sonar equation was used to predict the performance of the homing system, and the detection range considering these two scattering effects was obtained and compared to the detection range based on a reference model. An idealized propagation model was used as reference of comparison. This reference model was based on a noise source model for a cavitating propeller, the operational characteristics for a square-law detector, and a transmission model associated with a homogeneous, unbounded medium.

Due to high frequency, moderate sea state and low grazing angles, the scattering from the randomly rough sea surface was found to be dominated by the direct path.

This result includes effects from geometrical shadowing.

The effect of scattering and absorption from the bubble-dominated, inhomogeneous subsurface layer was investigated using multiple scattering theory. Both the coherent and incoherent limits were investigated by incorporating the associated absorption coefficient into the transmission equation.

The effect on the sound speed from the bubble content was found to be negligible.

At the assumed depth setting of 6 m for the torpedo's search and attack phase, the scattering from the bubbles increased the transmission loss. This increase depended on the frequency and the wind speed.

Two operating frequencies were investigated, 60 kHz and 30 kHz. For both cases, bubbles significantly decreased the detection range.

For a torpedo system operating at the high frequencies, e.g., 60 kHz, the result indicates the inadvisability of using a searching and attack depth near the surface, i.e., $z = 6$ m.

For an operating frequency around 30 kHz, the calculated detection ranges is such that the turn rate requirements for a pursuit homing trajectory become excessive. For a maximum turn rate of 16 o/s, this limitation can be avoided

by adapting a tactical procedure where the angle on bow (AOB) at the beginning of the torpedo attack is greater than 85° .

At sea state 3, the results show a consistent and general trend towards the need for lower operating frequency in order to increase the detection range. An operating frequency below 30 kHz seems indicated.

Furthermore, a search depth below the bubble-dominated subsurface layer, i.e., $z > 15-20$ m would result in an increased detection range.

To reduce the operational limitations induced by the scattering and absorption effects, a high maximum turn rate together with a variable speed capability, where $p \leq 2$ would be beneficial.

The result of this analysis has clearly demonstrated the importance of environmental factors on the torpedo capability, and is useful in giving insight into the behavior of a homing torpedo during its critical attack phase.

A valuable follow-on of this study would be an investigation of the effects of the bubble-dominated subsurface layer on target validation and pitch plane steering when the torpedo search depth is 50-60 m.

APPENDIX A

DETAILED OCEANOGRAPHIC BACKGROUND MATERIAL

A. GEOGRAPHIC DESCRIPTION

The Norwegian coastal waters constitute the eastern boundary of the Norwegian Sea. Although some general aspects related to the Norwegian Sea will be covered, this analysis will be concentrated on the Norwegian coastal waters above 68°N.

B. WIND

The northern region of the Norwegian Sea is affected by the Polar Easterlies and the southern region by the prevailing Westerlies. There are two dominant air masses which are relatively permanent:

- The Greenland high.

- The Iceland low.

These pressure systems produce storms which are carried across the Norwegian Sea in a belt from Iceland towards the Norwegian Coast causing steady precipitation and wind most of the year. The steep Norwegian Coast has a considerable influence on the winds and consequently also on the waves in the coastal waters. The main general modifications are that the streamlines tend to run parallel

to the coast and that wind and sea increases with distance from the sheltered coast into open ocean.

Strong local variation may occur. The most important of these are the marked local increase in wind speed in areas where the coast sharply changes direction. One such "corner effect," caused by the confluence of the streamlines, occurs near "Nordkapp" (North Cape). Also of importance are monsoonal effects due to the different heat capacities between the ocean and the continent. Drainage of cold air from the inland valleys in the wintertime causes a marked increase in the wind speed in several areas along the coast. Most of these coastal effects are significantly dissipated at distances of approximately 50 nmi. from the coast. The fact that the wind tends to blow along the coast is clearly demonstrated in Figs. 12 and 13 which include data from weather stations from "Hillesöy" to "Ona" and "Myken" to "Furuholmen" respectively. The high frequency of offshore winds is caused by the drainage of cold air from the inland valleys during winter time. That this phenomenon is closely connected to the coast is illustrated by the fact that it is missing at weather station "Skomvaer" situated approximately 50 nmi. off the main coast. A frequency distribution of observed wind speeds along the coast, obtained from Ref. 1, is presented in Table V. A summary of this table follows:

TABLE V

FREQUENCY DISTRIBUTION OF WIND SPEED IN PERCENT PER YEAR
AT WEATHER STATIONS ALONG THE NORWEGIAN COAST

m/sec	0-7	8-13	14-20	≥ 21
Beaufort	0-4	5+6	7+8	≥ 9
Ferder	67	28	5	0.1
Lyngor	79	19	2	0.2
Lista	67	28	5	0.2
Utsira	73	22	5	0.3
Hellisöy	77	19	4	0.2
Krakenes	58	28	11	2.7 Jan-Dec
Ona	70	22	7	0.7 1949-1975
Sula	61	30	8	1.1
Nordoyan	49	35	14	1.9
Myken	64	26	9	1.2
Skomvær	58	31	10	0.9
Andenes	79	18	3	0.1
Torsvar	72	23	5	0.4
Fruholmen	54	32	12	1.8
Vardo	75	22	3	0.1
Biornoya	63	31	6	0.4 1956-1975
Polarfront	46	30	14	1.4

The highest winds are reported from the areas between 62°N and 68°N . The frequency of high winds in this area are significantly greater than those found at stations to the south of 62°N and also to the north of 68°N . The wind condition around North Cape, are very severe. This area can be compared with the other coastal area of high wind speed such as "Stadt" (represented by the weather station, "Krakenes"). In these areas the frequency of storms is greater than at "Polarfront" situated in the open Norwegian Sea.

C. WAVES

Frequency distribution of significant wave heights are represented in Table VI.

The station north of 68°N is characterized by comparatively small frequency of high waves. Even at "Furuholmen" where wind conditions are very severe, the frequency distribution of significant wave heights is similar to more sheltered areas like "Utsira."

The seasonal variation for the area of interest around 70°N is given in Figs. 3 and 4. The average monthly distribution of significant wave heights for a typical station like "Andenes" is given in Fig. 3 and Fig. 4 gives the yearly distribution for this station.

TABLE VI

FREQUENCY DISTRIBUTION OF SIGNIFICANT WAVE
HEIGHT IN PERCENT AT THE WEATHER STATION "ANDENES"

STATION: Andenes

YEARS: 1949-1972

SS	0+1+2	3	4	5	6	7	8	9	
H_S	0 - 0.4	0.5 - 1.2	1.3 - 2.4	2.5 - 3.9	4.0 - 5.9	6.0 - 8.9	9.0 - 13.9		N
JAN	15.3	26.9	33.3	15.5	6.6	2.3	0.18	0.00	2542
FEB	17.7	28.7	31.3	14.2	5.9	2.0	0.14	0.00	2295
MAR	18.1	28.9	30.8	14.3	5.8	1.9	0.17	0.00	2529
APR	24.5	33.1	27.4	10.8	3.4	0.8	0.04		2293
MAY	30.9	35.5	23.9	7.7	1.7	0.3	0.01		1720
JUN	37.4	36.9	20.2	4.8	0.6	0.1	0.00		1565
JUL	42.6	36.2	17.1	3.7	0.4	0.0	0.00		1618
AUG	40.6	36.4	18.0	4.3	0.5	0.1			1621
SEP	29.7	34.3	24.4	8.9	2.1	0.5	0.01		2301
OCT	21.8	31.3	29.4	12.4	4.1	1.0	0.01		2374
NOV	21.7	31.5	29.9	11.7	4.1	1.1	0.06		2303
DEC	18.5	30.1	32.2	13.2	4.7	1.2	0.09		2379
YEAR	26.6	32.5	26.5	10.1	3.3	0.9	0.06	0.00	

N = Number of Observations
SS = Class Interval, State of Sea
 H_S = Significant Wave Height

D. AMBIENT NOISE

Due to the fact that the Norwegian Sea is physically separated from the Atlantic by the Faeröy-Shetland-Iceland ridge, and from the Greenland Sea by the Jan Mayan ridge, little long distance shipping noise is transferred into the area. This, combined with relatively low shipping traffic in the central and northern parts of the Norwegian Sea, produces a relatively low ambient noise level for the frequency band $100 < f < 1000$ Hz, especially when noise from marine life is not included. Further, in the absence of nearby shipping and marine life, the ambient noise level in the frequency band $1 < f < 50$ kHz is, according to Ref. 4, dominated by the wind.

A typical area for the central part of the Norwegian Sea can be represented by the weather station "Polarfront" at 66°N , 2°E . Reference 1 shows that there is approximately a 15% chance of finding wind forces of Beaufort > 6 . These effects predict a moderate ambient noise level in the frequency range 100 Hz-50 kHz for the central and northern regions of the Norwegian Sea.

The shallow coastal Norwegian waters are, according to Ref. 4, typically 5-10 dB noisier than the corresponding deep waters. However, great variability caused by local traffic, fishing fleet activity, marine life, and local wind conditions makes ambient noise level prediction

difficult in these areas. This means that accurate ambient noise level determinations have to be made on the spot, as it is both site and time dependent.

A noticeable influence on the ambient noise level is rain, which is a year around feature along the Norwegian coast. As seen from Fig. 8, taken from Ref. 4, rain has a tendency to produce a constant high ambient noise level over a large frequency range, thus dominating other effects. Furthermore, for the upper frequency of interest, i.e., around 60 kHz the lower bound for the ambient noise is determined by the thermal agitation, see Fig. 8.

In determining the figure of merit (FOM) for a passive sonar system, the noise level will be the larger of either the self noise or the ambient noise. For a torpedo the self noise will typically be dominant.

E. SOUND SPEED PROFILES

Again, concentrate on data relevant to Norwegian coastal waters. According to Ref. 6, which covers the southern part of the Norwegian coast, low sound speeds are common because of the influence of water from the Baltic Sea combined with fresh water drainage from the fjords. Furthermore, great variability, both seasonal and within seasons, is encountered. Figure 9 obtained from Ref. 5 gives a picture of the sound speed profiles

for the northern Norwegian coast. Again, large variations are common. Noticeable in both sets of data is a typical seasonal pattern of strong cooling of the surface layer during winter and a similarly strong heating during summer. Furthermore, note that the minimum and maximum are relatively shallow, i.e., less than 50 m.

Also characteristic is the influence of the cold and fresh melt waters drained out through the fjord-arms during spring and summer.

To illustrate the sonar problems associated with these sound speed profiles, ray paths for the extremes of Fig. 9 are shown in Figs. 10 and 11, where the source is 3 m below the sea surface.

APPENDIX B
SURFACE SCATTERING TI 59 PROGRAM

A. INTRODUCTION

This program gives specular scattered power at the receiver versus incoming power at the randomly rough surface in the high frequency limit according to Eq. (70).

Shadowing of surface areas by other parts of the boundary are taken into account by the bistatic shadowing function $S(\theta)$.

Furthermore, the program gives the effect of the randomly rough surface compared to the idealized free-field condition as expressed in Eq. (80). The results of these calculations is given in Fig. 27.

B. PROGRAM STEPS

A block-diagram of the computer program is given in Fig. 26.

The program uses the partitioning ratio of program to data space according to code 4 OP17. The users instructions are as follows:

Procedure	Enter	Press	Display
Enter data	Detection range	2nd A	R_D^1
Enter data	Source depth	R/S	h_s^1
Enter data	Receiver depth	R/S	h_r^1
Enter data	Beam width	R/S	ϕ^1
Enter data	Wind speed	R/S	w^1
Calculate θ, R_1, R_2, A	--	2nd B	A $(\theta, R_1, R_2, A)^1$
Calculate $\langle \zeta^{12} \rangle$	--	2nd C	$\langle \zeta^{12} \rangle^1$
Calculate v	--	2nd D	v^1
Calculate erfc v	--	A	erfc v^1
Calculate S(θ)	--	B	$S(\theta)^1$
Calculate $\frac{\langle s^2 \rangle}{\langle p_1 p_1^* \rangle}$	--	C	$\frac{\langle s^2 \rangle^1}{\langle p_1 p_1^* \rangle^1}$
Calculate ΔIL	--	D	ΔIL^1

¹These values are printed automatically if the calculator is connected to the PC-100A Print Cradle.

For the error function complement we have

$$\text{erfc}(v) = \frac{2}{\sqrt{\pi}} \int_v^{\infty} e^{-\alpha^2} d\alpha$$

in contrast to the normal distribution

$$Q(u) = \frac{1}{\sqrt{2\pi}} \int_u^{\infty} e^{-t^2/2} dt$$

However, there is a linear relationship between the two functions.

The numerical equation used to calculate the $\text{erfc}(v)$ is a modified program from Texas Instruments [Ref. 24].

$$\text{erfc}(v) = Z(v) [b_1\alpha + b_2\alpha^2 + b_3\alpha^3 + b_4\alpha^4 + b_5\alpha^5]$$

where

$$\alpha = \frac{1}{1+\rho v}$$

$$p = .231649$$

$$b_1 = .451673691$$

$$b_2 = -.504257336$$

$$b_3 = 2.51939026$$

$$b_4 = -2.563346623$$

$$b_5 = 1.881292139$$

The program steps are listed below, giving location (LOC), code (COD), key symbol (KEY), and comments.

000	76	LBL	023	17	B'	046	05	05
001	16	A'	024	53	(047	55	÷
002	42	ST	025	53	(048	43	RCL
003	00	00	026	43	RCL	049	02	02
004	99	PRT	027	00	00	050	54)
005	91	R/S	028	65	x	051	22	INV
006	42	STO	029	43	RCL	052	30	TAN
007	01	01	030	02	02	053	54)
008	99	PRT	031	54)	054	42	STO
009	91	R/S	032	55	+	055	06	06
010	42	STO	033	53	(056	99	PRT
011	02	02	034	43	RCL	057	53	(
012	99	PRT	035	01	01	058	53	(
013	91	R/S	036	85	+	059	43	RCL
014	42	STO	037	43	RCL	060	05	05
015	03	03	038	02	02	061	55	÷
016	99	PRT	039	54)	062	53	(
017	91	R/S	040	54)	063	43	RCL
018	42	STO	041	42	STO	064	06	06
019	04	04	042	05	05	065	38	SIN
020	99	PRT	043	53	(066	54)
021	91	R/S	044	53	(067	54)
022	76	LBL	045	43	RCL	068	42	STO

069	07	07	120	43	RCL	171	69	OP
070	99	PRT	121	03	03	172	06	06
071	53	(122	38	SIN	173	91	R/S
072	53	(123	65	x	174	76	LBL
073	43	RCL	124	43	RCL	175	19	D'
074	00	00	125	07	07	176	53	(
075	75	-	126	54)	177	43	RCL
076	43	RCL	127	54)	178	06	06
077	05	05	128	42	STO	179	30	TAN
078	54)	129	10	10	180	35	1/x
079	55	÷	130	69	OP	181	54)
080	53	(131	06	06	182	42	STO
081	43	RCL	132	91	R/S	183	12	12
082	06	06	133	76	LBL	184	53	(
083	38	SIN	134	18	C'	185	43	RCL
084	54)	135	25	CLR	186	12	12
085	54)	136	69	OP	187	55	÷
086	42	STO	137	00	00	188	53	(
087	08	08	138	00	00	189	53	(
088	99	PRT	139	06	6	190	02	2
089	53	(140	02	2	191	65	x
090	43	RCL	141	07	7	192	43	RCL
091	07	07	142	03	3	193	11	11
092	85	+	143	02	2	194	54)
093	43	RCL	144	03	3	195	34	\sqrt{x}
094	08	08	145	03	3	196	54)
095	54)	146	69	OP	197	54)
096	42	STO	147	04	04	198	42	STO
097	09	09	148	53	(199	13	13
098	25	CLR	149	53	(200	99	PRT
099	69	OP	150	53	(201	91	R/S
100	00	00	151	43	RCL	202	76	LBL
101	01	1	152	04	04	203	11	A
102	03	3	153	65	x	204	53	(
103	03	3	154	05	5	205	53	(
104	05	5	155	93	.	206	53	(
105	01	1	156	01	1	207	53	(
106	07	7	157	02	2	208	43	RCL
107	01	1	158	54)	209	13	13
108	03	3	159	85	+	210	33	x^2
109	69	OP	160	03	3	211	54	(
110	04	04	161	54)	212	55	÷
111	53	(162	65	x	213	02	2
112	53	(163	93	.	214	54)
113	99	π	164	00	0	215	94	+/-
114	65	x	165	00	0	216	22	INV
115	43	RCL	166	01	1	217	23	LNx
116	08	08	167	54)	218	54)
117	54)	168	50	1x1	219	65	x
118	65	x	169	42	STO	220	53	(
119	53	(170	11	11	221	53	(

222	89	π	273	03	3	324	43	RCL
223	34	\sqrt{x}	274	08	8	325	15	15
224	65	x	275	01	1	326	45	Y ^x
225	02	2	276	05	5	327	04	4
226	54)	277	03	3	328	85	+
227	35	1/X	278	75	-	329	01	1
228	54)	279	93	.	330	93	.
229	54)	280	03	3	331	03	3
230	42	STO	281	05	5	332	03	3
231	14	14	282	06	6	333	00	0
232	53	(283	05	5	334	02	2
233	53	(284	06	6	335	07	7
234	53	(285	03	3	336	04	4
235	53	(286	07	7	337	04	4
236	43	RCL	287	08	8	338	02	2
237	13	13	288	02	2	339	09	9
238	65	x	289	65	x	340	00	0
239	93	.	290	43	RCL	341	65	x
240	02	2	291	15	15	342	43	RCL
241	03	3	292	33	x ²	343	15	15
242	01	1	293	85	+	344	45	Y ^x
243	06	6	294	01	1	345	05	5
244	04	4	295	93	.	346	54)
245	01	1	296	97	7	347	54)
246	09	9	297	08	8	348	42	STO
247	86	+	298	01	1	349	16	16
248	01	1	299	04	4	350	99	PRT
249	54)	300	07	7	351	91	R/S
250	35	1/x	301	07	7	352	76	LBL
251	54)	302	09	9	353	12	B
252	42	STO	303	03	3	354	53	(
253	15	15	304	07	7	355	53	(
254	53	(305	65	x	356	53	(
255	53	(306	43	RCL	357	43	RCL
256	43	RCL	307	15	15	358	13	13
257	14	14	308	45	Y ^x	359	33	x ²
258	65	x	309	03	3	360	94	+/-
259	01	1	310	75	-	361	22	INV
260	93	.	311	01	1	362	23	LN ^x
261	08	8	312	93	.	363	54)
262	01	1	313	08	8	364	75	-
263	54)	314	02	2	365	53	(
264	65	x	315	01	1	366	89	π
265	53	(316	02	2	367	34	\sqrt{x}
266	43	RCL	317	05	5	368	65	x
267	15	15	318	05	5	369	43	RCL
268	65	x	319	09	9	370	13	13
269	93	.	320	07	7	371	65	x
270	03	3	321	08	8	372	43	RCL
271	.01	1	322	00	0	373	16	16
272	09	9	323	65	x	374	54)

375	54)	426	99	PRT	477	14	D
376	55	÷	427	91	R/S	478	25	CLR
377	53	(428	76	LBL	479	69	OP
378	89	π	429	13	C	480	00	00
379	34	\sqrt{x}	430	25	CLR	481	01	1
380	65	x	431	69	OP	482	06	6
381	04	4	432	00	00	483	01	1
382	65	x	433	03	3	484	04	4
383	43	RCL	434	06	6	485	69	OP
384	13	13	435	01	1	486	04	04
385	54)	436	05	5	487	53	(
386	54)	437	01	1	488	53	(
387	42	STO	438	03	3	489	43	RCL
388	17	17	439	03	3	490	19	19
389	53	(440	07	7	491	28	LOG
390	53	(441	69	OP	492	54)
391	53	(442	04	04	493	65	x
392	01	1	443	53	(494	01	1
393	75	-	444	53	(495	00	0
394	53	(445	43	RCL	496	54)
395	53	(446	10	10	497	42	STO
396	53	(447	65	x	498	20	20
397	43	RCL	448	43	RCL	499	69	OP
398	17	17	449	18	18	500	06	06
399	65	x	450	54)	501	91	R/S
400	04	4	451	55	÷			
401	54)	452	53	(
402	94	+/-	453	53	(
403	54)	454	53	(
404	22	INV	455	53	(
405	23	LN _X	456	43	RCL			
406	54)	457	07	07			
407	54)	458	33	x ²			
408	65	x	459	54)			
409	53	(460	65	x			
410	01	1	461	08	8			
411	75	-	462	54)			
412	43	RCL	463	65	x			
413	16	16	464	89	π			
414	54)	465	54)			
415	54)	466	65	x			
416	55	÷	467	43	RCL			
417	53	(468	11	11			
418	43	RCL	469	54)			
419	17	17	470	54)			
420	65	x	471	42	STO			
421	04	4	472	19	19			
422	54)	473	69	OP			
423	54)	474	06	06			
424	42	STO	475	91	R/S			
425	18	18	476	76	LBL			

APPENDIX C

BUBBLE DYNAMICS TI 59 PROGRAM

A. INTRODUCTION

This program gives the resonant frequency f_r and the damping constant δ for bubbles according to Eq. (92). Furthermore, the program gives scattering cross section σ_s , extinction cross section σ_e , and absorption cross section σ_a as a function of bubble radius a , incoming frequency f , and depth z . The results of the calculations are given in Figs. 31 and 32.

B. PROGRAM STEPS

The user's instructions are as follows:

Procedure	Enter	Press	Display
Enter data	Bubble Radius	2nd A	a^1
Enter data	Incoming Frequency	R/S	f^1
Enter data	Depth	R/S	z^1
Calculate X	--	2nd B	X^1
Calculate coshX and sinhX	--	2nd C	$\cosh X^1$ $\sinh X^1$
Calculate d/b	--	2nd D	d/b^1
Calculate b	--	2nd E	b^1
Calculate β	--	A	β^1
Calculate f_r	--	B	f_r^1
Calculate δ	--	C	δ^1
Calculate σ	--	D	σ_e^1
Calculate σ_s and σ_a	--	E	σ_s^1 σ_a^1

¹These values are printed automatically if the calculator is connected to PC-100A Print Cradle.

The program steps are listed below giving location (LOC), code (COD), key (KEY) and comments.

000	76	LBL	043	55	÷	086	01	01
001	16	A'	044	43	RCL	087	99	PRT
002	42	STO	045	11	11	088	91	R/S
003	11	11	046	54)	089	76	LBL
004	99	PRT	047	85	+	090	18	C'
005	91	R/S	048	93	.	091	53	(
006	42	STO	049	00	0	092	53	(
007	12	12	050	00	0	093	43	RCL
008	99	PRT	051	01	1	094	01	01
009	91	R/S	052	02	2	095	22	INV
010	42	STO	053	09	9	096	23	LNx
011	13	13	054	65	x	097	85	+
012	99	PRT	055	53	(098	43	RCL
013	91	R/S	056	01	1	099	01	01
014	76	LBL	057	85	+	100	94	X/-
015	17	B'	058	93	.	101	22	INV
016	53	(059	01	1	102	23	LNx
017	53	(060	65	x	103	54)
018	53	(061	43	RCL	104	55	÷
019	53	(062	13	13	105	02	2
020	53	(063	54)	106	54)
021	53	(064	54)	107	42	STO
022	04	4	065	54)	108	02	02
023	65	x	066	65	x	109	99	PRT
024	89	π	067	93	.	110	53	(
025	54)	068	02	2	111	53	(
026	65	x	069	04	4	112	43	RCL
027	43	RCL	070	54)	113	01	01
028	12	12	071	55	÷	114	22	INV
029	54)	072	93	.	115	23	LNx
030	65	x	073	00	0	116	75	-
031	53	(074	00	0	117	43	RCL
032	53	(075	00	0	118	01	01
033	93	.	076	00	0	119	94	+/-
034	00	0	077	05	5	120	22	INV
035	00	0	078	06	6	121	23	LNx
036	00	0	079	54)	122	54)
037	00	0	080	34	\sqrt{x}	123	55	÷
038	00	0	081	65	x	124	02	2
039	00	0	082	43	RCL	125	54)
040	01	0	083	11	11	126	42	STO
041	09	9	084	54)	127	03	03
042	01	1	085	42	STO	128	99	PRT

129	91 R/S	180	53 (231	54)
130	76 LBL	181	01 1	232	54)
131	17 D'	182	93 .	233	55 ÷
132	53 (183	02 2	234	53 (
133	53 (184	65 x	235	43 RCL
134	53 (185	43 RCL	236	02 02
135	53 (186	01 01	237	75 -
136	43 RCL	187	54)	238	43 RCL
137	01 01	188	65 x	239	01 01
138	65 x	189	53 (240	39 COS
139	53 (190	43 RCL	241	54)
140	43 RCL	191	03 03	242	54)
141	03 03	192	75 -	243	85 +
142	85 +	193	43 RCL	244	01 1
143	43 RCL	194	01 01	245	54)
144	01 01	195	38 SIN	246	35 1/x
145	38 SIN	196	54)	247	65 x
146	54)	197	54)	248	53 (
147	54)	198	54)	249	54 (
148	75 -	199	54)	250	43 RCL
149	02 2	200	65 x	251	04 04
150	65 x	201	01 1	252	33 x ²
151	53 (202	93 .	253	54)
152	43 RCL	203	02 2	254	85 +
153	02 02	204	54)	255	01 1
154	75 -	205	42 STO	256	54)
155	43 RCL	206	04 04	257	35 1/x
156	01 01	207	99 PRT	258	54)
157	39 COS	208	91 R/S	259	42 STO
158	54)	209	76 LBL	260	05 05
159	54)	210	10 E	261	99 PRT
160	55 ÷	211	53 (262	91 R/S
161	53 (212	53 (263	76 LBL
162	53 (213	53 (264	11 A
163	53 (214	53 (265	53 (
164	43 RCL	215	53 (266	53 (
165	01 01	216	03 3	267	53 (
166	33 x ²	217	93 .	268	01 1
167	54)	218	02 2	269	05 5
168	65 x	219	55 ÷	270	00 0
169	53 (220	43 RCL	271	55 ÷
170	43 RCL	221	01 01	272	53 (
171	02 02	222	54)	273	01 1
172	75 -	223	65 x	274	00 0
173	43 RCL	224	53 (275	01 1
174	01 01	225	43 RCL	276	03 3
175	39 COS	226	03 03	277	00 0
176	54)	227	75 -	278	00 0
177	54)	228	43 RCL	279	00 0
178	85 +	229	01 01	280	65 x
179	53 (230	38 SIN	281	43 RCL

282 11 11
 283 65 x
 284 53 (
 285 01 1
 286 85 +
 287 93 .
 288 01 1
 289 65 x
 290 43 RCL
 291 13 13
 292 54)
 293 54)
 294 54)
 295 65 x
 296 53)
 297 01 1
 298 75 -
 299 53 (
 300 53 (
 301 04 4
 302 93 .
 303 02 2
 304 65 x
 305 43 RCL
 306 05 05
 307 54)
 308 35 1/x
 309 54)
 310 54)
 311 54)
 312 85 +
 313 01 1
 314 54)
 315 42 STO
 316 06 06
 317 99 PRT
 318 91 R/S
 319 76 LBL
 320 12 B
 321 53 (
 322 53 (
 323 53 (
 324 53 (
 325 04 4
 326 93 .
 327 02 2
 328 65 x
 329 43 RCL
 330 05 05
 331 65 x
 332 43 RCL

333 06 06
 334 65 x
 335 01 1
 336 00 0
 337 01 1
 338 03 3
 339 00 0
 340 00 0
 341 00 0
 342 54)
 343 65 x
 344 53 (
 345 01 1
 346 85 +
 347 93 .
 348 01 1
 349 65 x
 350 43 RCL
 351 13 13
 352 52)
 353 54)
 354 55 ÷
 355 01 1
 356 93 .
 357 00 0
 358 02 2
 359 06 6
 360 54)
 361 50 1x1
 362 34 \sqrt{x}
 363 65 x
 364 53 (
 365 53 (
 366 89 π
 367 65 x
 368 02 2
 369 65 x
 370 43 RCL
 371 11 11
 372 54)
 373 35 1/x
 374 54)
 375 54)
 376 42 STO
 377 07 07
 378 99 PRT
 379 91 R/S
 380 76 LBL
 381 13 C
 382 53 (
 383 53 (

384 53 (
 385 93 .
 386 00 0
 387 00 0
 388 00 0
 389 00 0
 390 04 4
 391 01 1
 392 08 8
 393 08 8
 394 07 7
 395 09 9
 396 65 x
 397 43 RCL
 398 12 12
 399 65 x
 400 43 RCL
 401 11 11
 402 54)
 403 85 +
 404 53 (
 405 43 RCL
 406 04 04
 407 65 x
 408 53 (
 409 53 (
 410 43 RCL
 411 07 07
 412 55 ÷
 413 43 RCL
 414 12 12
 415 54)
 416 33 x^2
 417 54)
 418 54)
 419 54)
 420 85 +
 421 53 (
 422 93 =
 423 00 0
 424 00 0
 425 06 6
 426 02 2
 427 00 0
 428 05 5
 429 55 ÷
 430 53 (
 431 43 RCL
 432 12 12
 433 65 x
 434 53 (

435	43	RCL	486	43	RCL	537	33	x ²
436	11	11	487	07	07	538	54)
437	33	x ²	488	55	÷	539	75	-
438	54)	489	43	RCL	540	01	1
439	54)	490	12	12	541	54)
440	54)	491	54)	542	33	x ²
441	54)	492	33	x ²	543	53)
442	42	STO	493	54)	544	85	+
443	08	08	494	75	-	545	53	(
444	99	PRT	495	01	1	546	43	RCL
445	91	R/S	496	54)	547	08	08
446	76	LBL	497	33	x ²	548	33	x ²
447	14	D	498	54)	549	54)
448	53	(499	85	+	550	54)
449	53	(500	53	(551	54)
450	04	4	501	43	RCL	552	42	STO
451	65	x	502	08	08	553	10	10
452	89	π	503	33	x ²	554	99	PRT
453	65	x	504	54)	555	66	PAU
454	43	RCL	505	54)	556	53	(
455	11	11	506	54)	557	43	RCL
456	54)	507	42	STO	558	09	09
457	65	x	508	09	09	559	75	-
458	53	(509	99	PRT	560	43	RCL
459	53	(510	91	R/S	561	10	10
460	43	RCL	511	76	LBL	562	54)
461	08	08	512	15	E	563	42	STO
462	65	x	513	53	(564	11	11
463	01	1	514	53	(565	99	PRT
464	05	5	515	04	4	566	91	R/S
465	00	0	516	65	x			
466	00	0	517	89	π			
467	00	0	518	65	x			
468	00	0	519	53	(
469	55	÷	520	43	RCL			
470	53	(521	11	11			
471	89	π	522	33	x ²			
472	65	x	523	54)			
473	02	2	524	54)			
474	65	x	525	55	÷			
475	43	RCL	526	53	(
476	12	12	527	53	(
477	54)	528	53	(
478	54)	529	53	(
479	54)	530	53	(
480	55	÷	531	43	RCL			
481	53	(532	07	07			
482	53	(533	55	÷			
483	53	(534	43	RCL			
484	53	(535	12	12			
485	53	(536	54)			

APPENDIX D

NUMERICAL INTEGRATION TI 59 PROGRAM

A. INTRODUCTION

In order to perform the numerical integration of $\sigma(a)da$, a standard Texas Instrument's program was used [Ref. 25]. This program performs the integration by using Simpson's discrete approximation based on the following expression

$$I = \int_{x_0}^{x_n} f(x) dx \approx \frac{h}{3} (f_0 + 4f_1 + 2f_2 + 4f_3 + 2f_4 + \dots + 2f_{n-2} + 4f_{n-1} + f_n)$$

where

$f(x)$ must be known at $n+1$ equally spaced points ($f_0 - f_n$).

$$h = \frac{x_n - x_0}{n} ; x_n > x_0$$

$n+7 \leq$ number of data registers available

n = number of subintervals = 2, 4, 6,

B. PROGRAM INSTRUCTIONS

The program is taken from the master library program package by using the code 2nd Pgm 10 on the calculator.

The user's instructions are as follows

Procedure	Enter	Press	Display
Enter data	Subintervals	A	n^1
Enter data	h	B	h^1
Enter data	Function values		
	0	C	0
	f_0	R/S	f_0^1
	f_1	R/S	f_1^1
	.	.	
	.	.	
	f_n	R/S	f_n^1
Calculate	-	D	I^1

¹These values are printed automatically if the calculator is connected to PC-100A Print Cradle.

The program steps are listed below giving location (LOC), key symbol (KEY), and comments.

000	76	LBL	019	99	PRT	038	06	6
001	11	A	020	92	RTN	039	54)
002	53	(021	76	LBL	040	42	STO
003	50	1x1	022	52	EE	041	01	01
004	42	STO	023	00	0	042	32	$x \leq t$
005	05	05	024	35	1/x	043	98	ADV
006	55	÷	025	92	RTN	044	92	RTN
007	02	2	026	76	LBL	045	76	LBL
008	54)	027	12	B	046	50	1x1
009	42	STO	028	42	STO	047	76	ST*
010	02	02	029	03	03	048	01	01
011	22	INV	030	99	PRT	049	32	$x \geq t$
012	59	INT	031	92	RTN	050	01	1
013	29	CP	032	76	LBL	051	44	SUM
014	22	INV	033	13	C	052	01	01
015	67	EQ	034	53	(053	32	$x \leq t$
016	52	EE	035	24	CE	054	99	PRT
017	43	RCL	036	85	+	055	92	RTN
018	05	05	037	32	$x \leq t$	056	61	GTO

057	50	1x1	108	44	SUM
058	76	LBL	109	04	04
059	14	D	110	53	(
060	53	(111	43	RCL
061	43	RCL	112	03	03
062	05	05	113	55	÷
063	85	+	114	03	3
064	06	6	115	54)
065	54)	116	49	PRD
066	42	STO	117	04	04
067	01	01	118	43	RCL
068	73	RC*	119	04	04
069	01	01	120	98	ADV
070	42	STO	121	99	PRT
071	04	04	122	92	RTN
072	76	LBL			
073	45	y ^x			
074	01	1			
075	22	INV			
076	44	SUM			
077	01	01			
078	53	(
079	73	RC*			
080	01	01			
081	65	x			
082	04	4			
083	54)			
084	44	SUM			
085	04	04			
086	01	1			
087	22	INV			
088	44	SUM			
089	01	01			
090	22	INV			
091	97	DSZ			
092	02	02			
093	33	x ²			
094	53	(
095	73	RC*			
096	01	01			
097	65	x			
098	02	2			
099	54)			
100	44	SUM			
101	04	04			
102	61	GTO			
103	45	y ^x			
104	76	LBL			
105	33	x ²			
106	73	RC*			
107	01	01			

APPENDIX E

TURN RATE LIMITATION TI 59 PROGRAMS

A. INTRODUCTION

The turn rate limitation calculations are divided into two parts with separate programs.

B. PART I PROGRAM

For a given initial detection range and a given ship speed, Part I performs a sequential calculation of $\phi_A, K_A, \phi_B, K_B, \phi^*$ and K^* for each of the maximum turn rates investigated, together with the "no limit" conditions $(V_s)_{NL}$ and K_{NL} based on

$$\phi_A = \sin^{-1} \left(\frac{3p|\dot{\phi}|_{\max}}{V_s} \right); \leq 90^\circ$$

$$\phi_B = 180^\circ - \phi_A$$

$$K_{A,B} = \frac{V_s (1 + \cos \phi_{A,B})^P}{|\dot{\phi}|_{\max} (\sin \phi_{A,B})^{P-2}}$$

$$\phi^* = \cos^{-1} (P-2)$$

$$K^* = \frac{V_s (1+P/2)^P [1-(P/2)^2]^{1-P/2}}{|\dot{\phi}|_{\max}}$$

$$(V_s)_{NL} = (3V_T |\dot{\phi}|_{\max})^{1/2}$$

$$K_{NL} = 3p$$

For $p > 2$, the solution for ϕ^* and K^* are not valid. Furthermore, for $V_S (V_S)_{NL}$ no solutions are valid for any of the quantities.

The program is based on the fixed torpedo speed of $V_T = 35$ kts (18 m/s) and an initial detection range of $T_O = R_D = 250$ m.

The user instructions for the program are as follows:

Procedure	Enter	Press	Display
Enter data	Maximum Turn Rate	A	$ \phi _{\max}^1$
Enter data	Ship speed	B	V_T^1
Calculate ϕ^* and K^*	--	C	$\phi^*, K^*{}^1$
Calculate ϕ_A and ϕ_B	--	D	ϕ_A, ϕ_B^1
Calculate K_A and K_B	--	E	K_A, K_B^1

¹These values are printed automatically if the calculator is connected to PC-100A Print Cradle.

A listing of the program steps follows giving location (LOC), code (COD), key symbol (KEY), and comments.

000 76 LBL	012 69 OP	024 54)
001 11 A	013 00 00	025 42 STO
002 42 STO	014 03 3	026 03 03
003 01 01	015 03 3	027 69 OP
004 99 PRT	016 69 OP	028 06 06
005 91 R/S	017 04 04	029 25 CLR
006 76 LBL	018 53 (030 69 OP
007 12 B	019 01 1	031 00 00
008 42 STO	020 08 8	032 02 2
009 02 02	021 55 ÷	033 06 6
010 99 PRT	022 43 RCL	034 03 3
011 25 CLR	023 02 02	035 01 1

036	02	2	087	03	3	138	45	y^x
037	07	7	088	03	3	139	43	RCL
038	69	OP	089	02	2	140	03	03
039	04	04	090	03	3	141	54)
040	53	(091	05	5	142	54)
041	43	RCL	092	01	1	143	65	x
042	03	03	093	69	OP	144	53	(
043	65	x	094	04	04	145	53	(
044	03	3	095	53	(146	01	1
045	54)	096	53	(147	75	-
046	42	STO	097	53	(148	53	(
047	10	10	098	43	RCL	149	53	(
048	69	OP	099	03	03	150	43	RCL
049	06	06	100	55	÷	151	03	03
050	25	CLR	101	02	2	152	55	÷
051	69	OP	102	54)	153	02	2
052	00	00	103	22	INV	154	54)
053	04	4	104	39	COS	155	33	x^2
054	02	2	105	54)	156	54)
055	03	3	106	54)	157	54)
056	06	6	107	42	STO	158	45	y^x
057	03	3	108	04	04	159	53	(
058	01	1	109	69	OP	160	01	1
059	02	2	110	06	06	161	75	-
060	07	7	111	25	CLR	162	53	(
061	69	OP	112	69	OP	163	43	RCL
062	04	04	113	00	00	164	03	03
063	53	(114	02	2	165	55	÷
064	53	(115	06	6	166	02	2
065	53	(116	05	5	167	54)
066	03	3	117	01	1	168	54)
067	65	x	118	69	OP	169	54)
068	01	1	119	04	04	170	54)
069	08	8	120	53	(171	55	÷
070	54)	121	53	(172	43	RCL
071	65	x	122	53	(173	01	01
072	43	RCL	123	53	(174	54)
073	01	01	124	43	RCL	175	42	STO
074	54)	125	02	02	176	05	05
075	34	\sqrt{x}	126	65	x	177	69	OP
076	54)	127	53	(178	06	06
077	42	STO	128	53	(179	91	R/S
078	11	11	129	01	1	180	76	LBL
079	69	OP	130	85	+	181	14	D
080	06	06	131	53	(182	25	CLR
081	91	R/S	132	43	RCL	183	69	OP
082	76	LBL	133	03	03	184	00	00
083	13	C	134	55	÷	185	03	3
084	25	CLR	135	02	2	186	03	3
085	69	OP	136	54)	187	02	2
086	00	00	137	54)	188	03	3

189	01	1	240	06	06	291	54)
190	03	3	241	91	R/S	292	54)
191	69	OP	242	76	LBL	293	54)
192	04	04	243	15	E	294	42	STO
193	53	(244	25	CLR	295	08	08
194	53	(245	69	OP	296	69	OP
195	53	(246	00	00	297	06	06
196	53	(247	02	2	298	25	CLR
197	53	(248	06	6	299	69	OP
198	43	RCL	249	01	1	300	00	00
199	03	03	250	03	3	301	02	2
200	65	x	251	69	OP	302	06	6
201	03	3	252	04	04	303	01	1
202	54)	253	53	(304	04	4
203	65	x	254	53	(305	69	OP
204	43	RCL	255	43	RCL	306	04	04
205	01	01	256	02	02	307	53	(
206	54)	257	65	x	308	53	(
207	55	÷	258	53	(309	43	RCL
208	43	RCL	259	53	(310	02	02
209	02	02	260	01	1	311	65	x
210	54)	261	85	+	312	53	(
211	22	INV	262	53	(313	53	(
212	38	SIN	263	43	RCL	314	01	1
213	54)	264	06	06	315	85	+
214	42	STO	265	39	COS	316	53	(
215	06	06	266	54)	317	43	RCL
216	69	OP	267	54)	318	07	07
217	06	06	268	45	y ^x	319	39	COS
218	25	CLR	269	43	RCL	320	54)
219	69	OP	270	03	03	321	54)
220	00	00	271	54)	322	45	y ^x
221	03	3	272	54)	323	43	RCL
222	03	3	273	55	÷	324	03	03
223	02	2	274	53	(325	54)
224	03	3	275	43	RCL	326	54)
225	01	1	276	01	01	327	55	÷
226	04	4	277	65	x	328	53	(
227	69	OP	278	53	(329	43	RCL
228	04	04	279	53	(330	01	01
229	53	(280	43	RCL	331	65	x
230	01	1	281	06	06	332	53	(
231	08	8	282	38	SIN	333	53	(
232	00	0	283	54)	334	43	RCL
233	75	-	284	45	y ^x	335	07	07
234	43	RCL	285	53	(336	38	SIN
235	06	06	286	43	RCL	337	54)
236	54)	287	03	03	338	45	y ^x
237	42	STO	288	75	-	339	53	(
238	07	07	289	02	2	340	43	RCL
239	69	OP	290	54)	341	03	03

342 75 -
 343 02 2
 344 54)
 345 54)
 346 54)
 347 54)
 348 42 STO
 349 09 09
 350 69 OP
 351 06 06
 352 91 R/S
 353 02 2
 354 54)
 355 54)
 356 54)
 357 54)
 358 42 STO
 359 09 09
 360 69 OP
 361 06 06
 362 91 R/S

C. PART II PROGRAM

Given K from Part I, Part II program performs the probe calculations of the corresponding initial approach angles $(\phi_0)_A$, $(\phi_0)_B$, $(\phi_0)^*$, and $(\phi_0)_{NL}$ based on the relationship

$$f(\phi_0) = K_{A,B,*,NL} [\sin(\phi_0)_{A,B,*,NL}]^{P-1} \\
 -r_0 [(1+(\cos\phi_0)_{A,B,*,NL})^P] = 0$$

The program used a fixed torpedo speed of $V_T = 35$ kts (18 m/s) and an initial detection range of $r_0 = R_D = 250$ m. The purpose of this general probe program is to locate roots of the given function $y = f(\phi_0)$ to evaluate the slope of the tangent line, and to find the maximum and minimum points on a graph. We will only use the first feature.

The program requires a subroutine for the function to be investigated. This subroutine starts at program location 140 and is located at label 2nd C. The user's instructions for the program are as follows:

Procedure	Enter	Press	Display
Enter data	Starting Value of ϕ_0	2nd D	ϕ_0
Enter data	The increment $\Delta\phi_0$	2nd E	$\Delta\phi_0$
Calculate $f(\phi_0 + \Delta\phi_0)$	--	A	$f(\phi_0 + \Delta\phi_0)$
Calculate $f(\phi_0 - \Delta\phi_0)$	--	B	$f(\phi_0 - \Delta\phi_0)$
Display current value of ϕ_0	--	E	ϕ_0

If the value of $\Delta\phi_0$ is chosen too large, $\Delta\phi_0$ may be replaced by $\Delta\phi_0/10$ by pressing label 2nd A. Similarly, if a larger value of $\Delta\phi_0$ is required, $\Delta\phi_0$ can be replaced by $10\Delta\phi_0$ by pressing label 2nd B. A listing of the program steps follows, giving location (LOC), code (COD), key symbol (KEY), and comments.

Associated with the subroutine, it should be noted that the value of K, r_0 and p are entered separately in the memory locations 10, 11, and 12, respectively.

000	76	LBL	051	42	STO	102	75	-
001	19	D'	052	03	03	103	43	RCL
002	42	STO	053	53	(104	04	04
003	01	01	054	43	RCL	105	54)
004	91	R/S	055	01	01	106	55	÷
005	76	LBL	056	75	-	107	43	RCL
006	10	E'	057	43	RCL	108	02	02
007	42	STO	058	02	02	109	54)
008	02	02	059	55	÷	110	91	R/S
009	91	R/S	060	02	2	111	76	LBL
010	76	LBL	061	54)	112	15	E
011	11	A	062	71	SBR	113	43	RCL
012	53	(063	18	C'	114	01	01
013	43	RCL	064	42	STO	115	91	R/S
014	01	01	065	04	04	116	76	LBL
015	85	+	066	53	(117	16	A'
016	43	RCL	067	53	(118	53	(
017	02	02	068	43	RCL	119	43	RCL
018	54)	069	03	03	120	02	02
019	42	STO	070	75	-	121	55	÷
020	01	01	071	43	RCL	122	01	1
021	71	SBR	072	04	04	123	00	0
022	18	C'	073	54)	124	54)
023	91	R/S	074	55	÷	125	42	STO
024	76	LBL	075	43	RCL	126	02	02
025	12	B	076	02	02	127	91	R/S
026	53	(077	54)	128	76	LBL
027	43	RCL	078	91	R/S	129	17	B'
028	01	01	079	76	LBL	130	53	(
029	75	-	080	14	D	131	43	RCL
030	43	RCL	081	53	(132	02	02
031	02	02	082	43	RCL	133	65	x
032	54)	083	01	01	134	01	1
033	42	STO	084	85	+	135	00	0
034	01	01	085	43	RCL	136	54)
035	71	SBR	086	02	02	137	42	STO
036	18	C'	087	54)	138	02	02
037	91	R/S	088	71	SBR	139	91	R/S
038	76	LBL	089	18	C'	140	76	LBL
039	13	C	090	42	STO	141	18	C'
040	53	(091	03	03	142	42	STO
041	43	RCL	092	43	RCL	143	00	00
042	01	01	093	01	01	144	70	RAD
043	85	+	094	71	SBR	145	53	(
044	43	RCL	095	18	C'	146	53	(
045	02	02	096	42	STO	147	43	RCL
046	55	÷	097	04	04	148	10	10
047	02	2	098	53	(149	65	x
048	54)	099	53	(150	53	(
049	71	SBR	100	43	RCL	151	53	(
050	18	C'	101	43	RCL	152	43	RCL

153 00 00
154 38 SIN
155 54)
156 45 y^x
157 43 RCL
158 13 13
159 54)
160 54)
161 75 -
162 53 (
163 43 RCL
164 11 11
165 65 x
166 53 (
167 53 (
168 01 1
169 85 +
170 53 (
171 43 RCL
172 00 00
173 39 COS
174 54)
175 54)
176 45 y^x
177 43 RCL
178 12 12
179 54)
180 54)
181 54)
182 92 RTN

APPENDIX F
FIGURES

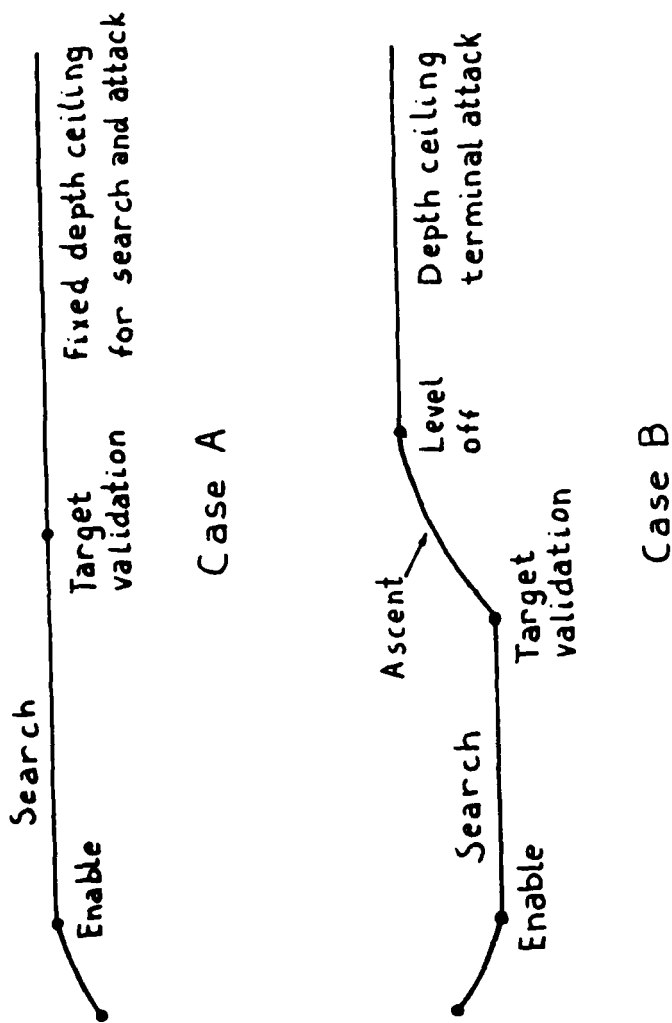


Fig. 1. Torpedo Search and Attack Geometry.

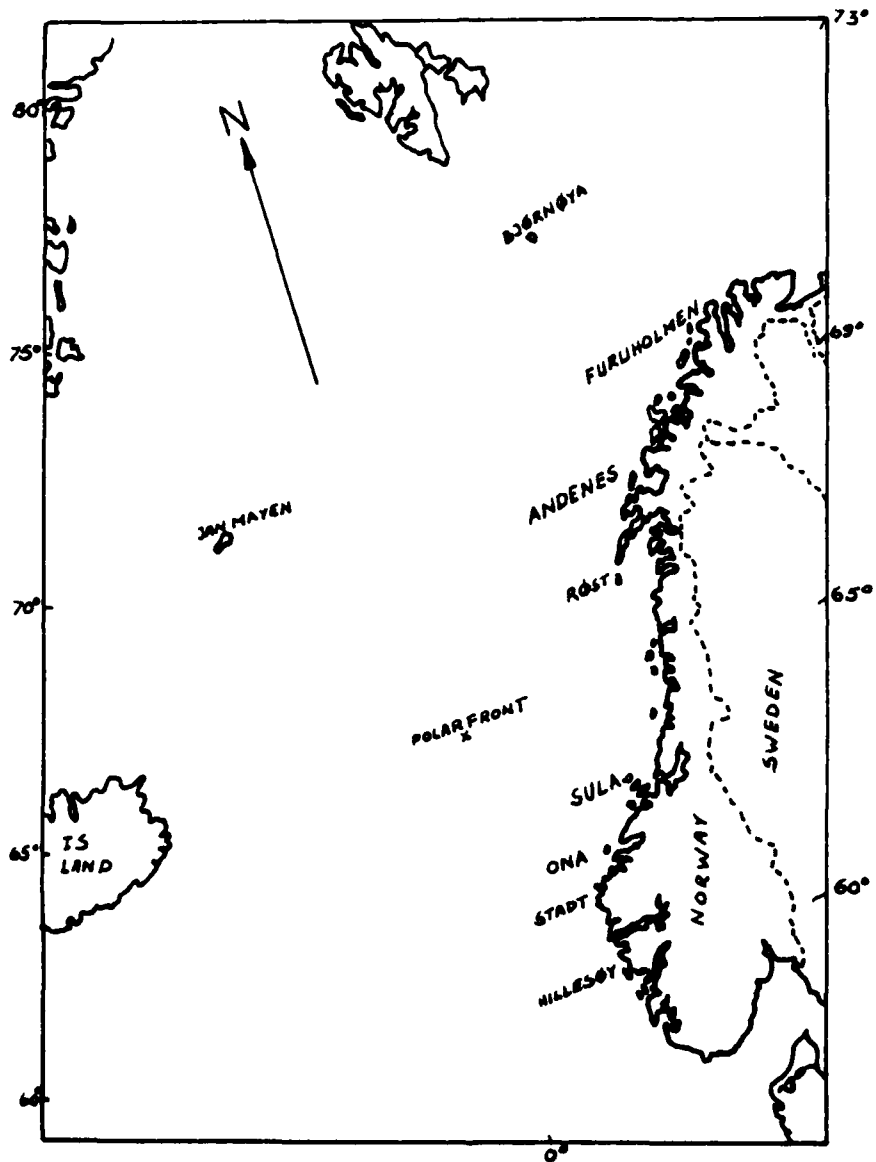


Fig. 2. Location of Weather Stations Along the Norwegian Coast.

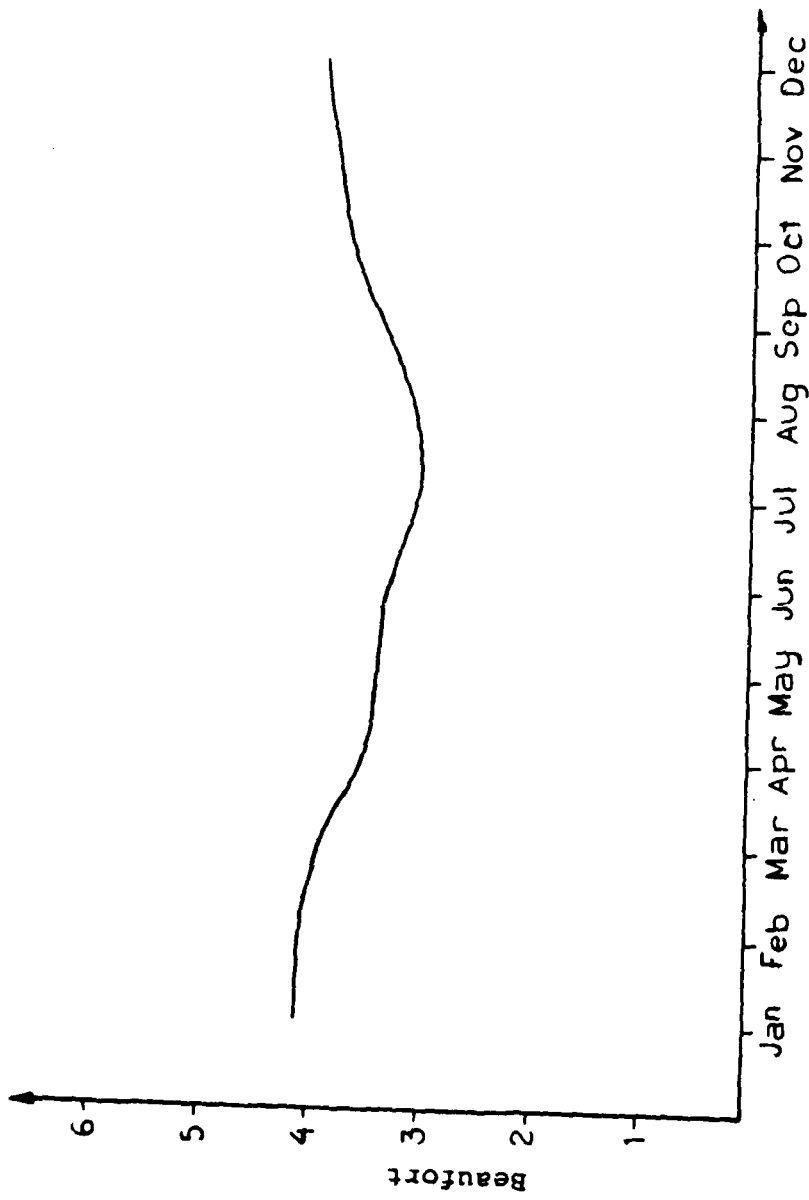


Fig. 3. Average Monthly Wind Speed in Beaufort from the Weather Station "Andenes."

Reproduction of this document is authorized for personal use only. All rights reserved.

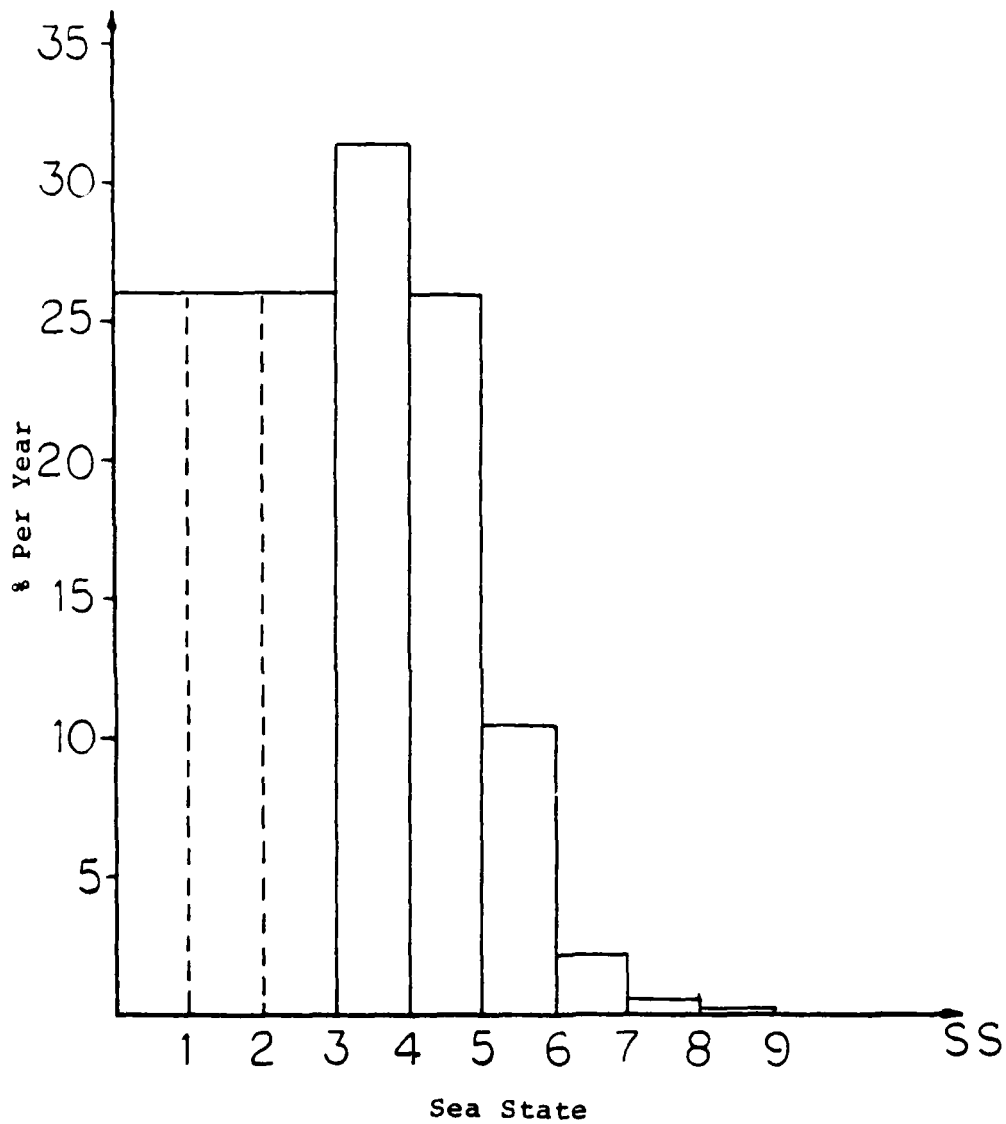


Fig. 4. Histogram of Significant Wave in Percent per Year from the Weather Station "Andenes."

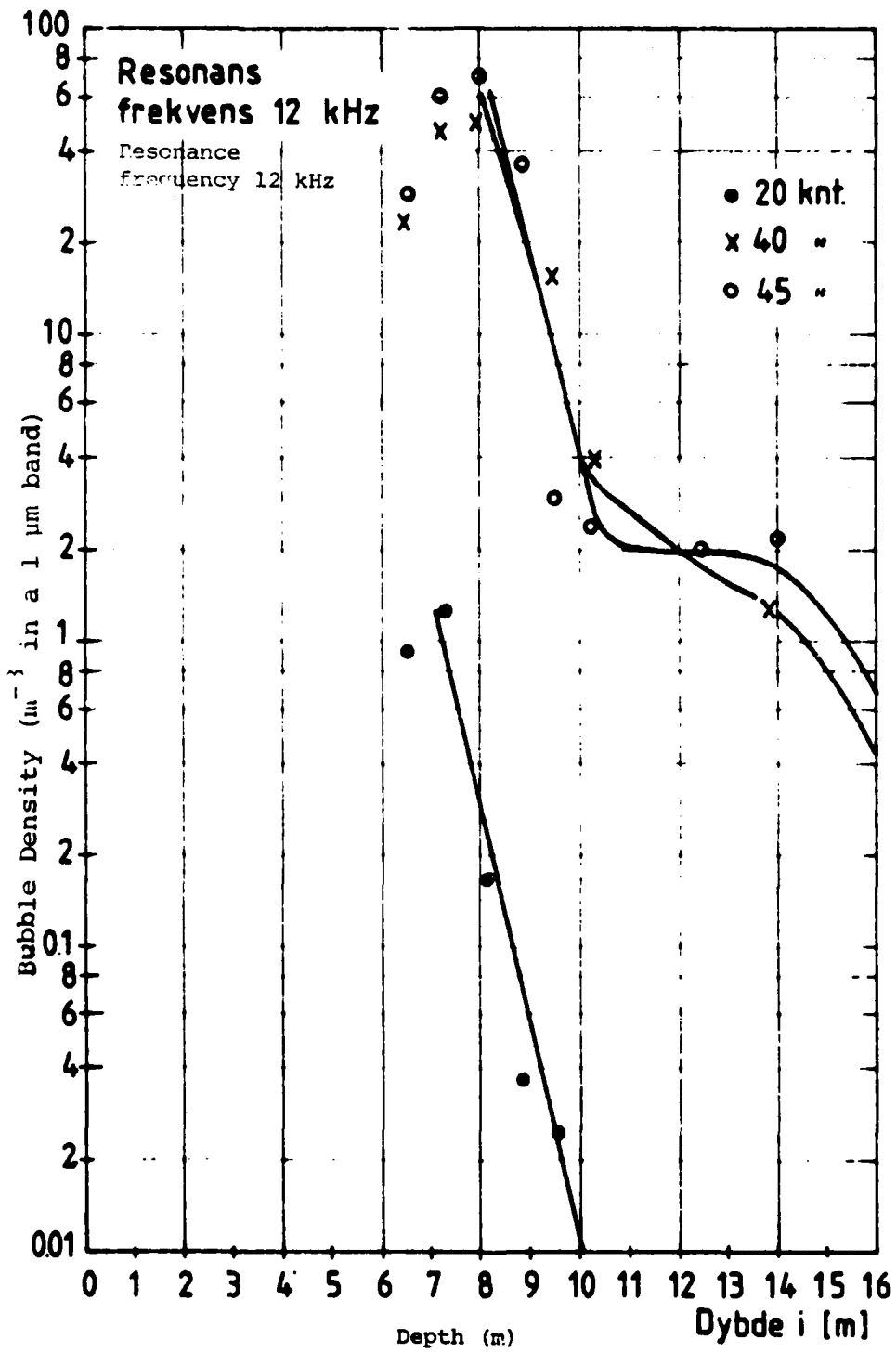


Fig. 5. Resonant Bubble Density at 12 kHz as a Function of Depth.

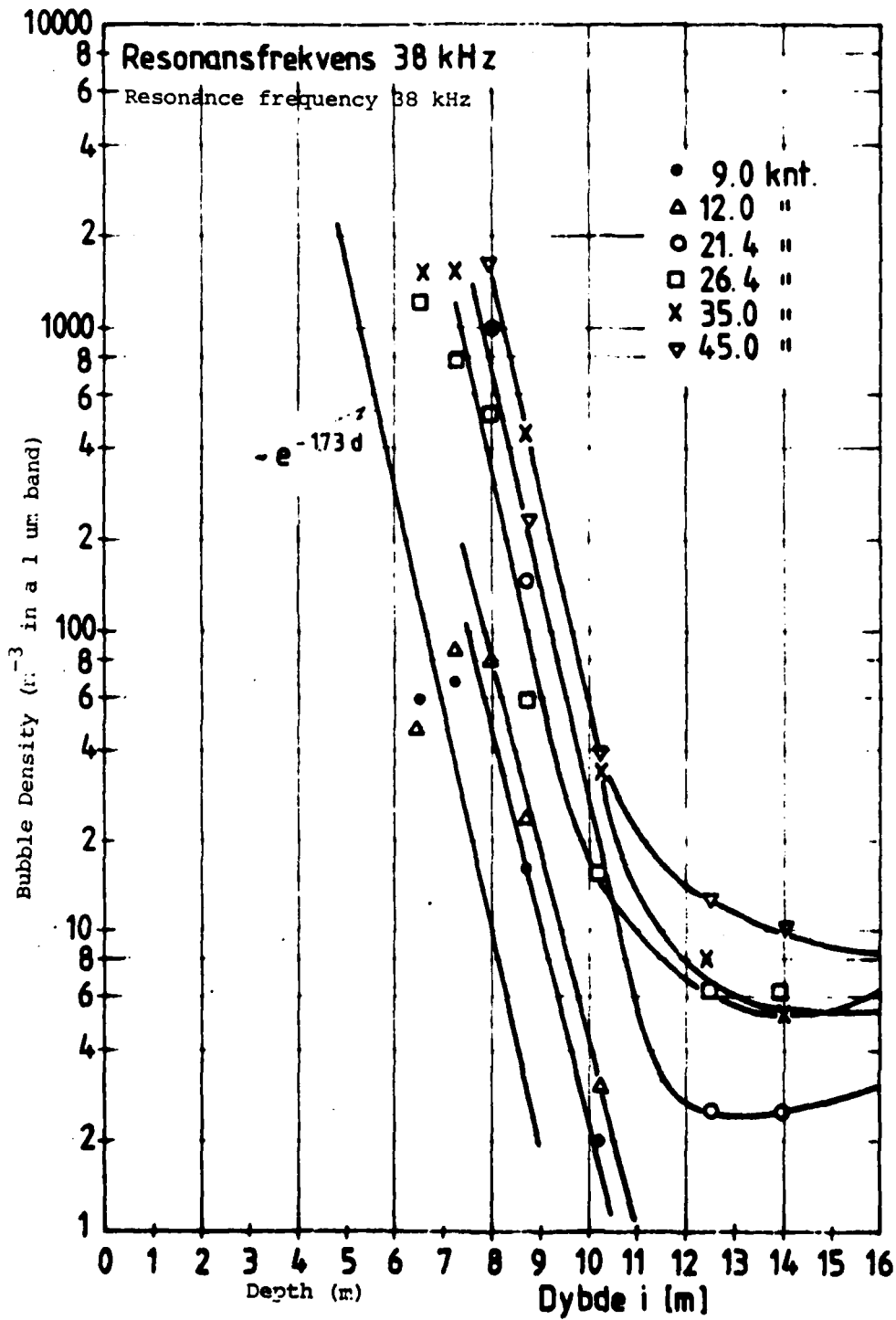


Fig. 6. Resonant Bubble Density at 38 kHz as a Function of Depth.

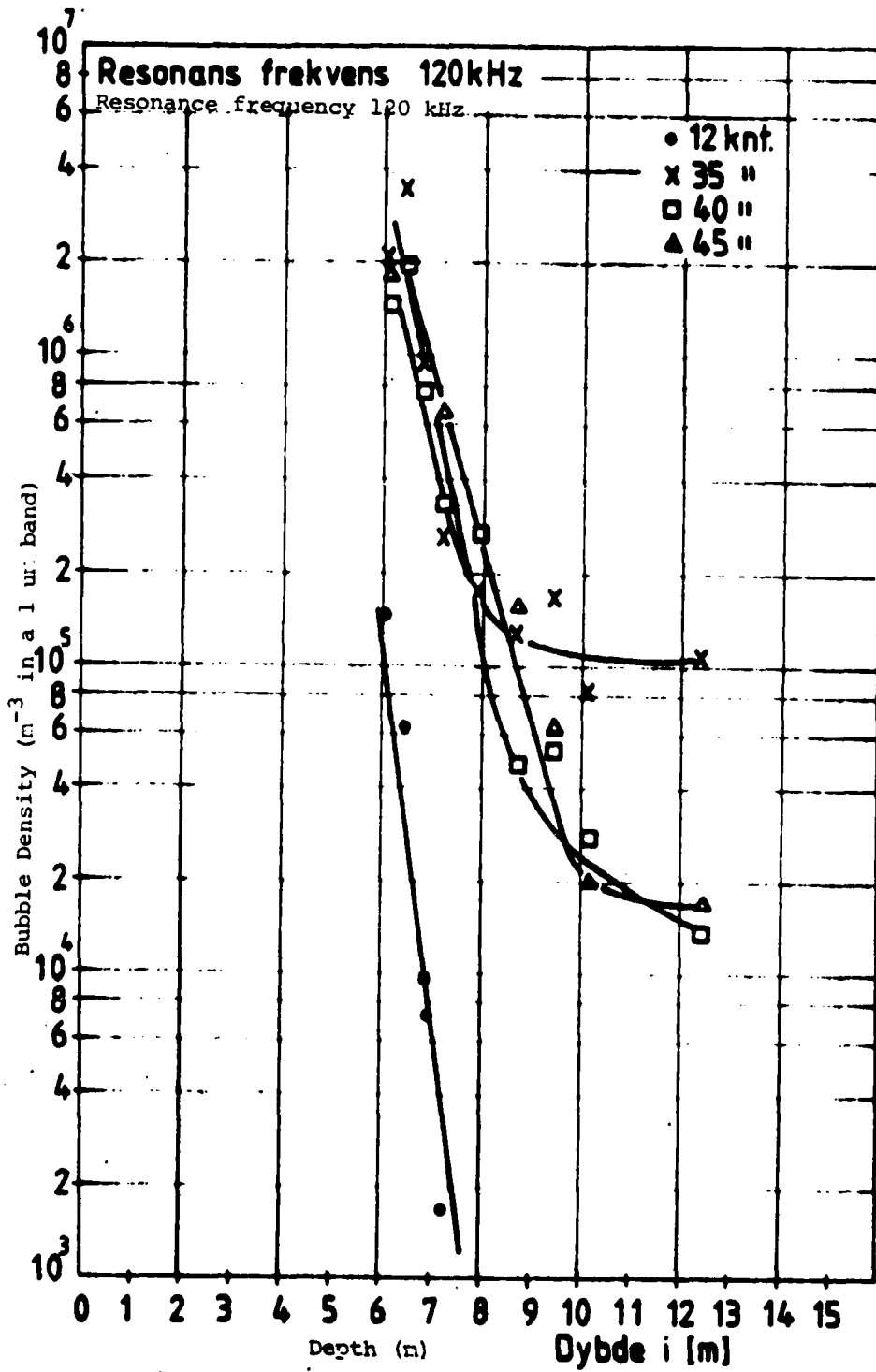


Fig. 7. Resonant Bubble Density at 120 kHz as a Function of Depth.

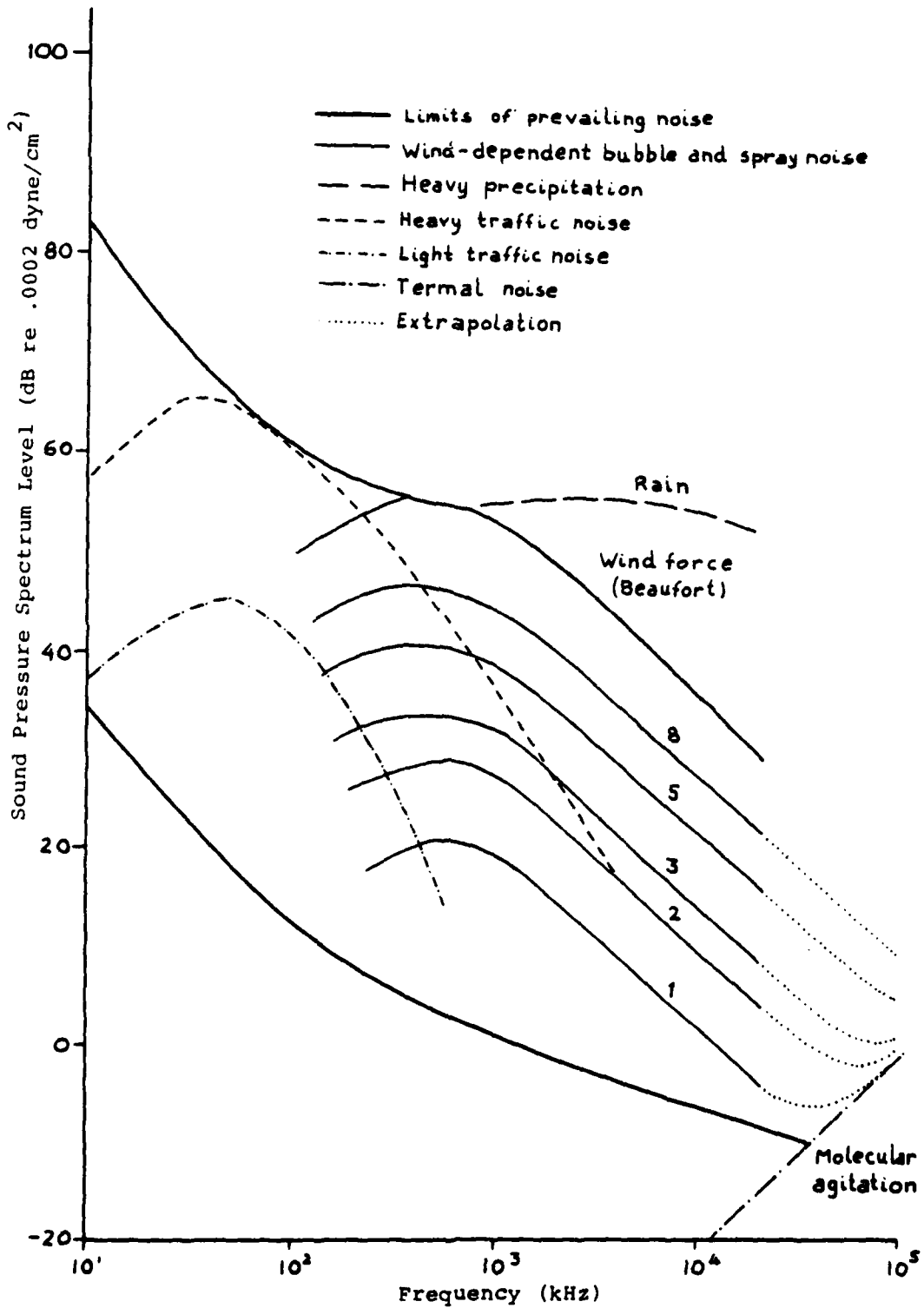


Fig. 8. Ambient Noise Level Curves.

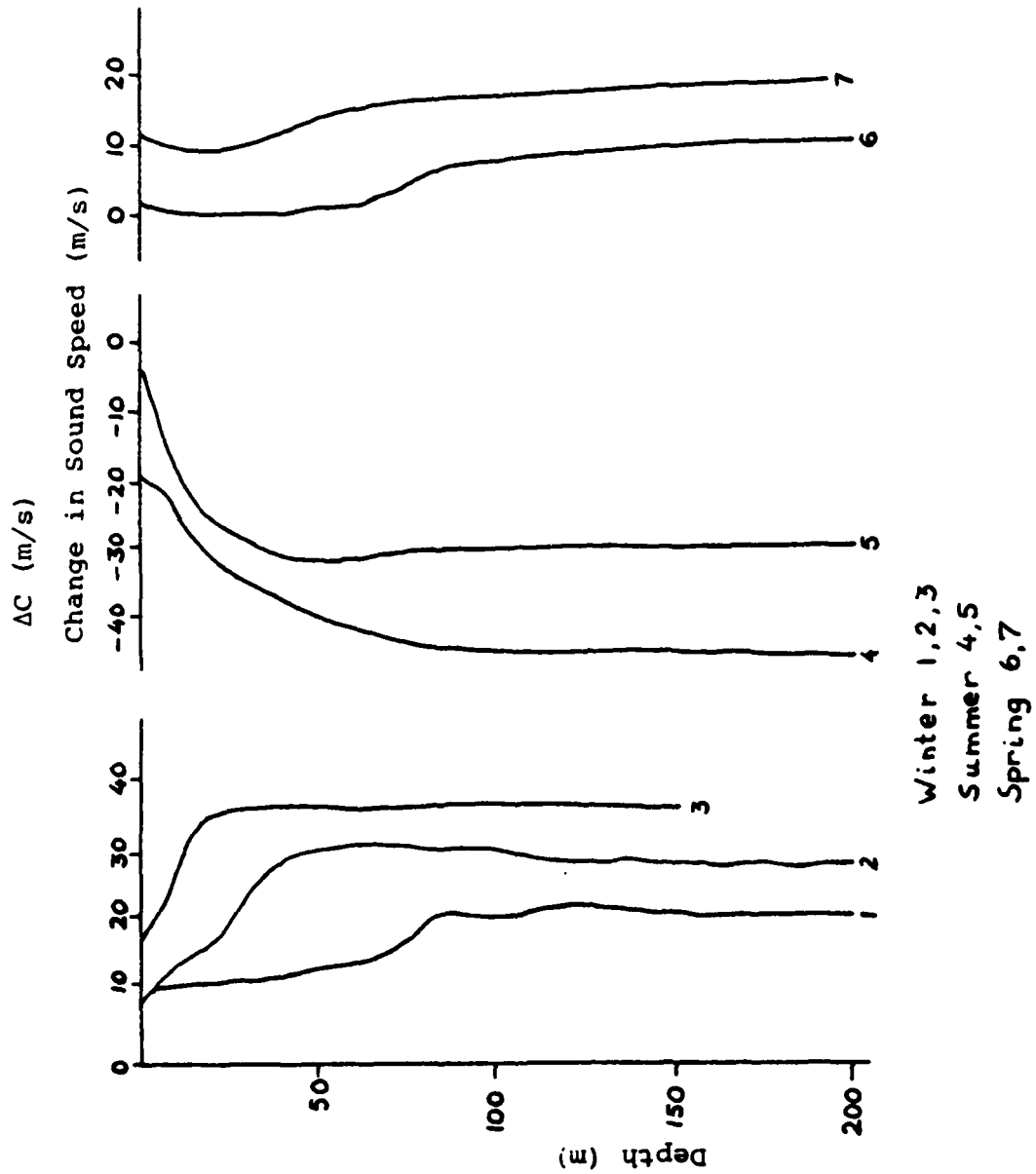
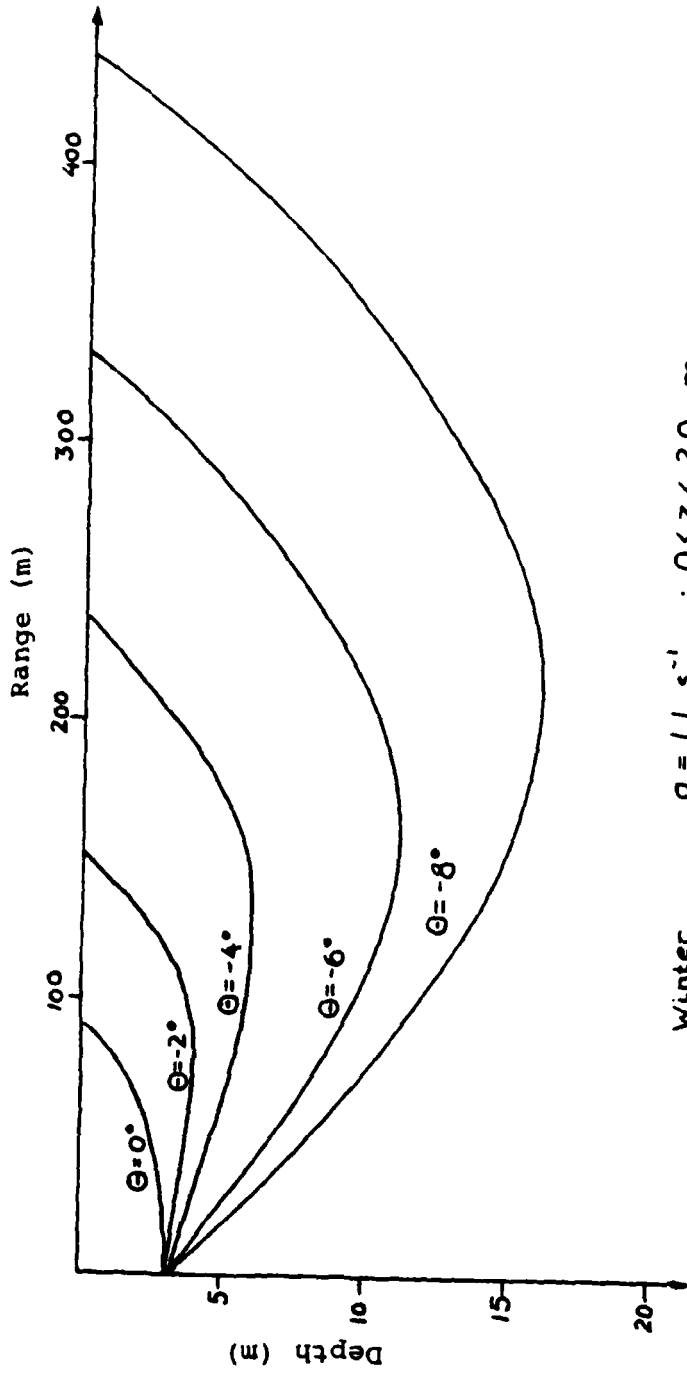
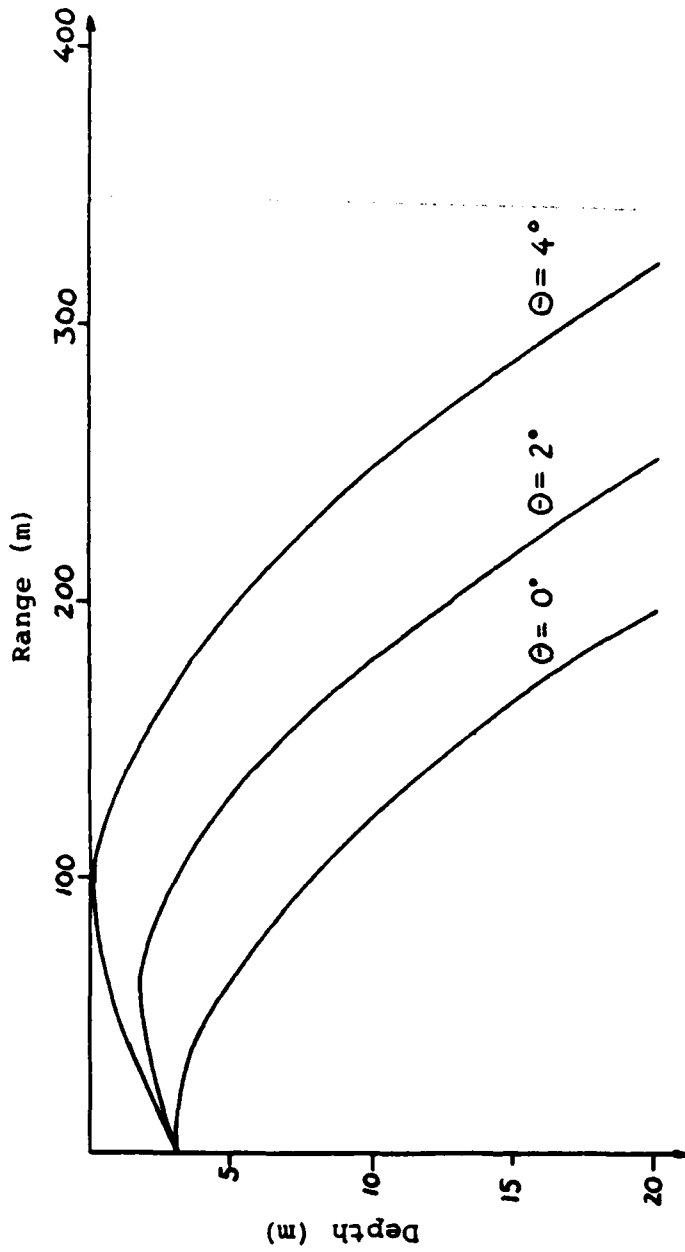


Fig. 9. Typical Sound Speed Profiles in Norwegian Coastal Waters.



Winter , $g = 1.1 \text{ s}^{-1}$; $0 < z < 20 \text{ m}$

Fig. 10. Worst Case Ray Path During Winter.



Summer, $g = 1.25 \text{ s}^{-1}$; $0 < z < 20 \text{ m}$

Fig. 11. Worst Case Ray Path During Summer.

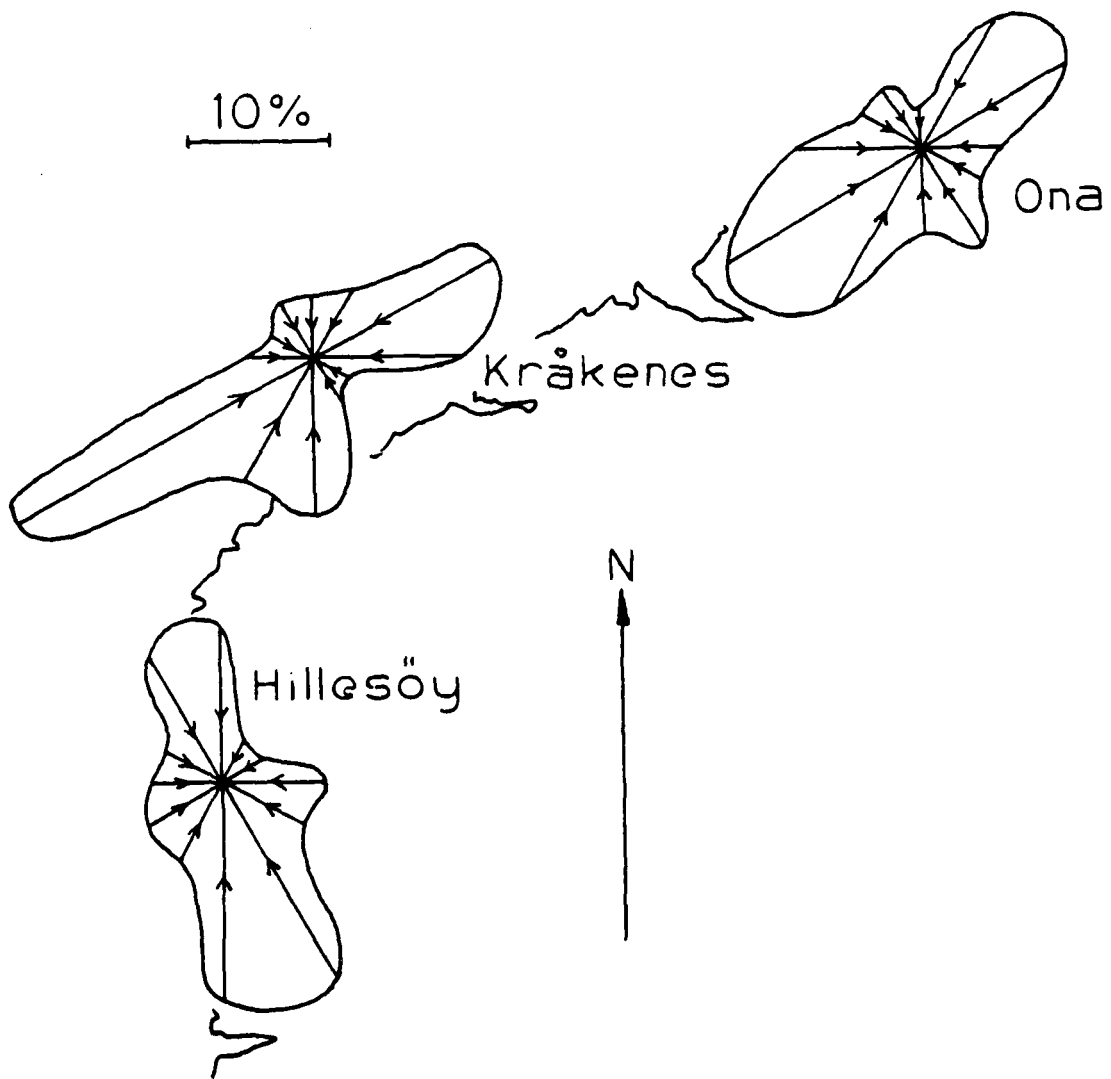


Fig. 12. Frequencies of Wind Directions in Percent for Stations Along the Coast from "Hillesøy" to "Ona."

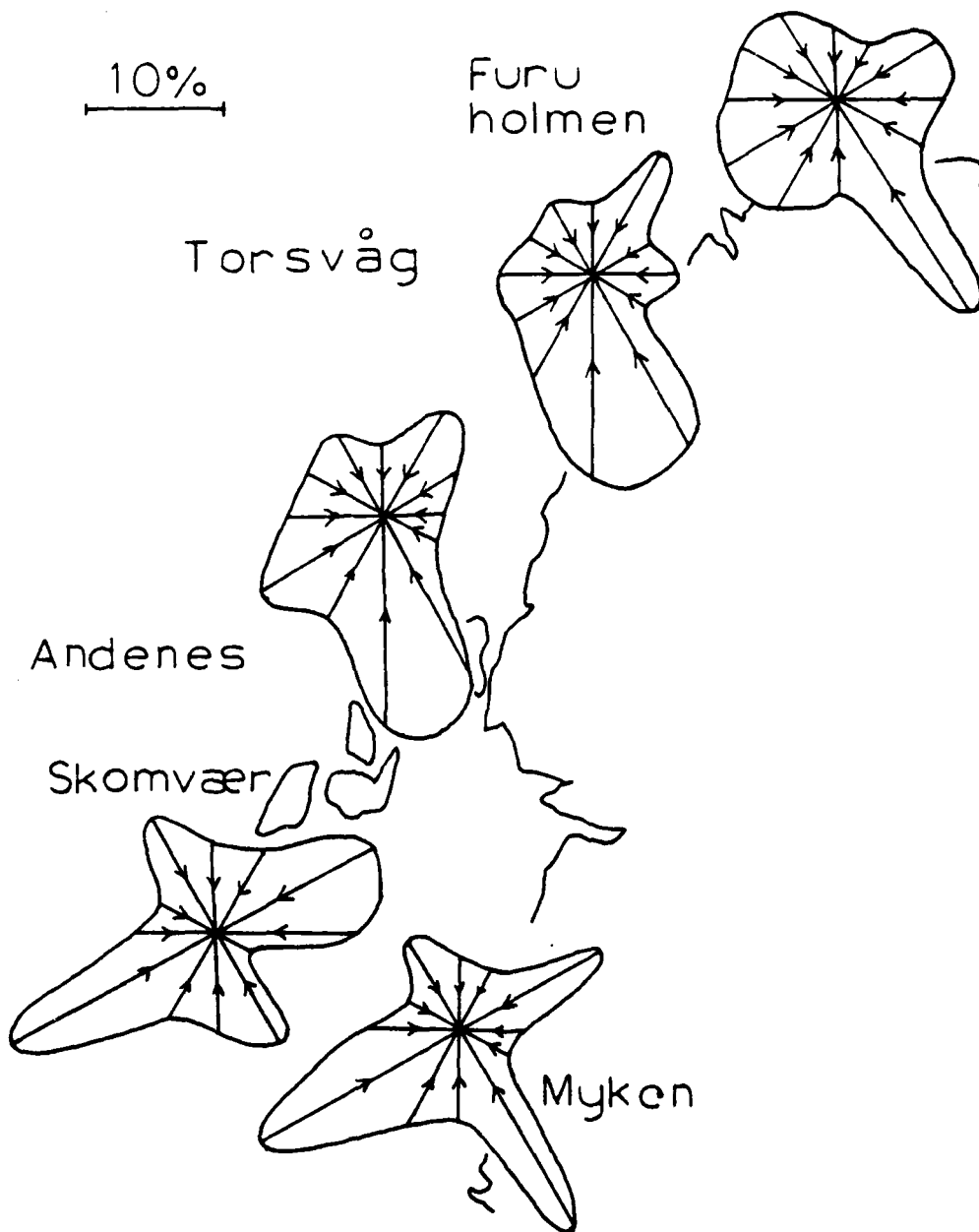


Fig. 13. Frequencies of Wind Directions in Percent for Stations Along the Coast from "Myken" to "Furuholmen."

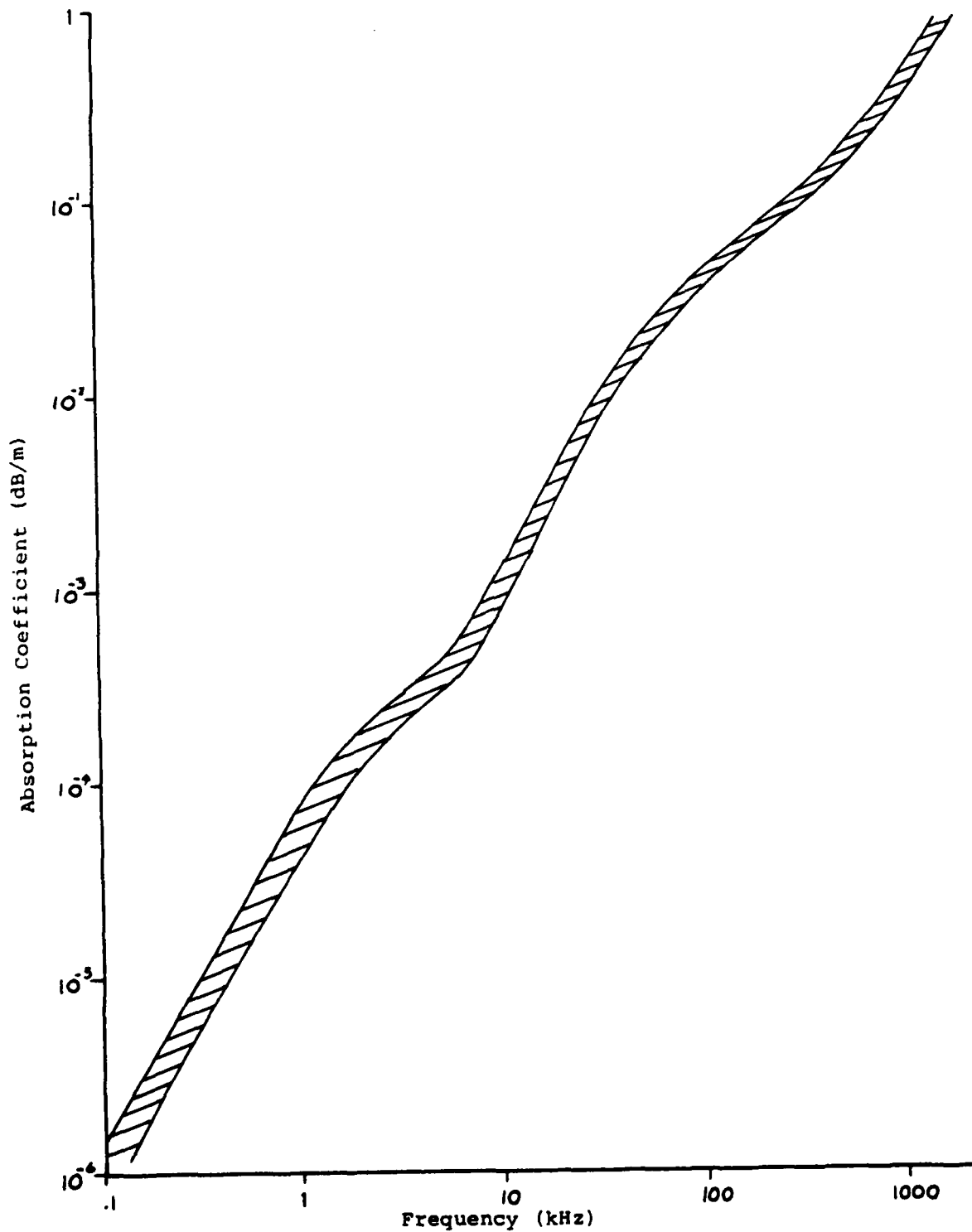


Fig. 14. Absorption Coefficient in dB/m as a Function of Frequency.

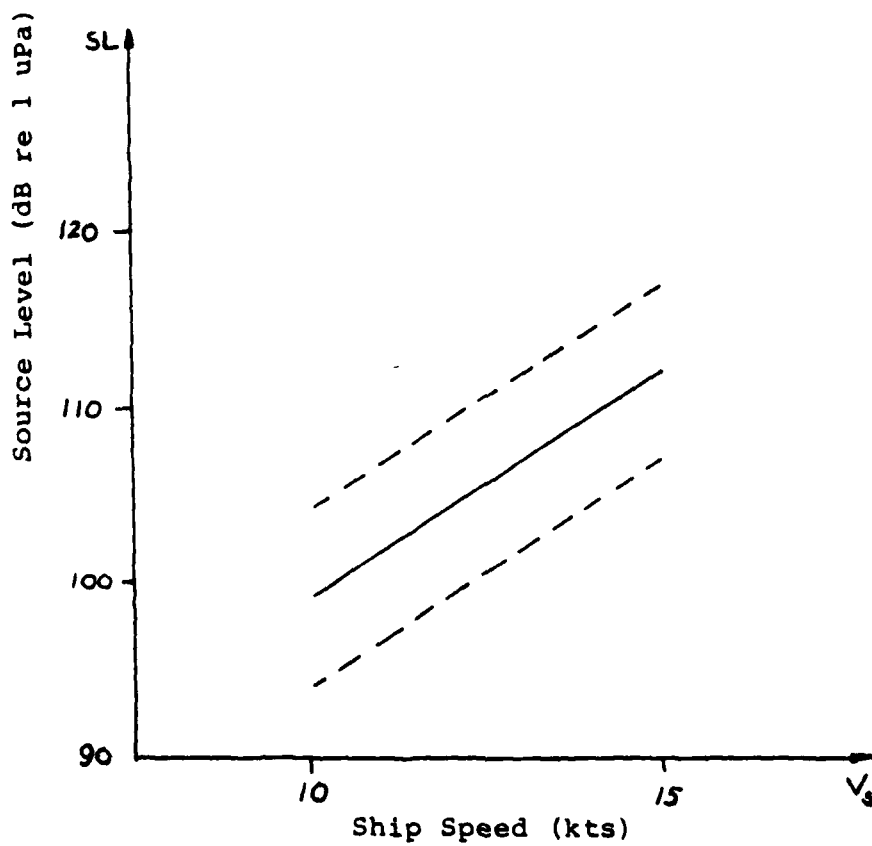


Fig. 15. Average Radiated Spectrum Level for Surface Ship as a Function of Speed in kts.

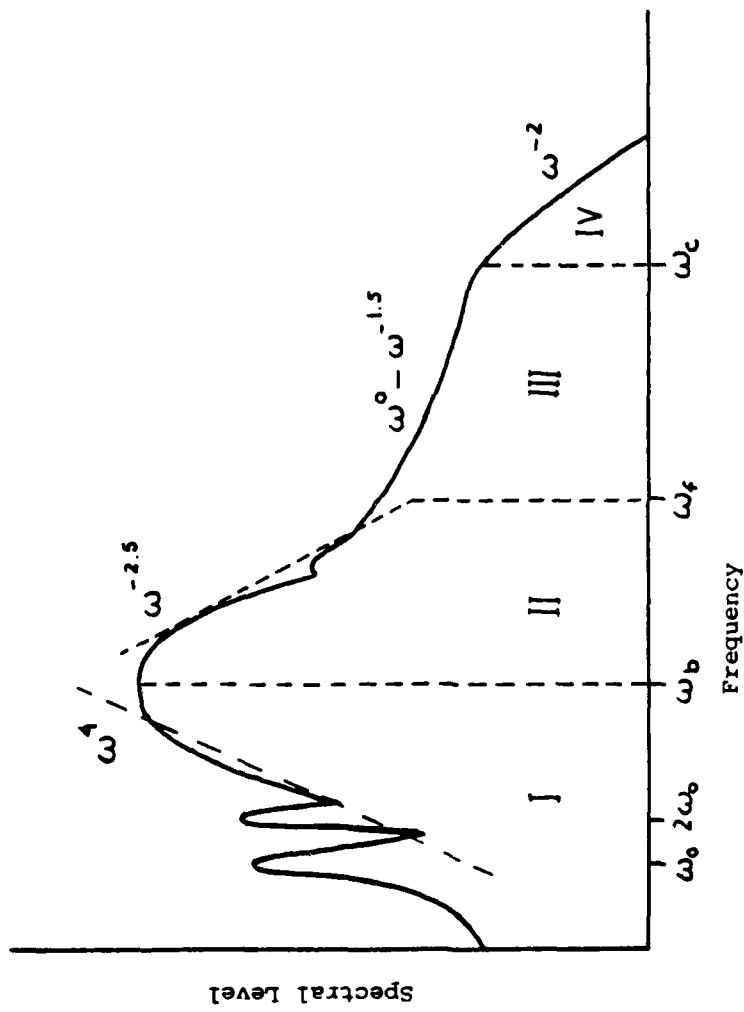


Fig. 16. General Noise Spectrum for a Cavitating Propeller.

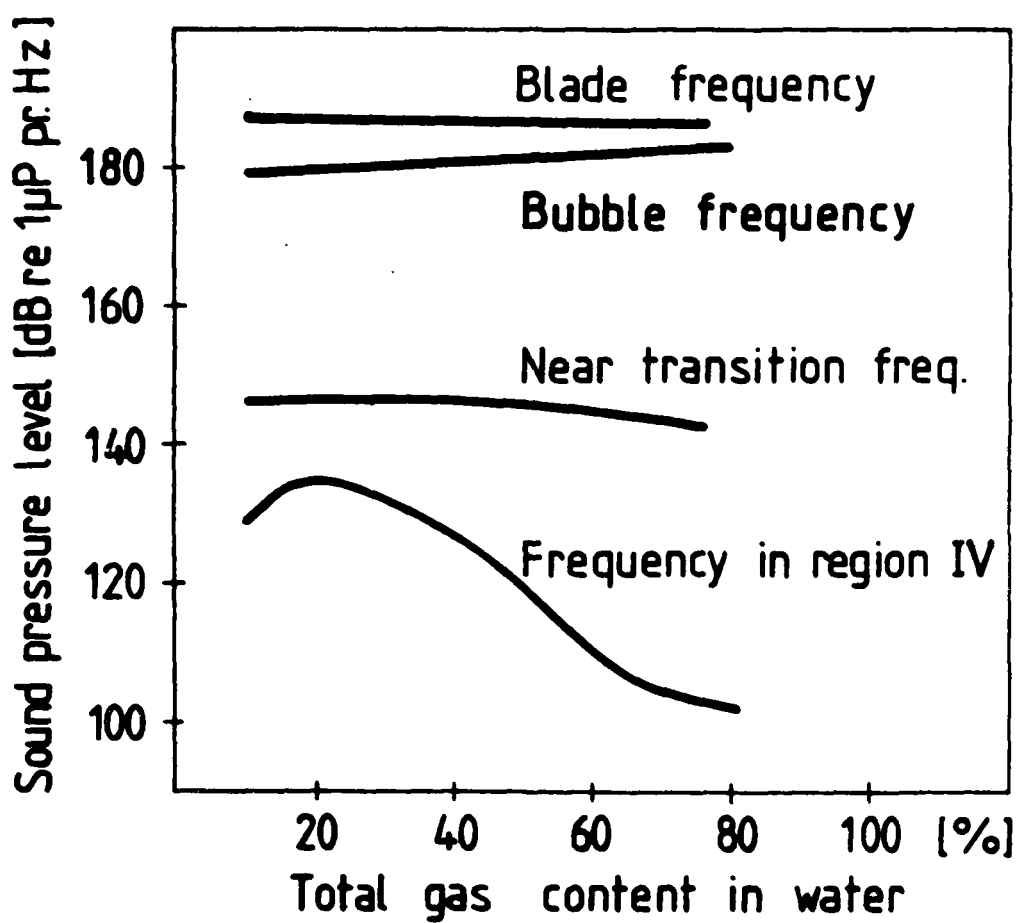


Fig. 17. Spectrum Level as a Function of Total Gas Content

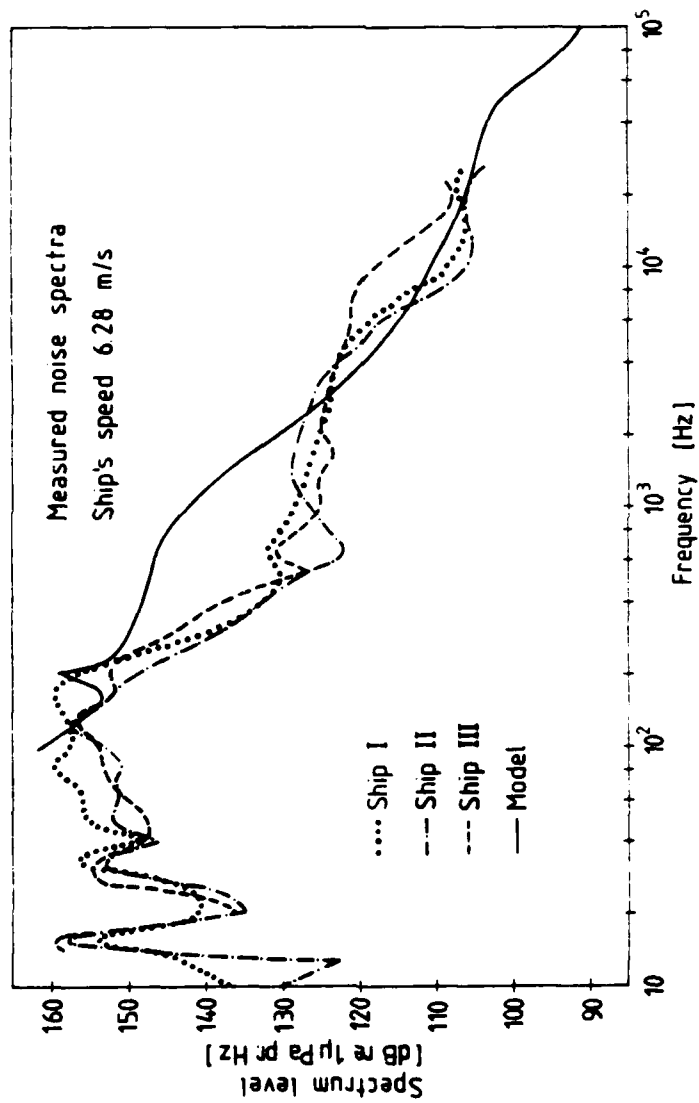


Fig. 18. Measured Model and Full Scale Noise Spectra.

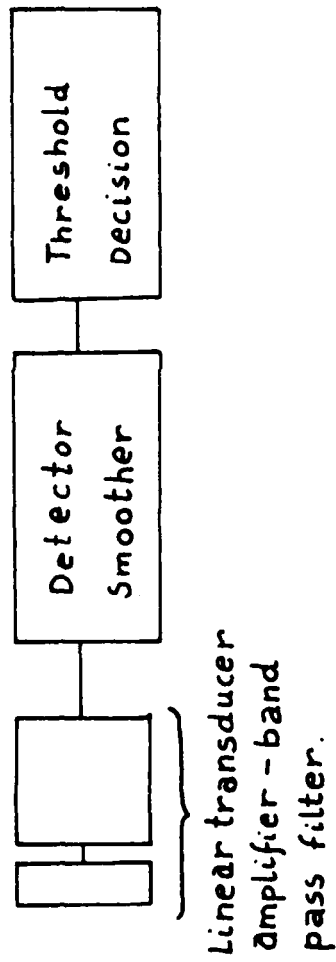


Fig. 19. Square Law Detector Scheme.

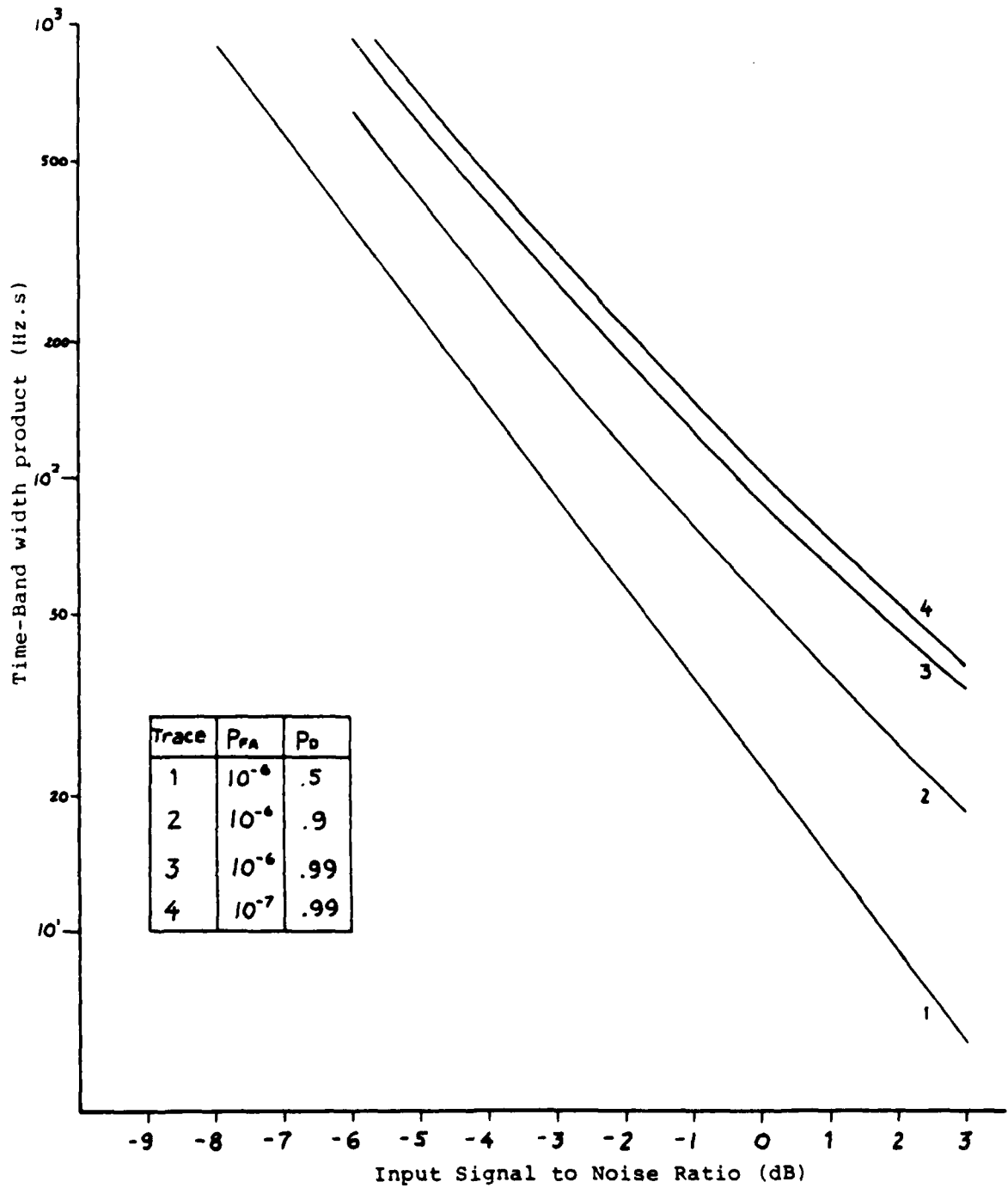


Fig. 20. Required Input S/N Ratio and BT Product for Various Operating Probabilities.

Trace	Threshold above NL	P_{FA}
1	.88	10^{-6}
2	1.0	2×10^{-8}
3	1.5	1×10^{-10}
4	2.0	1×10^{-30}
5	2.5	1×10^{-24}
6	3.0	1×10^{-28}

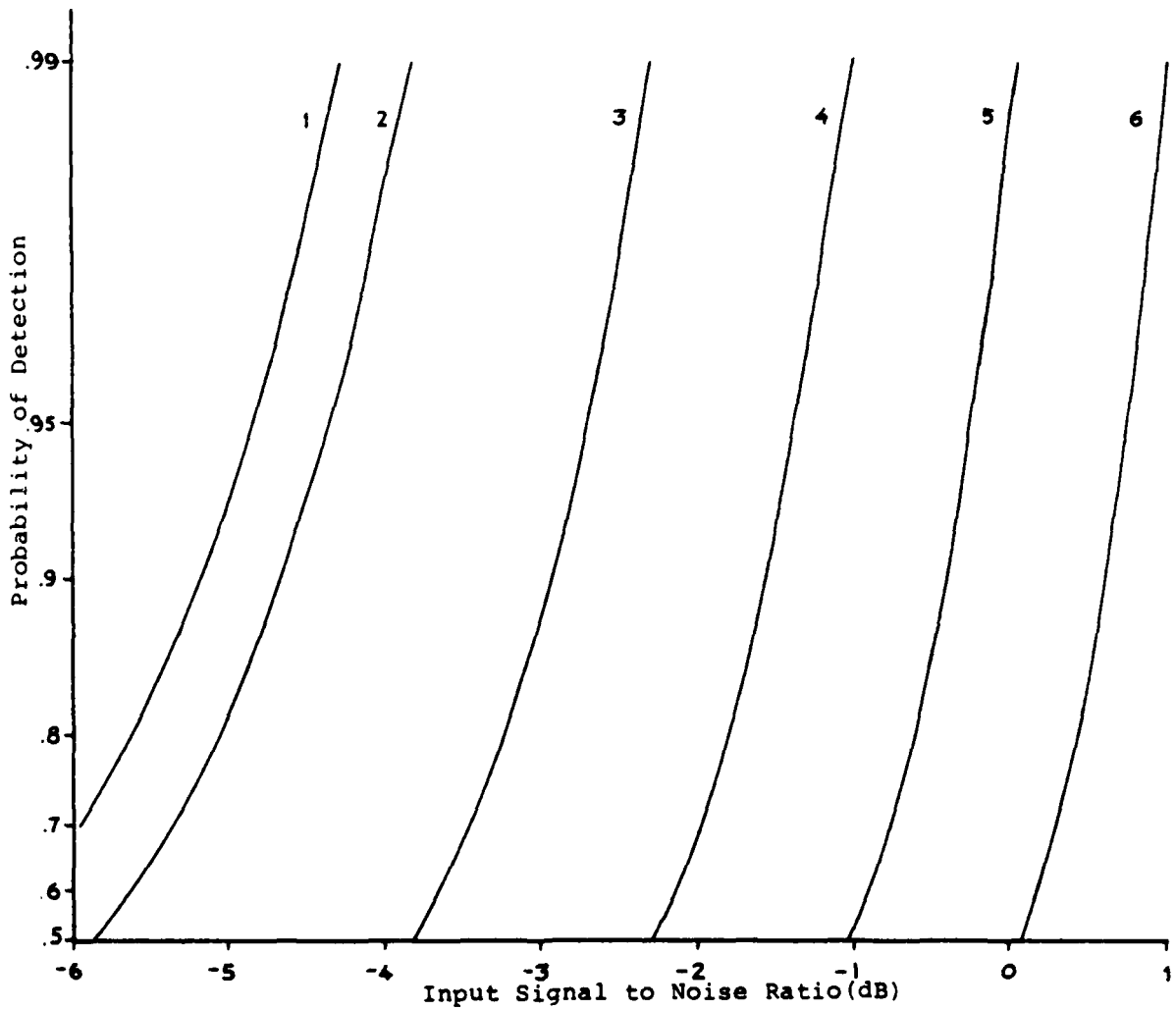


Fig. 21. Probability of Detection Versus Input S/N Ratio for Various Thresholds.

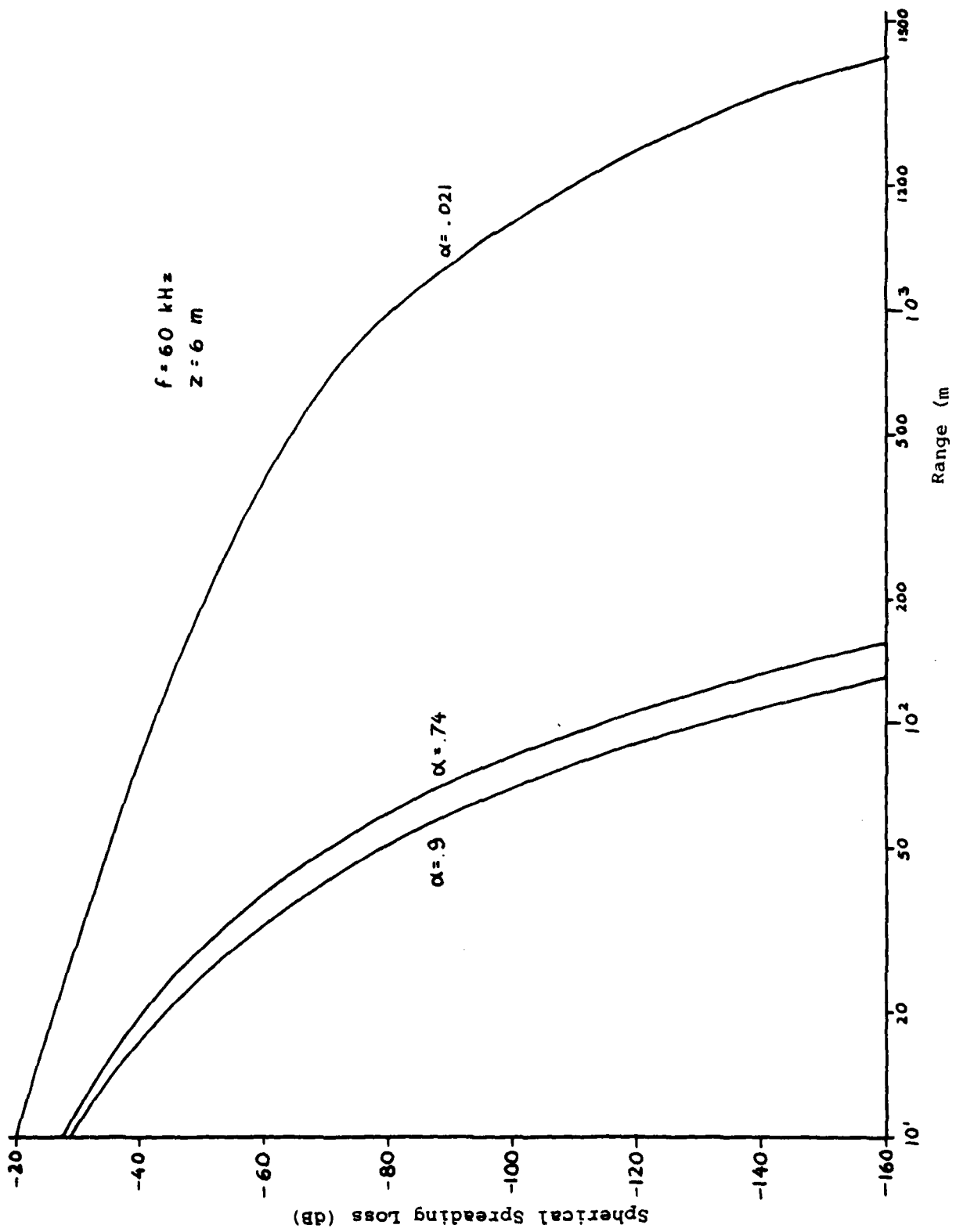


Fig. 22. $-20\log R - \alpha R$ Versus R for Frequency of 60 kHz.

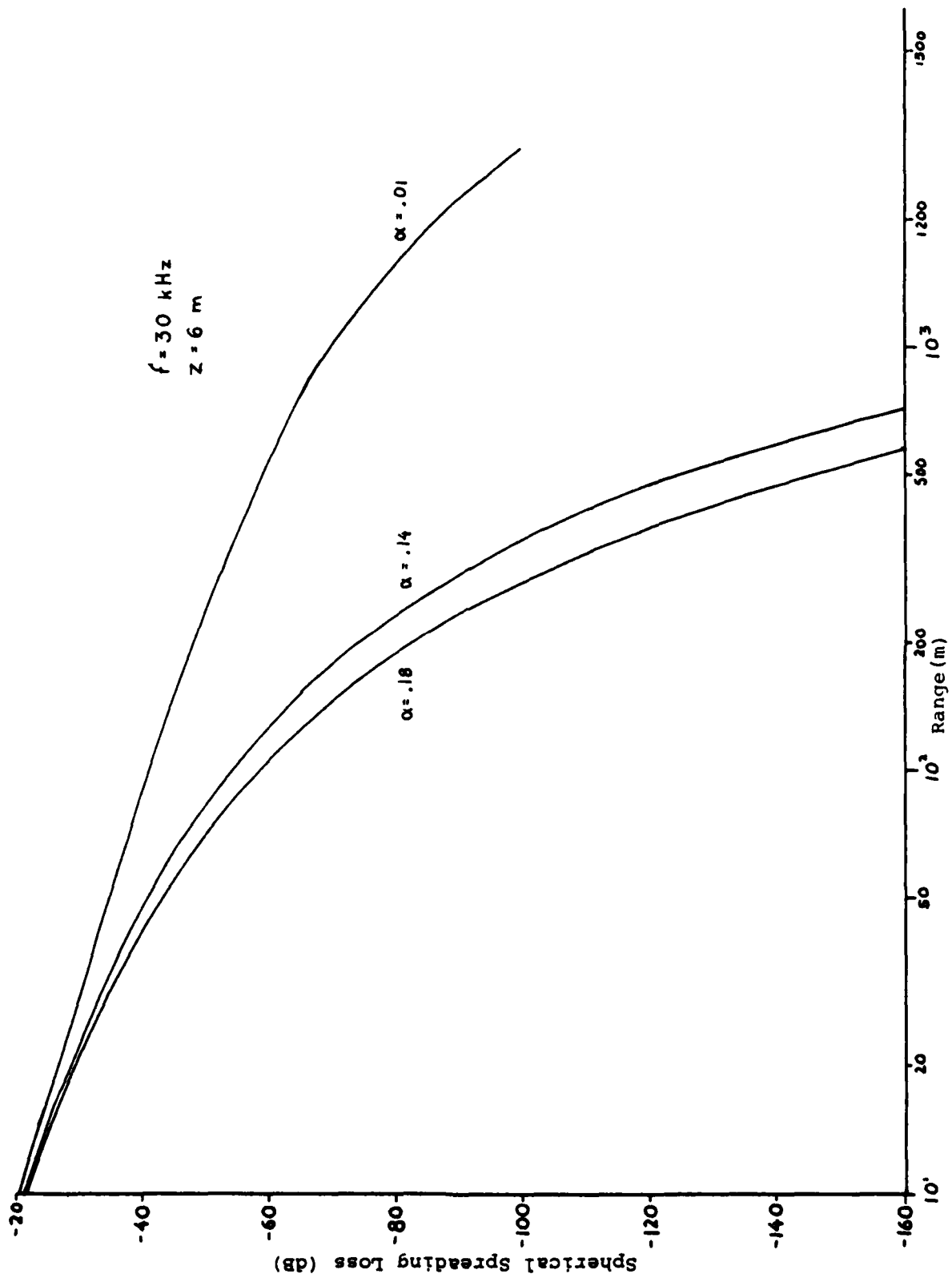


Fig. 23. $-20\log R - \alpha R$ Versus R for a Frequency of 30 kHz.

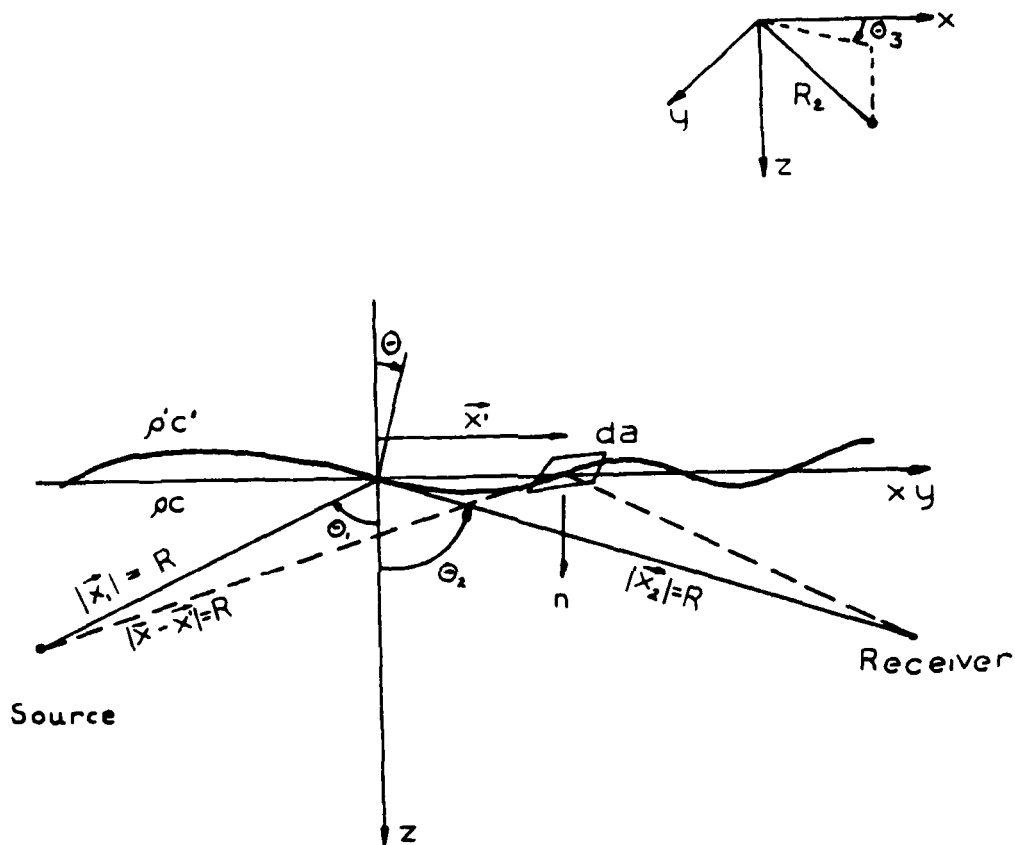


Fig. 24a. Geometry at the Sea Surface Scattering.

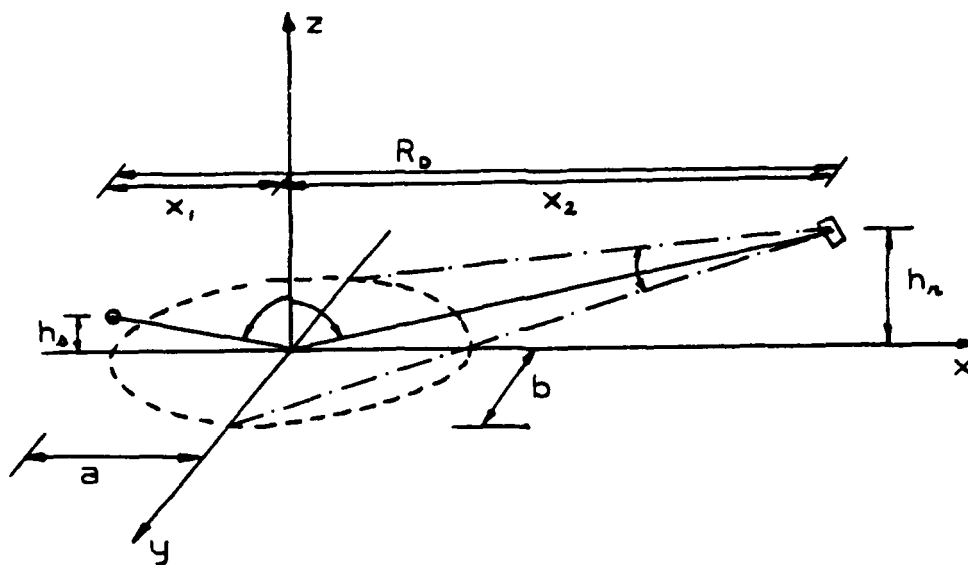


Fig. 24b. Specular Scattering Geometry.

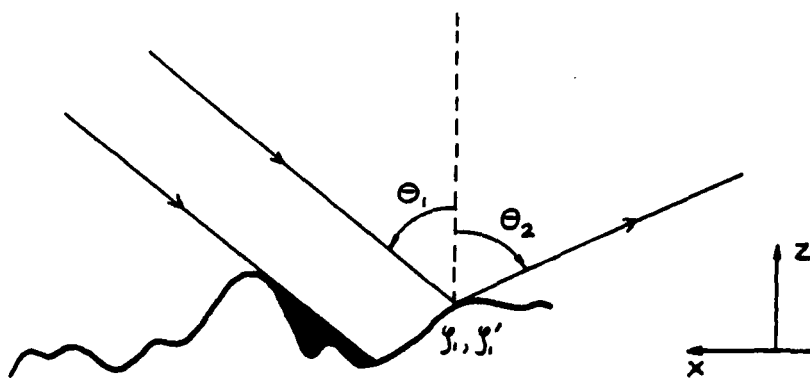


Fig. 25. Rough Surface Shadowing Geometry.

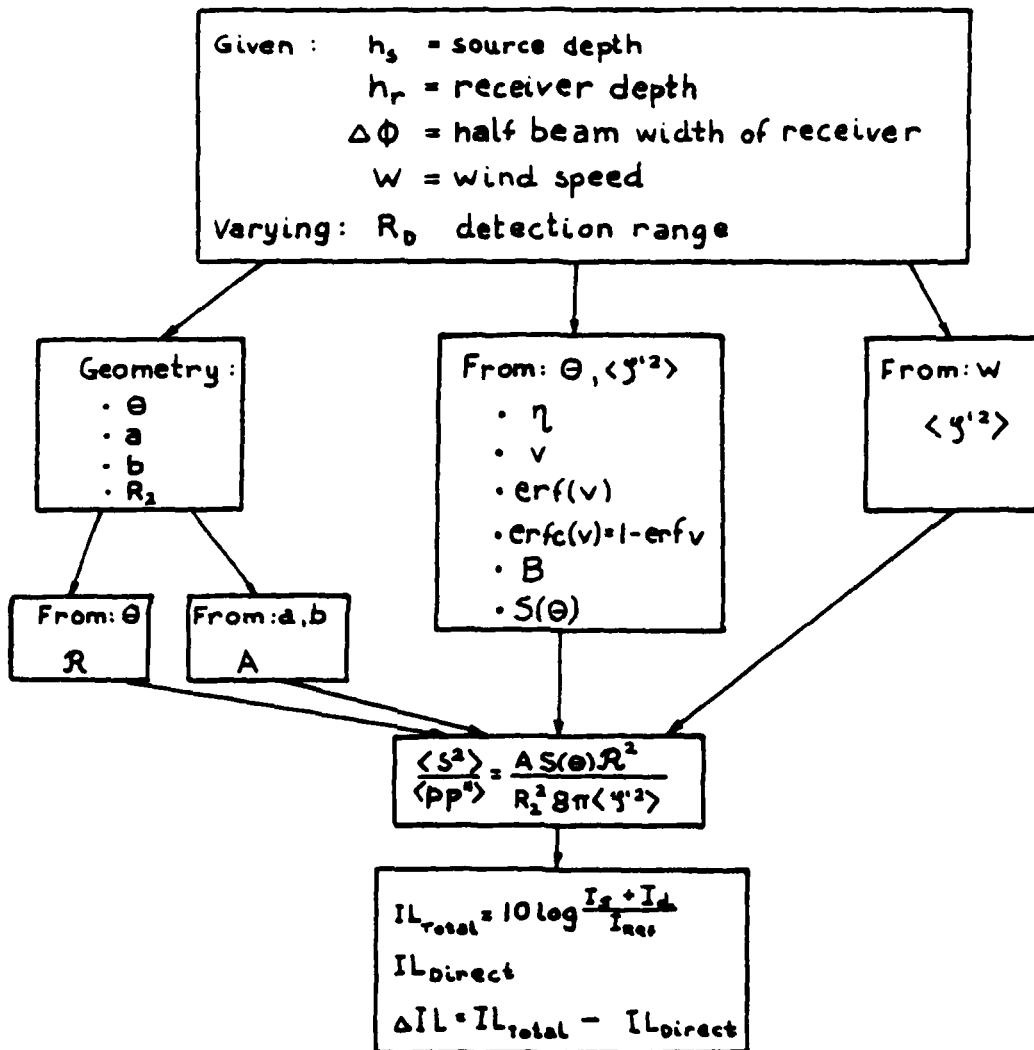


Fig. 26. Calculation Scheme of the Surface Scattering Effect.

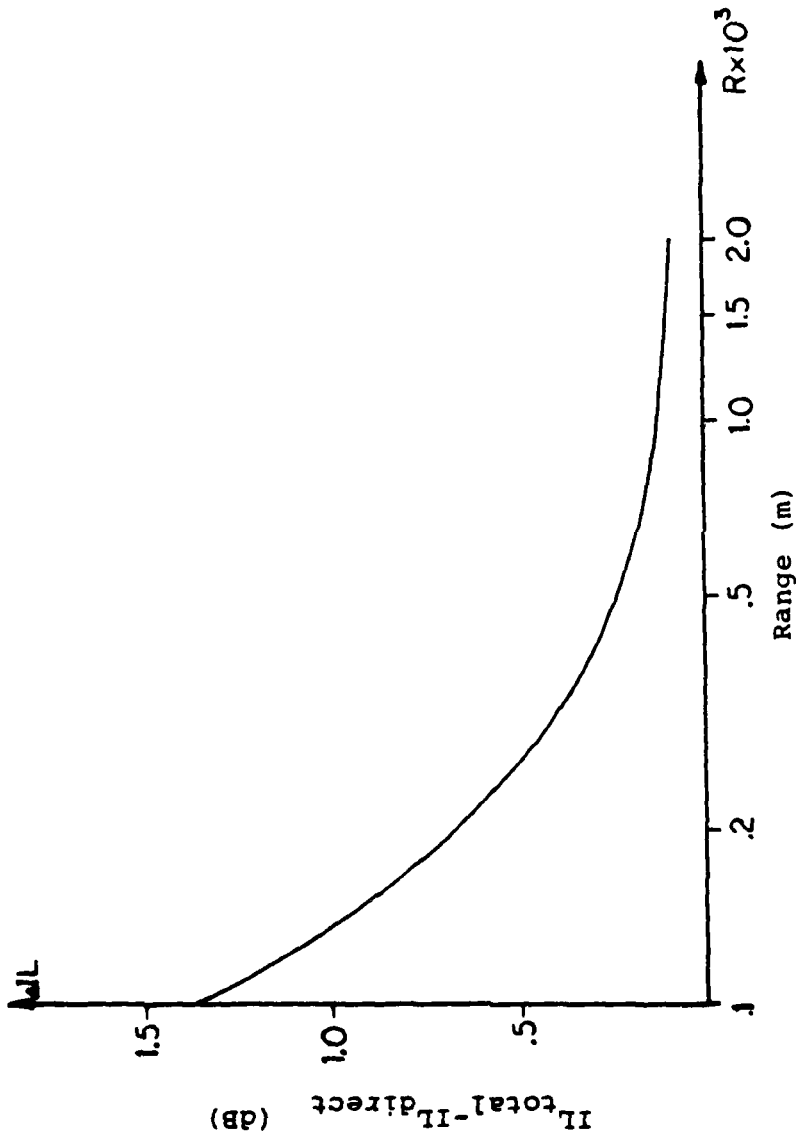


Fig. 27. ΔIL Versus R.

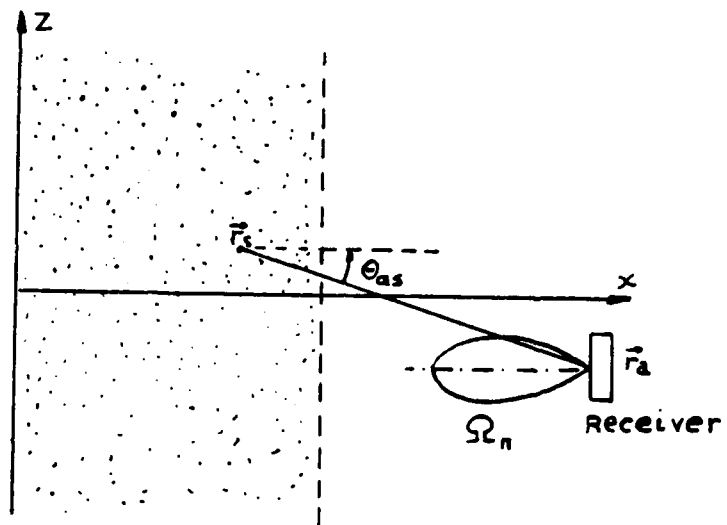


Fig. 28. Geometry of the Subsurface Propagation Model.

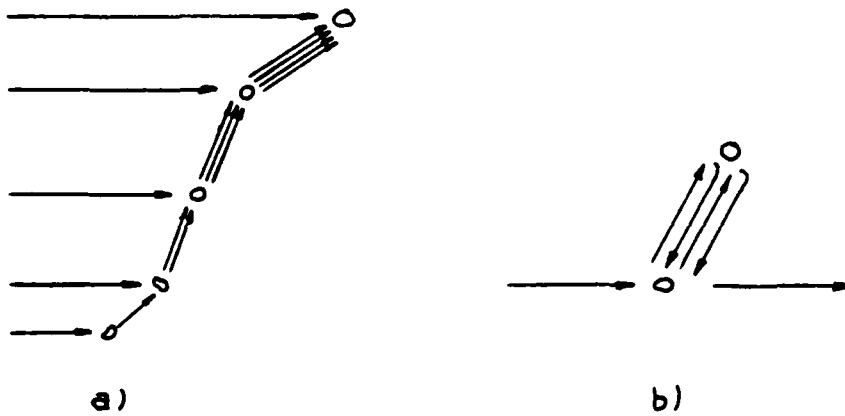


Fig. 29. a) Chains of Successive Scattering.
 b) Scattering Pattern Going Through the Same Scatterer More than Once.

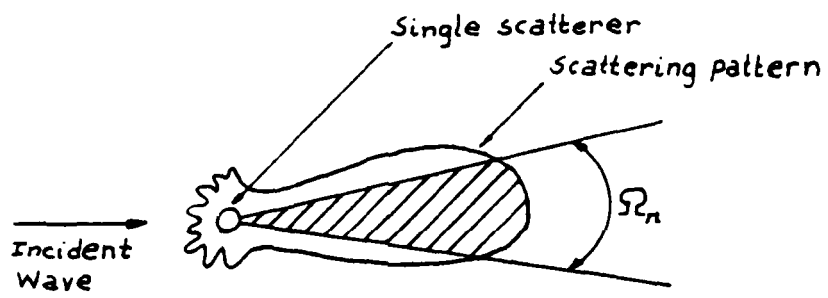


Fig. 30. Scattering Pattern.

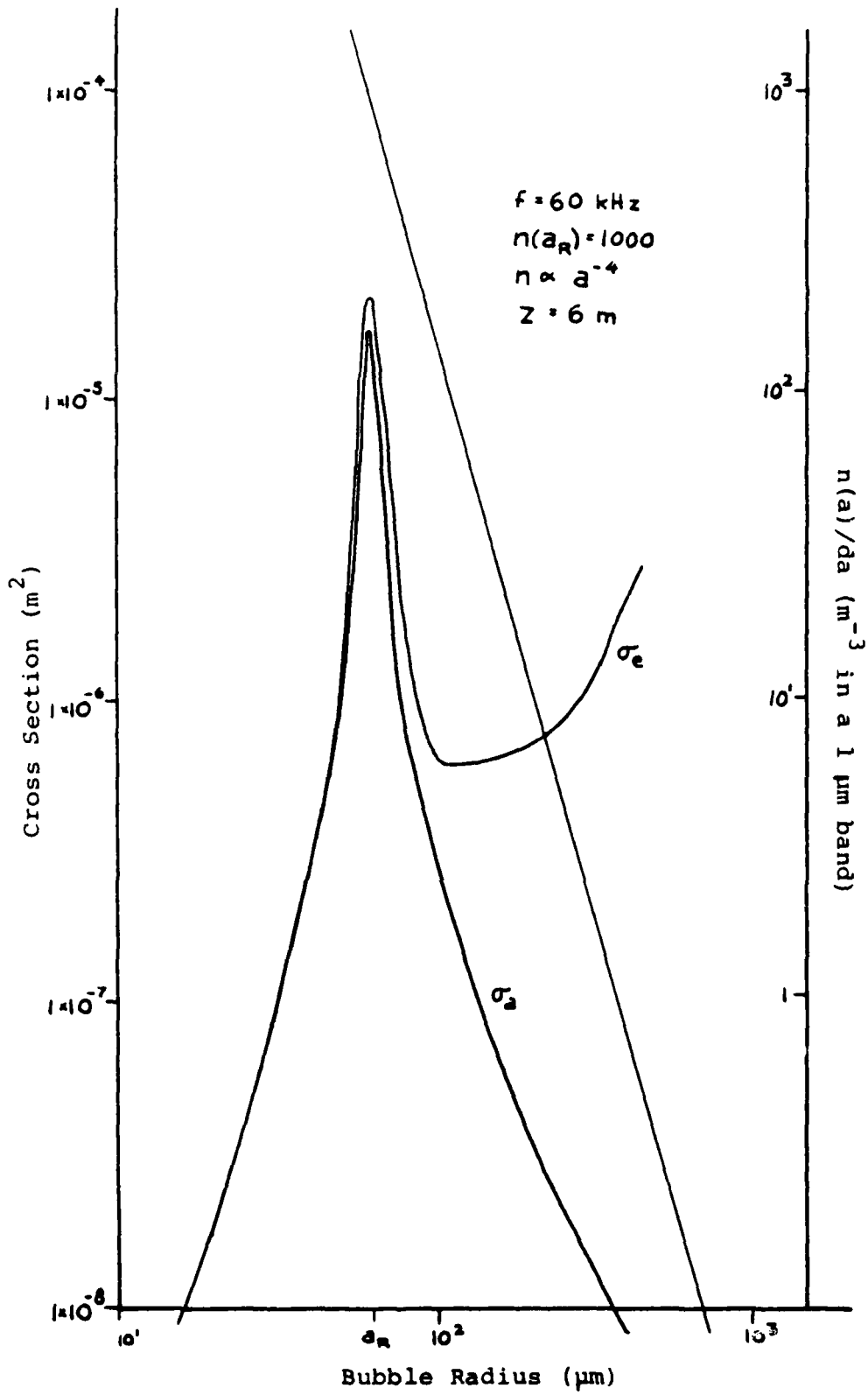


Fig. 31. σ_e and σ_a for 60 kHz.

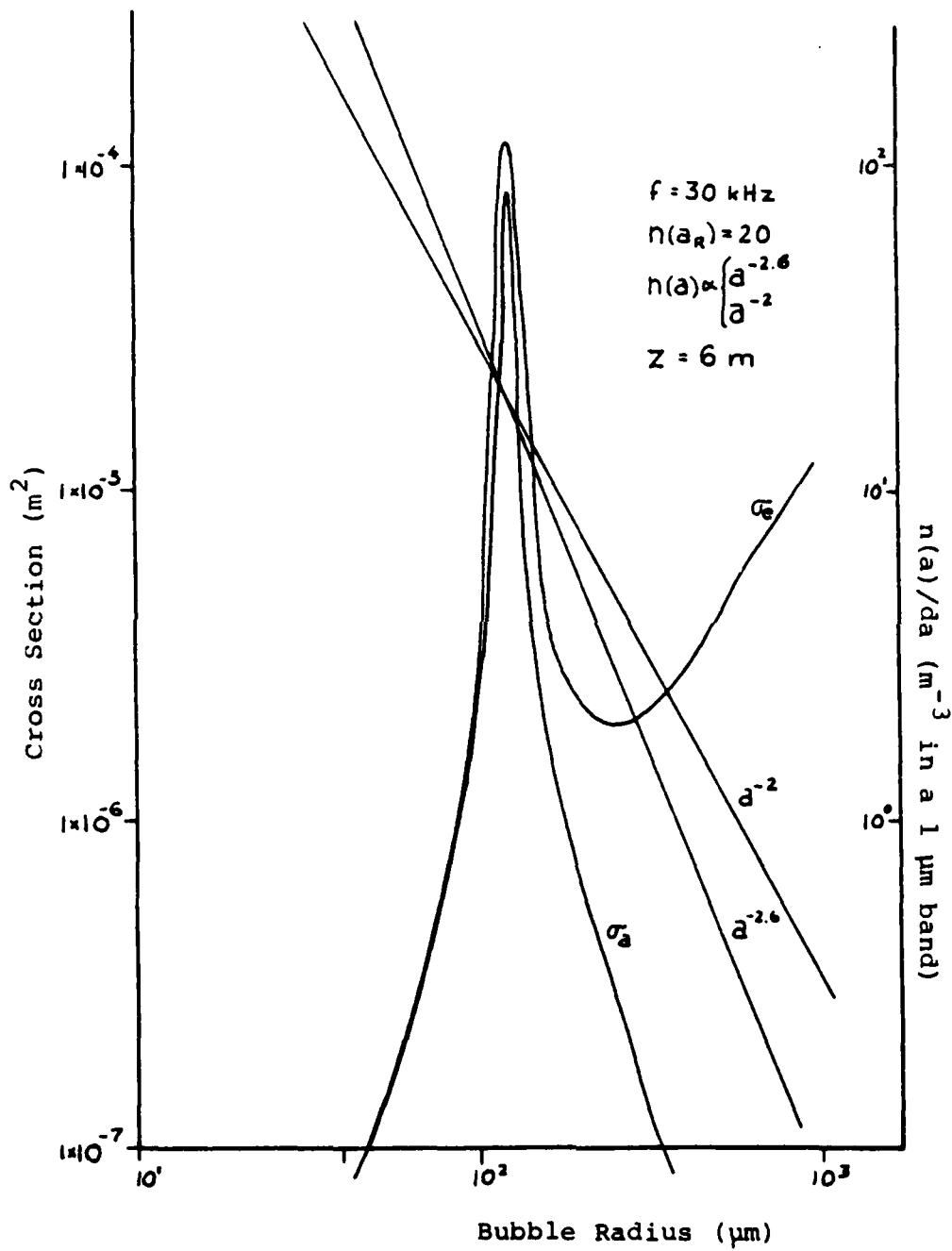


Fig. 32. σ_e and σ_a for 30 kHz.

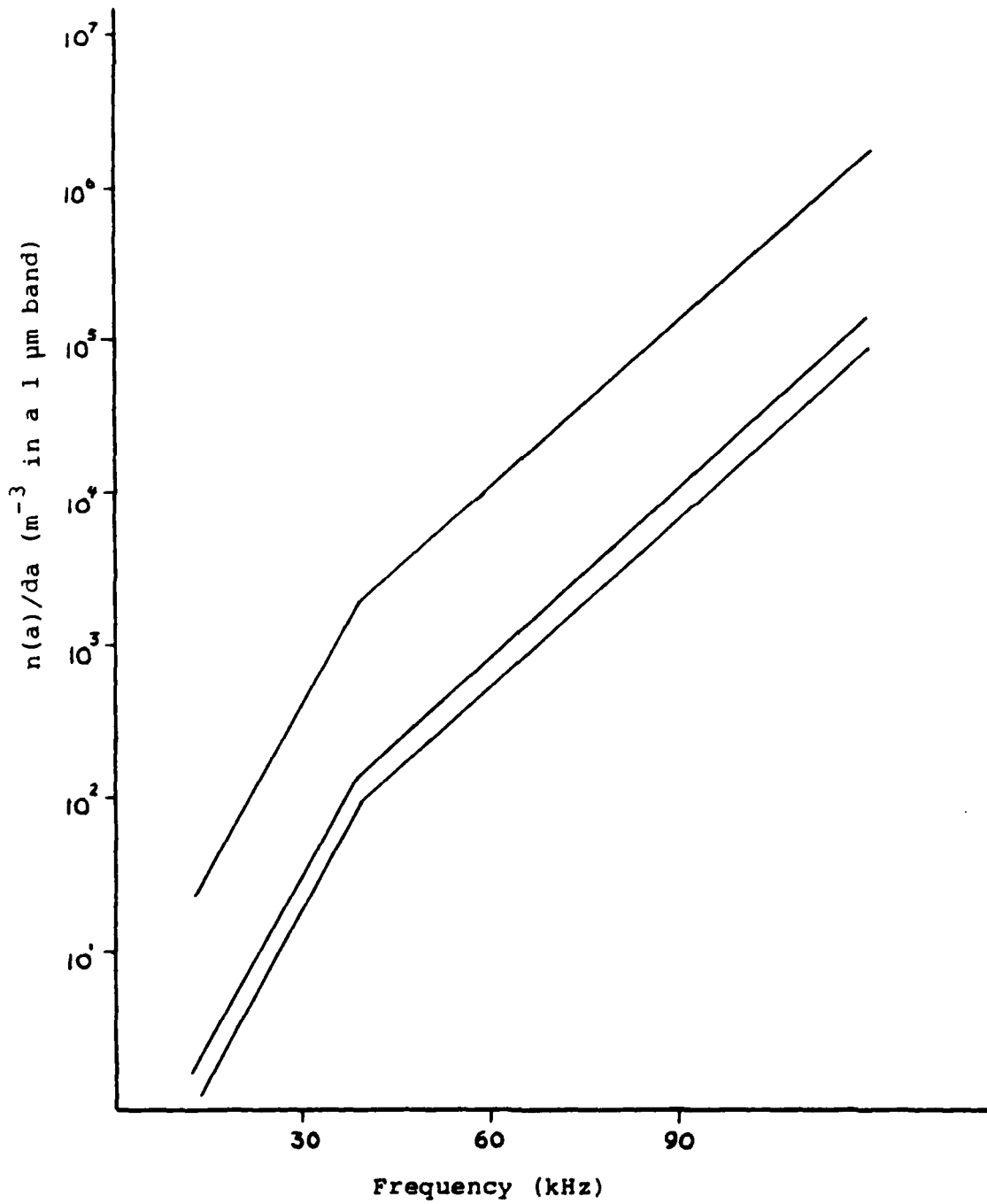


Fig. 33. Interpolated Bubble Data.

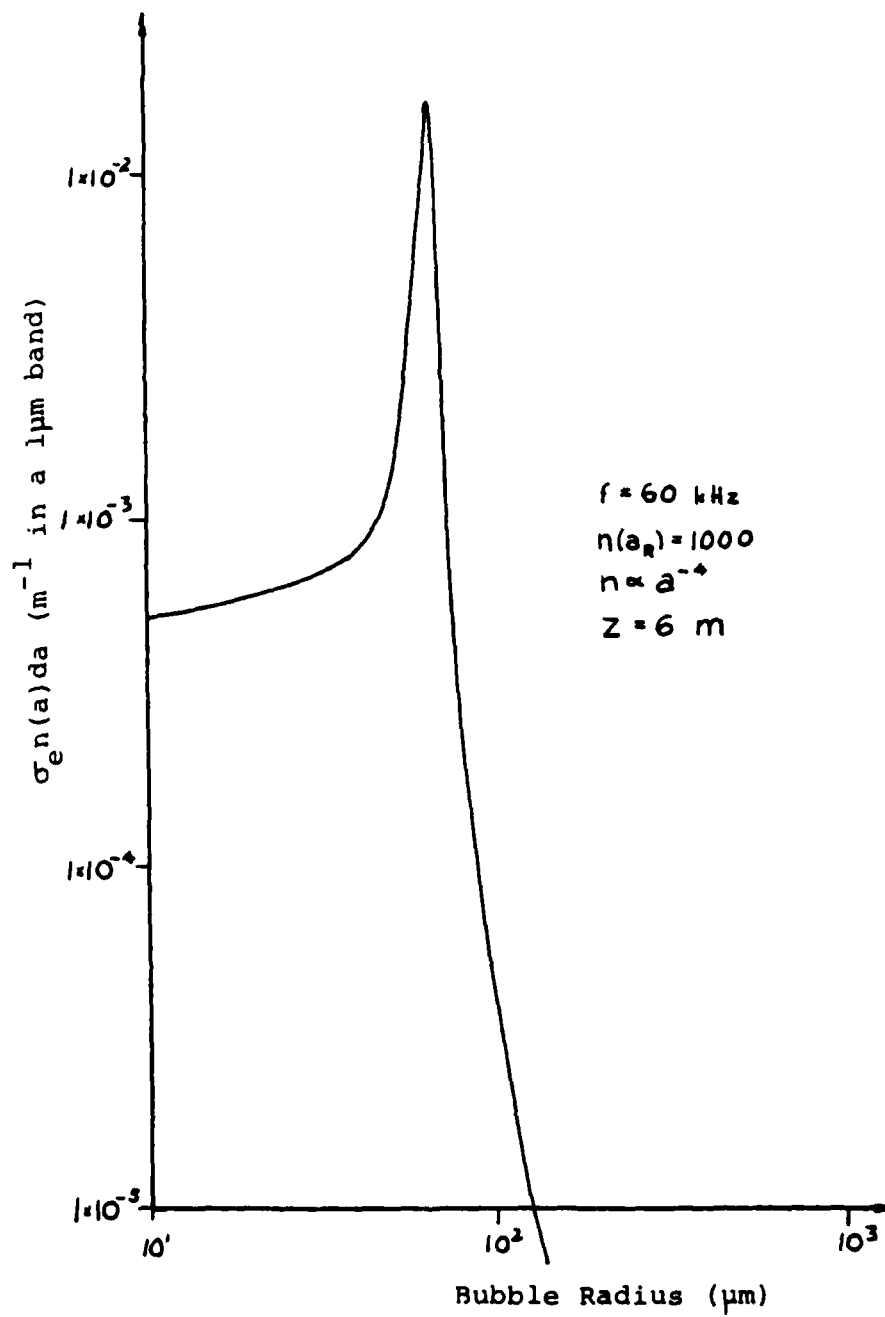


Fig. 34. $\sigma_e(a)n(a)da$ for 60 kHz.

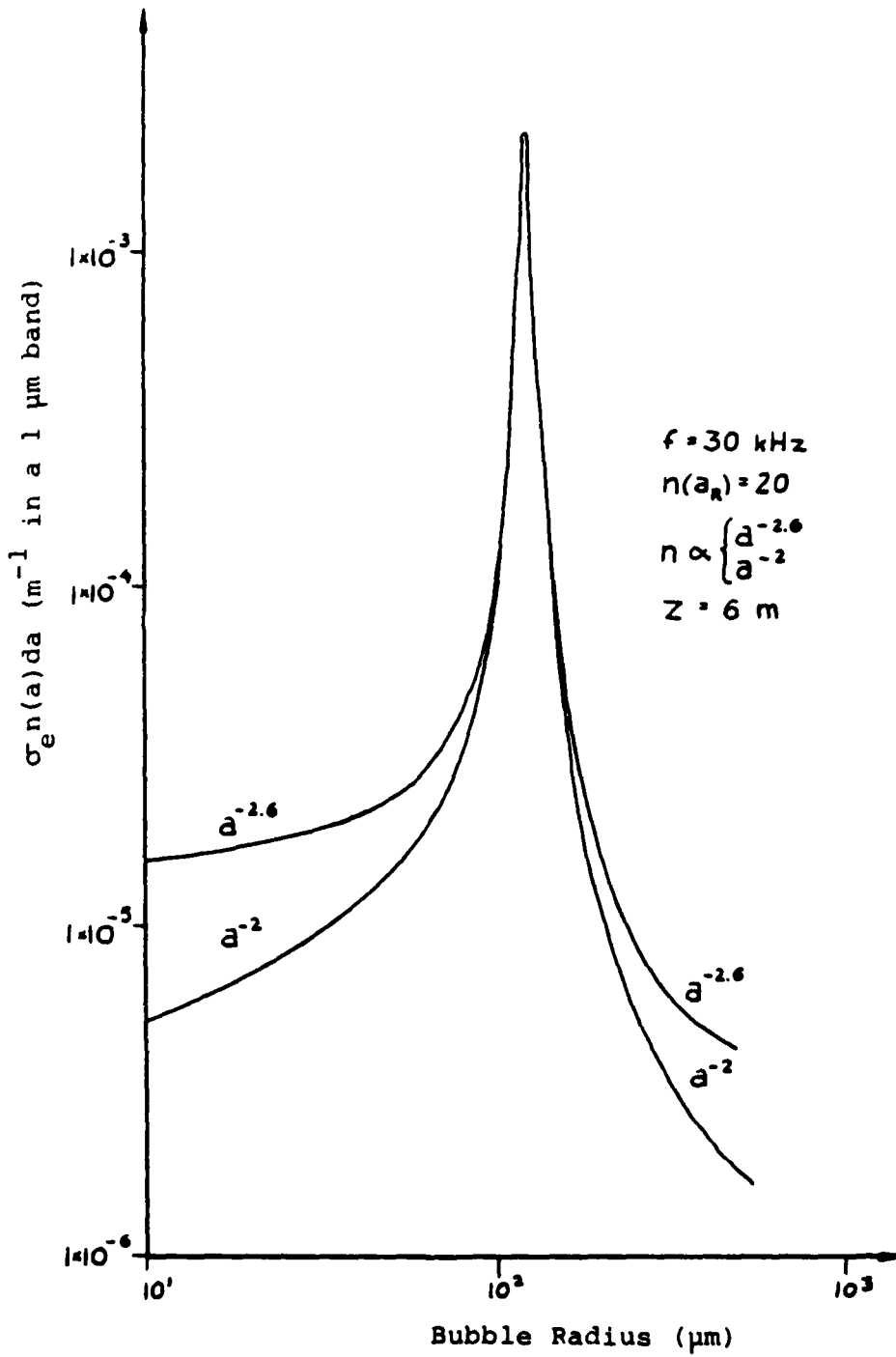


Fig. 35. $\sigma_e(a)n(a)da$ for 30 kHz.

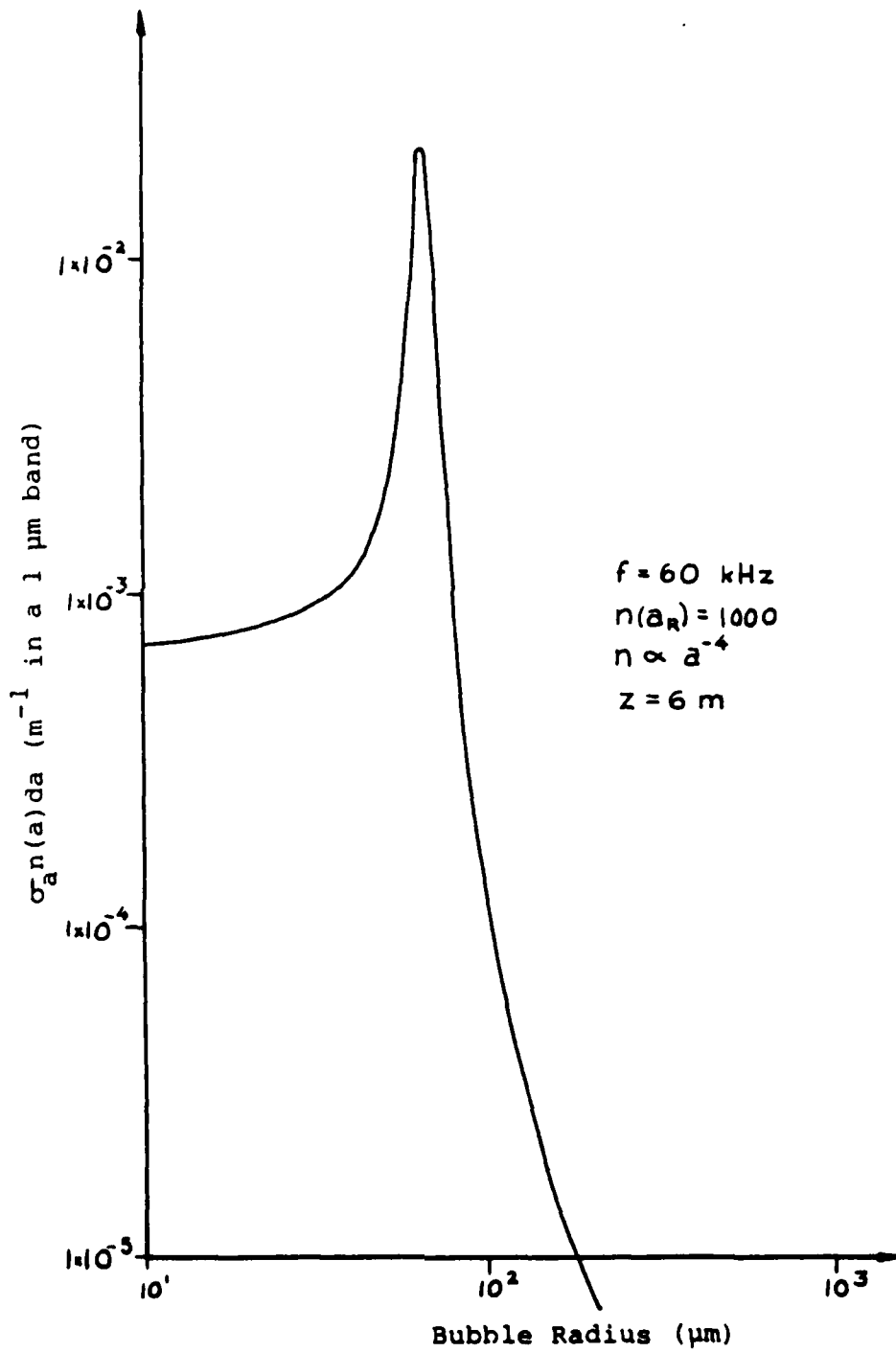


Fig. 36. $\sigma_a(a)n(a)da$ for 60 kHz.

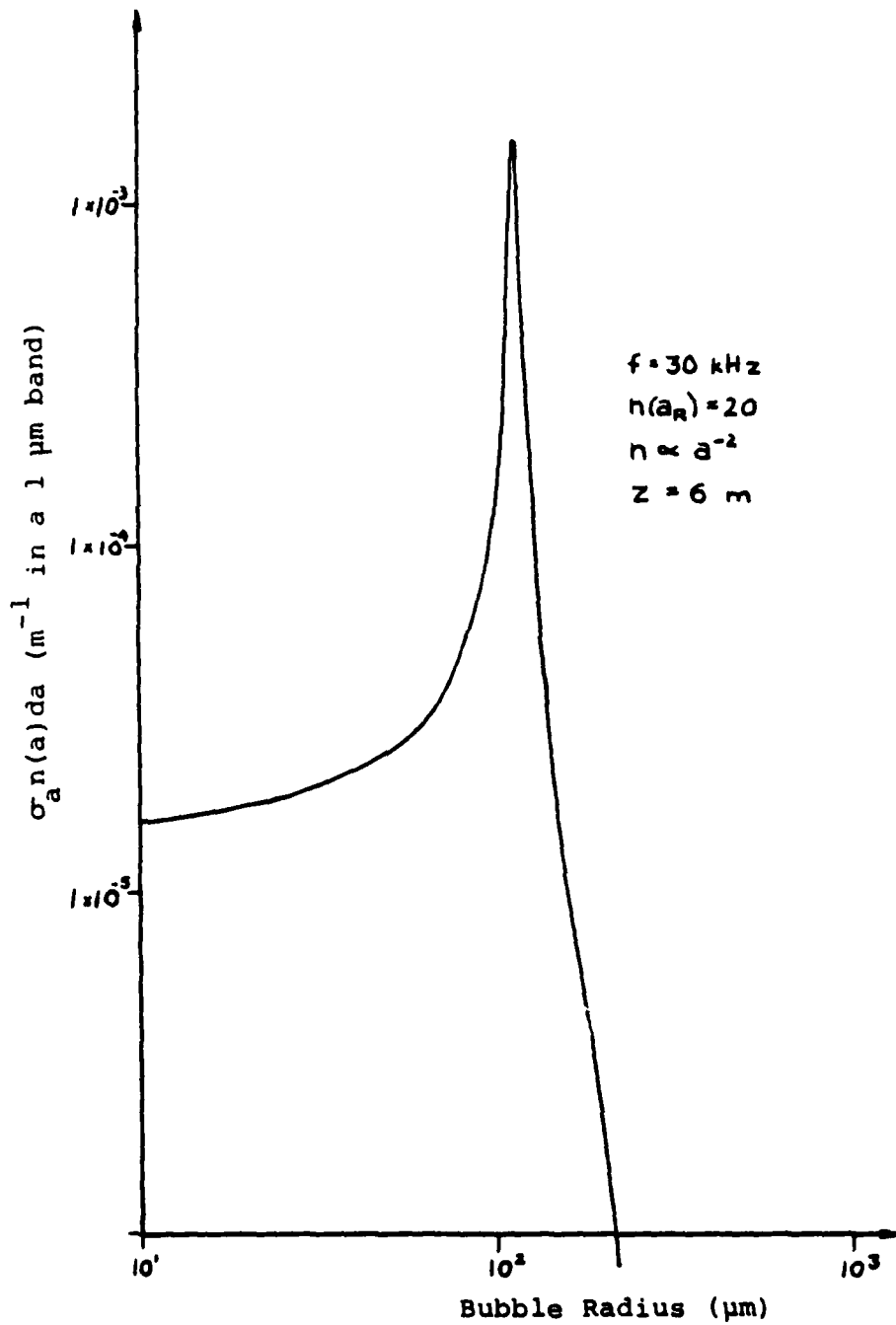


Fig. 37. $\sigma_a(a)n(a)da$ for 30 kHz.

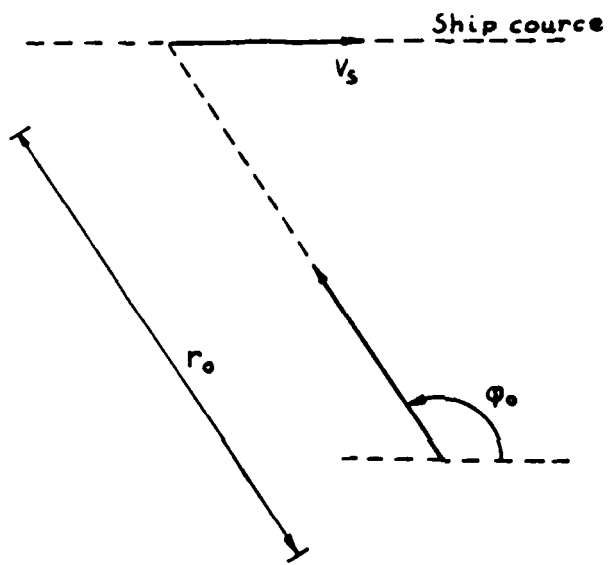


Fig. 38. Pursuit Homing Geometry.

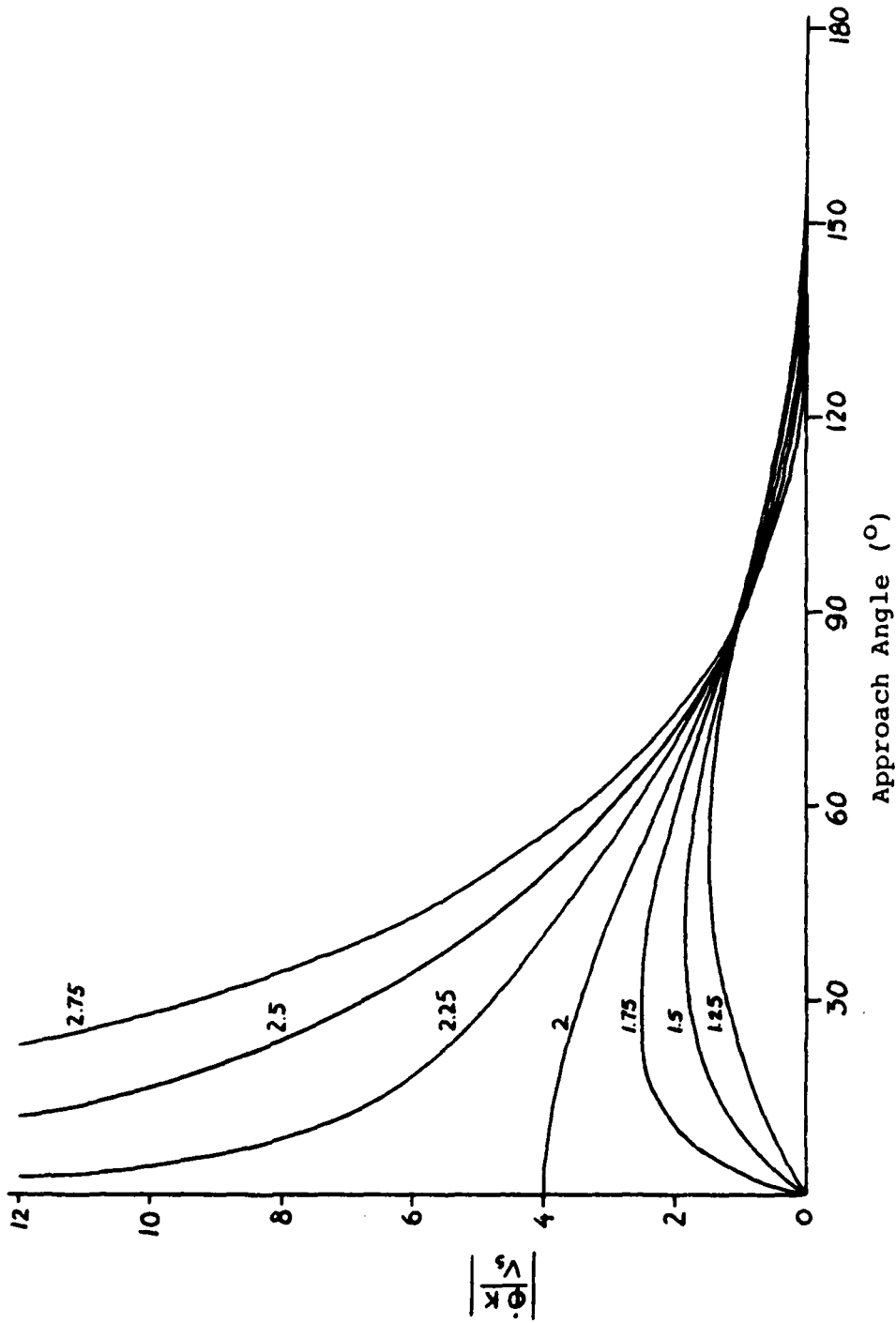


Fig. 39. $\left| \frac{\phi K}{V_s} \right|$ as a Function of ϕ With Parameter p.

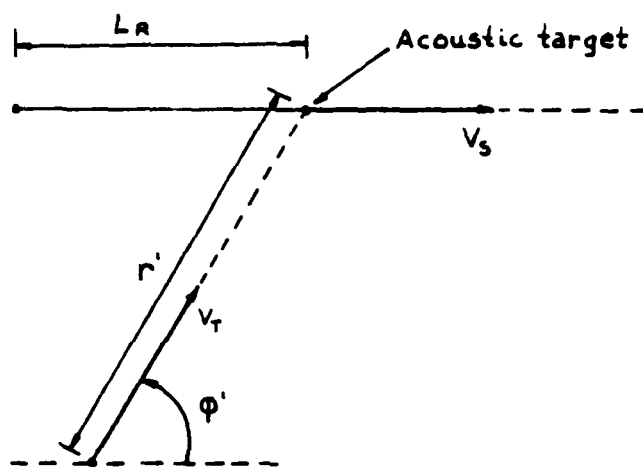


Fig. 40. Hit Criterion Geometry.

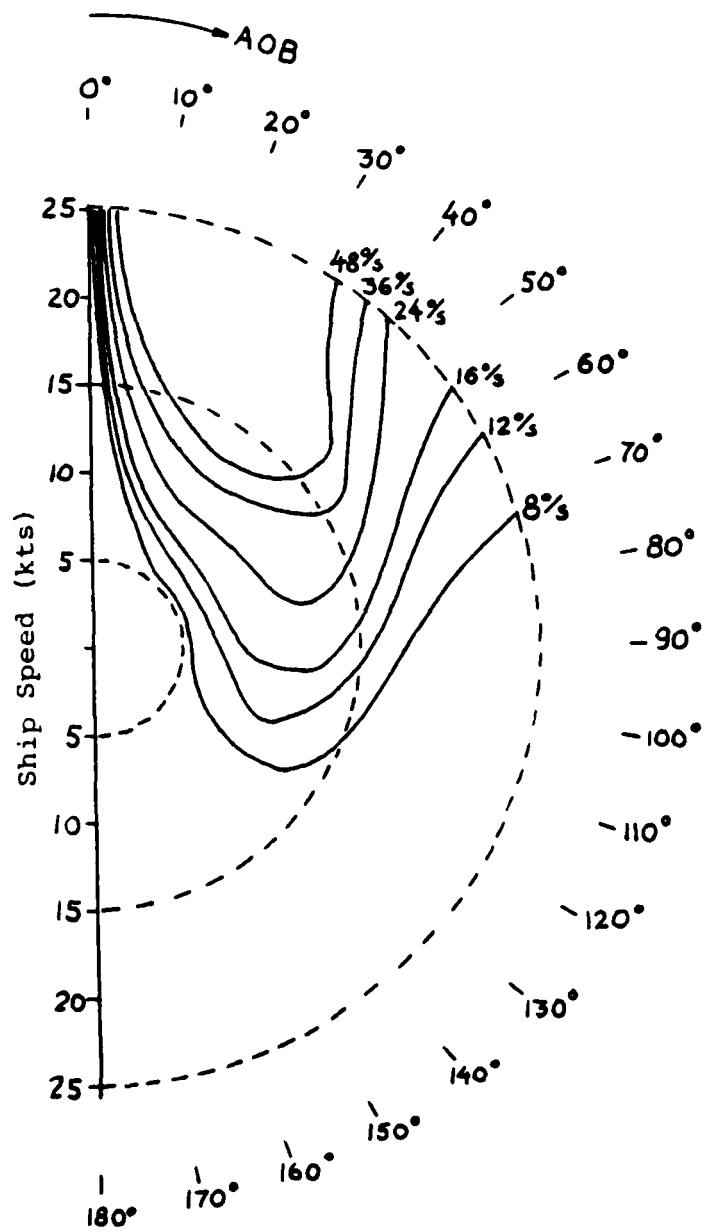


Fig. 41. AOB-limitation Versus Ship Speed with Parameter Maximum Turn Rate.

LIST OF REFERENCES

1. IKU (Continental Shelf Institute, Norway), Bølgedata fra Kontinentalsokkelen (translated, Wave Data from the Continental Shelf), IK U B 772/77/TA/mg, October 1977.
2. Lövik, A., Akustisk Måling av Vind og Bølgeinduserte Gassbobler i Havet (translated, Acoustic Measurements of Wind and Wave Induced Air Bubbles in the Ocean), NTH ELAB Report STF 44A7914, pp. 15-16, May 1979.
3. Medwin, H., In Situ Acoustic Measurements of Bubble Populations in Coastal Waters, J. Geoph. Res., V. 75, pp. 599-611, 1971.
4. Wenz, G. M., Acoustic Ambient Noise in the Ocean Spectra and Sources, J.A.S.A., V. 34, pp. 1936-1956, 1962.
5. Norwegian Defence Research Establishment, Division for Underwater Warfare, Typical Sound Velocity Curves in Norwegian Coastal Waters.
6. U.S. Navy, N.O. Publication 700, 1969.
7. Urick, R. J., Principles of Underwater Sound, McGraw-Hill, 1975.
8. Thorp, W. H., Deep Ocean Sound Attenuation in the Sub- and Low-Kilocycle-per-Second Region, J.A.S.A., V. 38, pp. 648-654, 1965.
9. Ross, D., Mechanics of Underwater Sound, Pergamon Press, 1976.
10. Morse, P. M. and Ingard, K. V., Theoretical Acoustics, McGraw-Hill, 1968.
11. Lövik, A., A Theoretical and Experimental Investigation on Propeller Cavitation Noise, NTH ELAB Report STF 44A80121, February 1980.
12. Lövik, A., Acoustic Detection of Gas Bubbles in Water, NTH ELAB Report STF 44A80122, pp. 25-38, February 1980.
13. Cox, C. S., and Munk, W. H., Measurements of the Roughness of the Sea Surface from Photographs of the Sun's Glitter, J. Optic, Soc. Am., V. 44, pp. 838-850, 1954.
Cox, C. S., and Munk, W. H., Statistics of the Sea Surface Derived from the Sun Glitter, J. Marine Res., V. 13, pp. 198-227, 1954.

14. Pierson, W. M., and Moskowitz, L., A Proposed Spectral Form for Fully Developed Wind Seas Based on Similarity Theory of S. A. Kitaigorodskic, J. Geoph. Res., V. 69, pp. 518.-5190, 1964.
15. Tolstoy, I. and Clay, C., Ocean Acoustics, McGraw-Hill, 1966.
16. Fortuin, L., The Wave Equation in a Medium with a Time-dependent Boundary, J.A.S.A., V. 53, pp. 302-305, 1972.
17. Beckmann, P., Shadowing of Randomly Rough Surfaces, Trans IEEE, Antenna Propagation, V. 13, pp. 384-388, 1965.
18. Wagner, R., Shadowing of Randomly Rough Surfaces, J.A.S.A., V. 41, pp. 138-147, 1967.
19. Kinsler, L. E. and Frey, A. R., Fundamental of Acoustics, Second Edition, Wiley, 1962.
20. Ishimaru, A., Wave Propagation and Scattering in Random Media, V. 2, Academic Press, 1978.
21. Clay, C. and Medwin, H., Acoustical Oceanography, Wiley, 1977.
22. Medwin, H., The Rough Surface and Bubbles Effect on the Sound Propagation in a Surface Duct, NPS-61Md71101A, October 1971.
23. Van Nostrand, D., Principles of Guided Missile Design, McGraw-Hill, 1955.
24. Texas Instruments Inc., TI Programmable 58/59 Math/Utilities, 1978.
25. Texas Instruments Inc., TI Programmable 58/59 Master Library, 1977.

INITIAL DISTRIBUTION LIST

	No. Copies
1. Defense Technical Information Center Cameron Station Alexandria, Virginia 22314	2
2. Library, Code 0142 Naval Postgraduate School Monterey, California 93940	2
3. Department Chairman, Code 61 Department of Physics and Chemistry Naval Postgraduate School Monterey, California 93940	1
4. NAVMATCOM NOR, Bureau of Weapons N-5078 Haakonsværn Norway	3
5. KNM "TORDENSKJOLD," Torpedo-/mine-skolen N-5078 Haakonsværn Norway	2
6. Norwegian Defense Research Establishment Division for Electronic P.O. Box 25, 2007 Kjeller Norway	1
7. Norwegian Defense Establishment Division for Underwater Warfare P.O. Box 115, N-3191 Horten Norway	1
8. Professor K. E. Woehler, Code 61Wh Department of Physics and Chemistry Naval Postgraduate School Monterey, California 93940	1
9. Professor H. Medwin, Code 61Md Department of Physics and Chemistry Naval Postgraduate School Monterey, California 93940	1
10. CDR Y. D. Tronstad, RNoN Naustvg. 23, N-5088 Mjølkeråen Norway	3